# Ionospheric tomography and data assimilation

Bruno, Jon

*Award date:*
2021

*Awarding institution:*
University of Bath

# IONOSPHERIC TOMOGRAPHY AND DATA ASSIMILATION

submitted by

Jon Bruno

A thesis submitted for the degree of Doctor of Philosophy

University of Bath

Department of Electronic and Electrical Engineering

January 2021

# Abstract

The impact the ionospheric electron density has on satellite-based applications, such as satellite communication and navigation systems, is of important consideration, as these signals must propagate through the ionosphere. The excess signal delay due to the ionospheric electron density is one of the main error sources in Global Navigation Satellite Systems (GNSS). One method to study the global behaviour of electron density is ionospheric tomography, a technique that allows estimation of the electron density in the ionosphere through line-integral observations between GNSS satellites and receivers. The research presented in this thesis benefits from the Multi Instrument Data Analysis System (MIDAS) (Mitchell and Spencer, 2003), an ionospheric tomography software that was originally capable of producing global or regional three-dimensional ionospheric electron density reconstructions from GPS observations.

GPS-based ionospheric tomography is first assessed in this thesis. This method shows accurate results in regions with high density of ground receivers. However, regions with sparse or uneven ground-receiver coverage give rise to geometric limitations, which lead to large errors in electron density estimation. To overcome this, a multi-GNSS (GPS-GLONASS-Galileo) based ionospheric imaging method is presented in this thesis. The method combines observations from different constellations of satellites orbiting around the Earth, which improves the availability and coverage of measurements for a given receiver network. The technique is evaluated for both under quiet and disturbed geomagnetic conditions, through simulation as well as experiment. The analysis quantifies the improvement of multi-GNSS tomography over single-GNSS tomography for electron density imaging in the ionosphere. The electron density images can be used to apply corrections to ionospheric delay in precise positioning algorithms.

Many GNSS precise positioning algorithms rely on ionospheric corrections to calculate the position. However, there is still room for improvement in reducing atmospheric and ionospheric induced errors. Application of corrections from multi-GNSS tomography is therefore proposed in this thesis to support GNSS positioning. Ionospheric corrections from a global network of multi-GNSS receivers are used in a single-frequency positioning method. The results show that this approach allows positioning accuracies comparable to dual-frequency positioning to be obtained, confirming the potential of using ionospheric corrections from multi-GNSS tomography.

# Acknowledgements

I am deeply grateful to my supervisor, Prof. Cathryn Mitchell, whose guidance has been invaluable throughout these years. Cathryn has understood my necessities and capabilities from the first day, and has helped me grow both personally and professionally.

I would also like to thank the Centre for Space, Atmospheric and Oceanic Science team at the University of Bath, in particular Karl Bolmgren, Dr. Talini Pinto Jayawardena, Dr. Ben Witvliet, Dr. Corwin Wright and Dr. Nikola Rankov for their working atmosphere and encouragement. This work would have not been possible without all of you.

Finally, I would like to thank my family and friends, and especially mi txiki. This long journey would have not been possible without their enormous support, patience and love. Eskerrik asko.

Global Positioning System (GPS) data were provided by the International GNSS Service (IGS), the University Navstar Consortium (UNAVCO), and the EUREF Permanent GNSS Network. Radar observations from Millstone Hill and EISCAT were obtained from the CEDAR Madrigal database. Ionosonde observations are taken from the Lowell Global Ionosphere Radio Observatory (GIRO) Data Center (LGDC).

This research was funded by the European Union's Horizon 2020 research and innovation programme under the Marie Skłodowska-Curie Grant Agreement No 722023.

# Table of contents

# List of Figures

# List of Tables

# List of abbreviations

**4DVAR** Four-Dimensional VARiational.

**CCL** Carrier-to-Code Levelling.

**CODE** Centre for Orbit DEtermination.

**DCB** Differential Code Bias.

**DF PPP** Dual-Frequency Precise Point Positioning.

**DOY** Day Of Year.

**EISCAT** European Incoherent SCATter.

**EOFs** Empirical Orthonormal Functions.

**EUV** Extreme Ultra-Violet.

**Fast-PPP** Fast Precise Point Positioning.

**GAIM** Global Assimilative Ionospheric Model.

**GIM** Global Ionospheric Map.

**GLONASS** GLObalnaya NAvigatsionnaya Sputnikovaya Sistema.

**GNSS** Global Navigation Satellite Systems.

**GPS** Global Positioning System.

**HF** High Frequency.

**IDA4D** Ionospheric Data Assimilation Four-Dimensional.

**IGS** International GNSS Service.

**IRI** International Reference Ionosphere.

**IRNSS** Indian Regional Navigation Satellite System.

**ISR** Incoherent Scatter Radio detection and ranging.

**MAPGPS** MIT Automated Processing of GPS.

**MEO** Medium Earth Orbit.

**MGEX** Multi-GNSS EXperiment.

**MIDAS** Multi Instrument Data Analysis System.

**NavIC** NAVigation with Indian Constellation.

**NNSS** Navy Navigation Satellite System.

**PNT** Positioning, Navigation and Timing.

**PPP** Precise Point Positioning.

**PVT** Position, Velocity and Time.

**QZSS** Quasi-Zenith Satellite System.

**RINEX** Receiver INdependent EXchange.

**RLS** Regularised Least Square.

**RMS** Root Mean Square.

**RMSE** Root Mean Square Error.

**RNSS** Regional Navigation Satellite Systems.

**SF PPP** Single-Frequency Precise Point Positioning.

**SP3** Standard Product 3 orbit.

**SPP** Single Point Positioning.

**sTEC** Slant Total Electron Content.

**TEC** Total Electron Content.

**TECu** TEC units.

**TGD** Timing Group Delay.

**TIDs** Travelling Ionospheric Disturbances.

**vTEC** Vertical Total Electron Content.

# List of symbols

| | |
|---|---|
| $A_{i,j}$ | Length of each ray within each voxel $(m)$. |
| $B$ | Magnetic flux density $(T)$. |
| $H_T$ | Scale height $(m)$. |
| $I$ | Ionospheric delay $(m)$. |
| $L$ | Electron density loss rate $(m^{-3}/s)$. |
| $M$ | Integer phase ambiguity $(cycles)$. |
| $N$ | Electron density $(m^{-3})$. |
| $N_m(F_2)$ | F2 layer peak electron density $(m^{-3})$. |
| $P0$ | Atmospheric pressure (milibar). |
| $T$ | Tropospheric delay $(m)$. |
| $T0$ | Atmospheric temperature (Kelvin). |
| $\delta_r$ | GNSS receiver instrumental phase bias $(s)$. |
| $\delta_s$ | GNSS satellite instrumental phase bias $(s)$. |
| $\eta$ | Regularisation tuning parameter. |
| $\kappa$ | Wave number $(m^{-1})$. |
| $\lambda$ | Wavelength $(m)$. |
| $\omega$ | Angular frequency $(rad/s)$. |
| $\omega_p$ | Plasma angular frequency $(rad/s)$. |
| $\rho$ | Pseudo-range observation $(m)$. |
| $\rho_{GF}$ | Pseudo-range geometry-free combination $(m)$. |
| $\mathbf{A}$ | Matrix of ray path geometry. |

| | |
|---|---|
| $\mathbf{D}$ | Matrix containing ray-differences over time. |
| $\mathbf{M}$ | Mapping matrix of orthonormal basis functions. |
| $\mathbf{R}$ | Regularisation matrix. |
| $\varepsilon$ | Unmodelled errors $(m)$. |
| $\varepsilon_0$ | Permittivity of free space $(V^{-1}m^{-1})$. |
| $\varphi$ | Carrier phase observation $(m)$. |
| $\varphi_{GF}$ | Phase geometry-free combination $(m)$. |
| $\vec{x}$ | Vector of electron concentration within each voxel. |
| $\vec{y}$ | Vector of TEC measurements. |
| $\vec{z}$ | Vector of coefficients of orthonormal basis functions. |
| $\widehat{y}$ | Vector of predicted TEC measurements. |
| $b_{clk}^{rel}$ | GNSS relativistic satellite clock error $(s)$. |
| $b_{del}^{rel}$ | GNSS relativistic signal delay due to space-time curvature $(s)$. |
| $b_r$ | GNSS receiver clock bias $(s)$. |
| $b_s$ | GNSS satellite clock bias $(s)$. |
| $c$ | Velocity of light in free space $(m/s)$. |
| $d_r$ | GNSS receiver instrumental code bias $(s)$. |
| $d_s$ | GNSS satellite instrumental code bias $(s)$. |
| $div(Nv)$ | Electron density transport rate $(m^{-3}/s)$. |
| $e$ | Electron charge $(C)$. |
| $f$ | Frequency $(Hz)$. |
| $f_p$ | Plasma frequency $(Hz)$. |

| | |
|---|---|
| $h$ | Vertical height $(m)$. |
| $h_m(F_2)$ | F2 layer peak height $(m)$. |
| $k$ | Number of measurements. |
| $l$ | Satellite to receiver path length $(m)$. |
| $m$ | Number of voxels. |
| $m_e$ | Electron mass $(kg)$. |
| $n$ | Refractive index. |
| $n_{gr}$ | Group refractive index. |
| $n_{ph}$ | Phase refractive index. |
| $p$ | Geometric distance $(m)$. |
| $q$ | Electron density production rate $(m^{-3}/s)$. |
| $r_{col}$ | Rate of collision between electrons and other particles. |
| $v_{gr}$ | Group velocity $(m/s)$. |
| $v_{ph}$ | Phase velocity $(m/s)$. |
| $wp$ | Pressure of water vapour (milibar). |
| $x$ | Electron concentration within each voxel $(m^{-3})$. |
| $z_h$ | Normalised height. |

# 1 Introduction

The solar-terrestrial environment comprises the space from the Sun to the Earth, and includes the Earth's atmosphere and magnetic field. The ionised region of the upper atmosphere, called the ionosphere, encompasses the region from $\sim$ 70 km to 1000 km above the Earth's surface. It is formed mainly through the absorption of electromagnetic solar radiation by the atmosphere as well as from particle precipitation at high latitudes. It varies both spatially and temporally and is influenced by changes in solar emissions, atmospheric dynamics and interplanetary and geomagnetic fields.

The ionosphere acts as dispersive medium to electromagnetic waves, where the signals are refracted and delayed depending on their frequency. The extent to which a signal with a given frequency is refracted depends also on the electron density of the ionosphere in which it is propagating. This means signals used in applications such as satellite communications that utilise trans-ionospheric propagation experience signal delays due to the electron density along their paths — typically quantified as the slant Total Electron Content (sTEC), the integrated electron density along the satellite-receiver signal path. These delays need to be corrected for successful use of satellite communication applications, which requires the estimation of the ionospheric electron density.

Different instruments are nowadays used to estimate the ionospheric electron density through various techniques. Among them, Global Navigation Satellite System (GNSS) constellations are one of the most common instruments to sense the ionosphere due to their availability, global coverage and cost-efficiency. They provide global or regional measurements, depending on the satellite to receiver geometry and the ground-receiver coverage over the area. Due to the dispersive nature of the ionosphere, signals from different frequency bands can be linearly combined to calculate the sTEC along the satellite to receiver path. Other ground instruments are also widely used to understand the physics of the ionosphere as well as independent validation tools for ionospheric models or algorithms. For example, ionosondes are low-cost vertical radio sounding instruments, which can estimate the ionospheric electron density up to the F-layer peak height. The Incoherent Scatter Radar (ISR) is the most accurate ionospheric sensing instrument, but it also has the highest power consumption, and thus is expensive to build and operate.

This thesis uses GNSS as the primary source of ionospheric measurements, with ionosondes and ISRs being used to valid the results. GNSS ground receivers provide valuable information about the ionosphere in the form of ray-path integrations of electron density (sTEC). Ionospheric tomography, which is an inversion imaging technique, ingest these sTEC measurements to reconstruct and create three or four-dimensional maps of the electron density of the ionosphere. The maps can then be used to estimate ionospheric delays experienced by GNSS signals.

Ionospheric delay estimation is much needed in GNSS-based navigation systems. In practice, most GNSS use a simplified two-dimensional ionosphere to correct for delays, which may not be sufficient in regions with strong ionisation gradients, such as equatorial or polar regions. Ionospheric tomography addresses this problem by providing three-dimensional distribution of electron density, which enables the ionospheric delay through the entire signal path to be calculated. It must be noted, however, that the accuracy of the maps depends on the number and distribution of observations, which is determined by the number of satellites and ground-receivers. Thanks to the increasing global availability of GNSS, data from different systems, such as GPS, GLONASS and Galileo, can now be used in ionospheric tomography to significantly improve the accuracy of three-dimensional ionospheric mapping, and therefore the ionospheric delay estimations for GNSS signals.

This dissertation aims to develop a novel multi-constellation ionospheric tomography framework using the Multi Instrument Data Analysis System (MIDAS) (Mitchell and Spencer, 2003) — a tomography software package developed at the University of Bath that can produce three and four dimensional images of the ionospheric electron density. The software is used to provide accurate ionospheric delay corrections for GNSS positioning methods. To achieve the main goal, intermediate objectives were set, which are summarised below:

- Evaluate the current state of MIDAS: Create a simulation framework to evaluate the accuracy of MIDAS over different regions with differing ground receiver coverage. At this stage only observations from GPS are used.
- Implement multi-constellation MIDAS (MIDAS-Multi): GLONASS and Galileo constellations are included into MIDAS. In addition, a novel method to estimate satellite and receiver Differential Code Biases (DCBs) using MIDAS-Multi is developed.

- Validate ionospheric corrections from MIDAS-Multi: Ionospheric delay corrections and satellite DCBs calculated from MIDAS-Multi are evaluated. The potential use of the corrections for GNSS positioning is assessed.

## 1.1 Thesis structure

This thesis is divided into 8 chapters. Chapters 2-4 provide the required background theory to support the scientific contribution introduced in this thesis. Chapters 5-7 discuss the research on ionospheric tomography and satellite-based positioning using ionospheric corrections. Chapter 8 concludes this thesis with an overall discussion and proposes possible future work that can be carried out in this area. A brief description of the structure of each chapter is given below:

**Chapter 2: Solar-terrestrial environment**

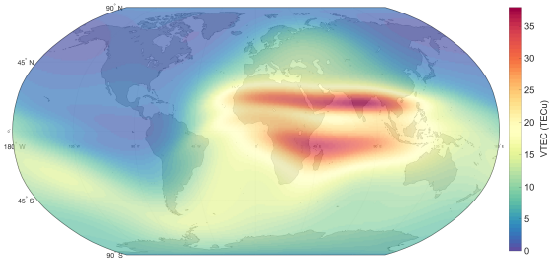


Chapter 2 provides an overview of the composition, variation and structure of the ionospheric electron density. An introduction to how the radio signals travelling through the upper atmosphere, such as satellite-based communications, are influenced by free electrons within the ionosphere is presented in this chapter.

**Chapter 3: Ionospheric sensing techniques**

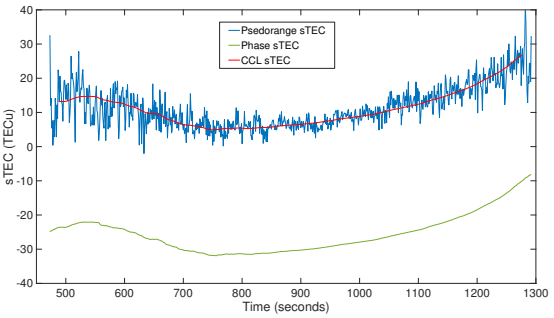


The most relevant ionospheric sensing techniques are introduced in Chapter 3. This includes trans-ionospheric instruments such as GNSS, and ground-based instruments such as ionosondes and Incoherent Scatter Radars (ISRs). An introduction about the different GNSS is first provided, the most relevant sensing instrument discussed in this thesis. In addition, the theory behind the use of observations from GNSS for ionospheric monitoring is described. Secondly, an overview of ionosondes and ISRs and the use of their observations for sensing the ionosphere is provided.

### Chapter 4: Ionospheric tomography

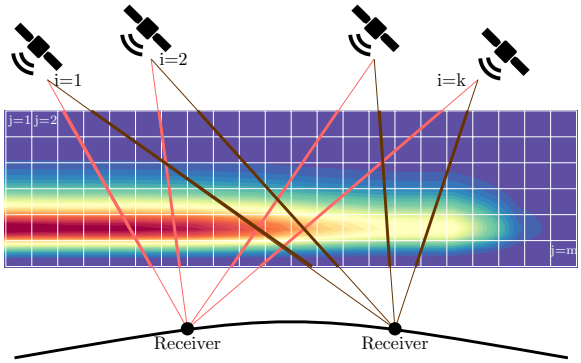


Chapter 4 describes the theory behind ionospheric tomography. The mathematical description of the tomographic problem, and how it is solved for the ionospheric case are discussed in this chapter. The use of regularisation techniques to make the ill-posed problem well-posed are described. In addition, the theory and special features of the most relevant ionospheric tomography algorithms are discussed. Particular attention is given to MIDAS, the software used throughout the work described in this thesis.

### Chapter 5: Simulation framework to evaluate ionospheric tomography

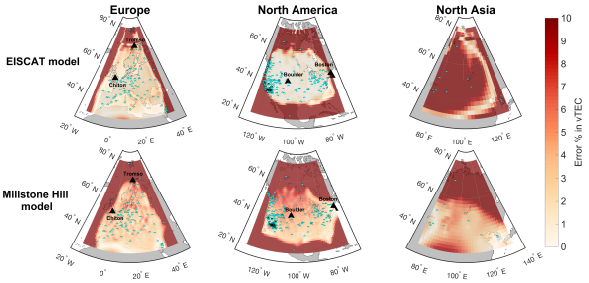


A novel simulation approach to test the quality of an ionospheric tomographic inversion technique is outlined in Chapter 5. The evaluation method, which uses observations from ISR scans to create a realistic ionospheric representation, is first introduced. The use of this ionospheric representation to create simulated observations, and the process to assess the accuracy of the ionospheric tomography algorithm are later discussed. Finally, the results gathered assessing the MIDAS algorithm using the simulation framework are presented in this chapter. The content of this chapter is published in the Advances in Space Research journal (Bruno et al., 2019).

### Chapter 6: Multi-constellation ionospheric tomography

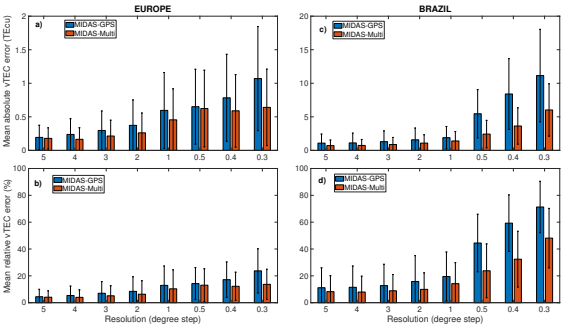


The increasing number of receivers tracking satellites from different GNSS, has enabled the transition from GPS-only to multi-constellation tomography. Chapter 6 investigates the potential for improvement in ionospheric mapping using the increased number of satellites in view — the multi-GNSS (GPS-GLONASS-Galileo) based MIDAS. First, two study regions are introduced, one mid-latitude and one equatorial. Europe and Brazil are chosen as they both have good ground-based coverage from multi-constellation GNSS receivers. The methods to evaluate the results, by simulation and by experiment, are later described. A comparison between multi-GNSS tomography and single-GNSS tomography for electron density imaging in the ionosphere is presented.

### Chapter 7: Global ionospheric delay corrections for single-frequency GNSS positioning

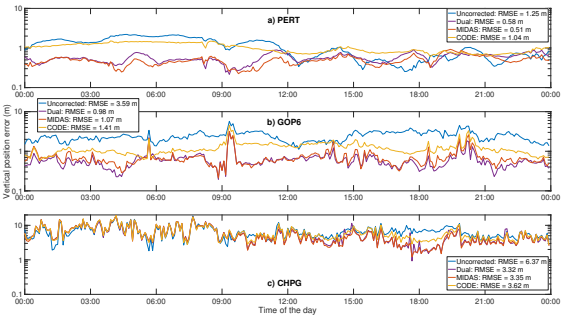


There are different approaches to assess the ionospheric estimations calculated with MIDAS. One solution is using external products, such as Global Ionospheric Maps (GIMs) as presented in Chapter 6. Another solution is validating against physics-based models (IRI, NeQuick 2) or third-party solutions. Unfortunately, none of the above provide a reference for validation, because the absolute electron density distribution within the ionosphere is unknown. Chapter 7 assesses the accuracy of the multi-constellation versions of MIDAS in the positioning domain. Ionospheric delays and satellite biases are provided to reference stations with a priori precisely known locations. The method to estimate the position of these reference stations is first described. The difference in positioning performance is used as a quality measurement for each of the provided ionospheric corrections. The main goal of this chapter is to quantise the accuracy of MIDAS in the positioning domain. Therefore, results from multi-constellation configuration and dual-frequency positioning are compared.

# 2 Solar-terrestrial environment

## Introduction

This chapter introduces the solar-terrestrial environment and the ionosphere, together with the influence of ionospheric free electrons on electromagnetic waves as they propagate through the upper atmosphere. The chapter is structured as follows: Section 2.1 gives an introduction to the coupling between the Sun's emissions and the Earth's upper atmosphere. Section 2.2 discusses the physical and chemical composition and structure of the ionosphere. In Section 2.3, the effect of free electrons within the ionosphere on electromagnetic waves propagating through the upper atmosphere is explained. Finally, a summary concludes this chapter.

## 2.1 The influence of the Sun

The Sun is a star that continuously emits electromagnetic radiation into interplanetary space. This radiation, together with a plasma outflow that carries millions of charged particles per second away from the Sun, results in the solar wind that constantly bombards the near-Earth system. The interplanetary magnetic field is a part of the Sun's magnetic field that is carried into interplanetary space by the solar wind. Due to the high electrical conductivity of the solar wind, the plasma and the magnetic field are frozen together. As the solar wind approaches the Earth, the plasma and the frozen-in interplanetary magnetic field interact with the outer geomagnetic field, also known as the magnetosphere. The magnetosphere acts as a shield against the solar wind plasma, forcing most of it to be swept around the Earth without penetrating the magnetosphere. Solar X-Ray and Extreme Ultra-Violet (EUV) radiation reaching the Earth is absorbed by the atmosphere, which ionises neutral atoms and molecules of the atmosphere to form the ionosphere. In addition, when the solar wind interacts with the geomagnetic field, particles can penetrate into the ionosphere along open magnetic field lines at the poles. The solar wind is therefore identified as a significant medium that couples the activity of the Sun with the Earth's atmosphere, making it extremely important for solar-terrestrial relations.

The composition and intensity of the Sun's emissions, and therefore the solar wind, is not constant, but driven by the Sun's activity. These activity periods occur with a

periodicity of around 11 years (Schwabe, 1843; Maunder, 1904), known as solar cycles, and have a strong influence on ionospheric dynamics. During the solar maximum when the solar activity is at its highest, larger events on the Sun such as solar flares increase the intensity and speed of the solar wind. This increases the number of particles formed within the ionospheric plasma. In contrast, during solar minimum when solar activity is low, the emissions from the Sun are weaker, decreasing the intensity of the solar wind and therefore the global mean ionospheric plasma density.

## 2.2 The ionosphere

The ionosphere is a layer in the upper atmosphere composed of free electrons and positive ions. It is created through the absorption of solar X-Ray and EUV radiation by the neutral atmosphere, which ionises atoms and molecules in the atmosphere, causing them to release free electrons. The composition of the ionosphere changes both spatially and temporally, driven by ion and electron production, loss and recombination processes. The region extends from $\sim$ 70 km to 1000 km above the Earth's surface.

Although the idea of an ionised layer in the upper atmosphere was first postulated by Gauss in 1839, it did not become widely accepted until the beginning of the 20th century. In 1901, Marconi sent a transatlantic radio signal from Cornwall, England, to Newfoundland, Canada, which was made possible thanks to the presence of free electrons within the upper atmosphere. However, it was not until 1931 that the first theory of the formation of an ionised region in the atmosphere was described by Chapman (1931).

### 2.2.1 Formation of the ionosphere

The density of free electrons in the ionosphere ($N$) varies over time and space, driven by the balance between production ($q$), loss ($L$) and transport ($div(Nv)$) processes of ions and electrons. The variation of the electron density with time can be expressed by the continuity equation (Hargreaves, 1979):

$$\frac{dN}{dt} = q - L - div(Nv) \tag{2.1}$$

where $div$ indicates the divergence operator — the term that indicates if there is more of the field vectors exiting an infinitesimal point than entering it — and $v$ is the mean drift velocity of electrons.

The production term ($q$) in Equation 2.1 is mainly driven by X-Ray and EUV radiation from the Sun, which is absorbed by the neutral atmosphere to produce ions and free electrons within the ionosphere. This phenomenon is known as photoionisation. The production rate depends on the absorption of solar radiation, which in turn depends partly on the solar activity and solar zenith angle. The intensity of radiation is strongest at high altitudes in the ionosphere, and decreases as altitude decreases. In contrast, the density of neutral atoms and molecules in the atmosphere decrease as altitude increases. The combination of these two phenomena produces a layer of electrons with a maximum density in an optimal altitude within the ionosphere, with lower densities above and below (Figure 2.1). In addition to solar radiation, ionised particles from the Sun travelling in the solar wind also contribute to the production process in the ionosphere. When the solar wind interacts with the geomagnetic field, particles can penetrate the ionosphere along open magnetic field lines — the main source of production at high latitudes (Barclay, 2003). The second term in the continuity equation (Equation 2.1) is Loss or Recombination ($L$). Recombination is the reverse process of photoionisation. During this process, negatively charged electrons and positively charged ions combine together to form neutral atoms or molecules again. Recombination is the main process that reduces the number of free electrons in the ionosphere. The last term in Equation 2.1 is the transport process ($div(Nv)$). During this process, the movement of plasma can occur both horizontally and vertically, which changes the electron and ion densities at a given location. The transport process is sometimes referred to as diffusion (Hunsucker and Hargreaves, 2003).

All three processes contribute to the electron density in the ionosphere at any given time and location. Photoionisation dominates during the day due to the availability of radiation from the Sun. The peak electron density in the ionosphere is therefore found slightly later than local noon. Recombination and diffusion in the ionosphere, on the other hand, take place throughout the day, but are especially important at night. During the night, recombination reduces the number of free electrons in the ionosphere as photoionisation no longer (or minimally) occurs due to the absence of solar radiation.

In addition to the diurnal variation, the solar cycle also has an impact on the density of the ionospheric plasma, with larger densities in the ionosphere generally found during solar maximum. Figure 2.2 shows an example of day-time and night-time electron density vertical profiles during solar maximum and minimum.

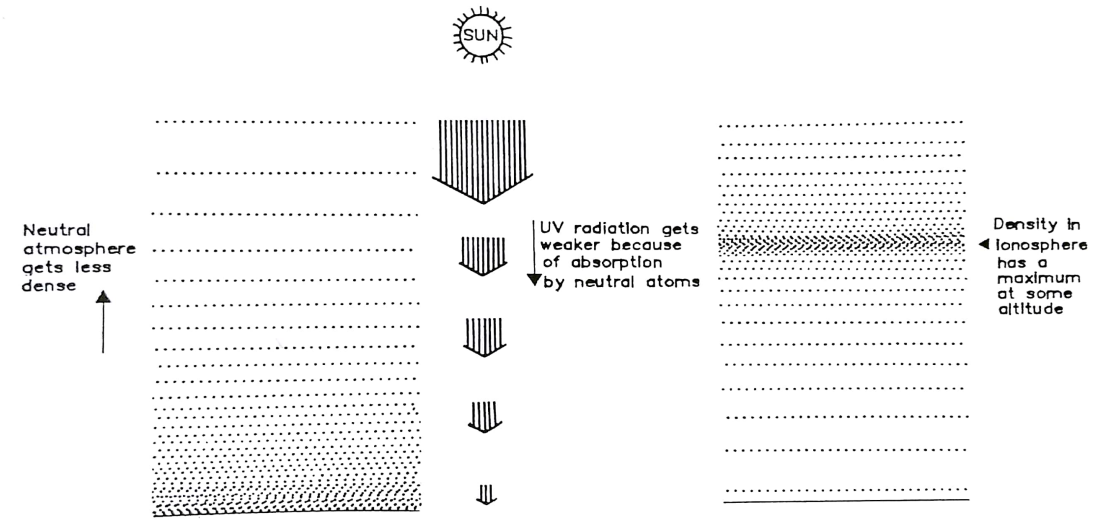


Figure 2.1: Variation in the density of the neutral atmosphere and solar intensity with height, and its impact on the formation of a ionised layer (McNamara, 1991).

### 2.2.2 Structure of the ionosphere

The ionosphere varies continuously with time of day, season, location and with the solar cycle. This section describes the spatial variation of the ionospheric electron density over the globe.

#### 2.2.2.1 Vertical structure

The vertical distribution of free electrons in the ionosphere is determined by two main conditions — density of the neutral atmosphere and intensity of solar radiation. The density of neutral atoms and molecules in the atmosphere that can be photoionised decrease as altitude increases. The radiation from the Sun, however, is absorbed as it propagates down through the upper atmosphere, decreasing the intensity of the solar radiation as it reaches lower altitudes. The process, as illustrated in Figure 2.1, produces a layer of ionised plasma with a maximum density at an optimal altitude that varies with solar and atmospheric conditions experienced at given time and location (Figure 2.2).

The basic vertical structure of the ionosphere contains four layers (Hunsucker and Hargreaves, 2003) known as D, E, F1 and F2 layers. As the ionospheric electron density is driven by the Sun, these regions are highly variable with season, time of day and solar activity.

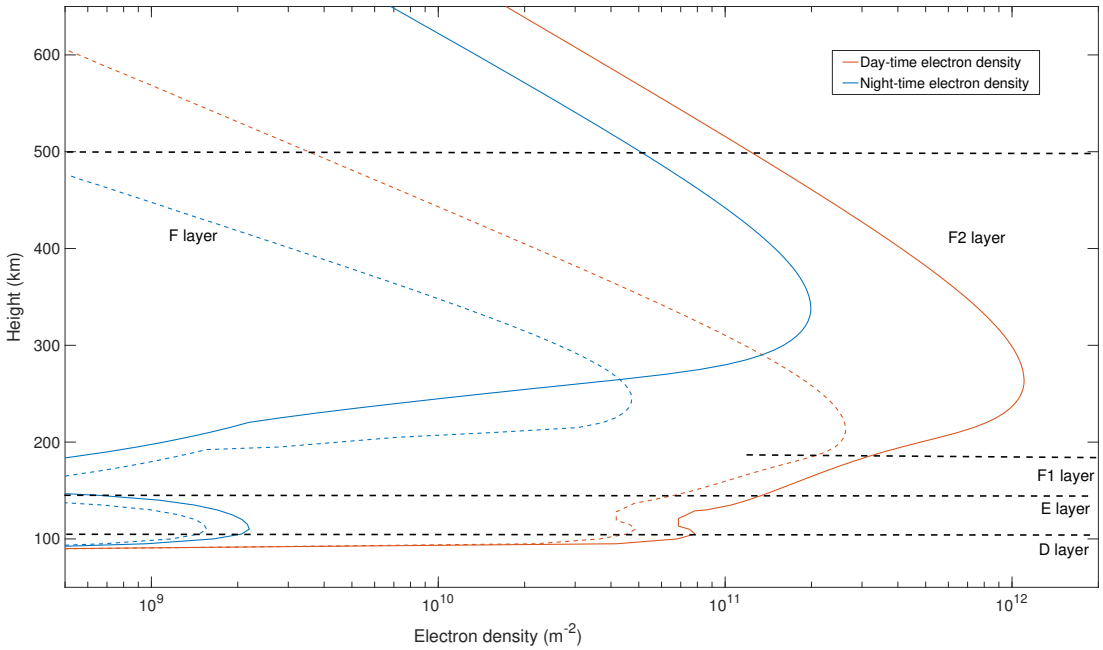


Figure 2.2: Day-time and night-time electron density profiles from the ionosonde at Juliusruh (Germany) the 2019-01-01 (solar minimum, dashed lines) and 2014-01-01 (solar maximum, solid lines).

The D layer is the lowest region of the ionosphere, starting at ∼70 km and reaching up to ∼90 km above the Earth's surface. It is characterised by a relatively weaker electron density compared to the higher layers because the radiation from the Sun is weaker at low altitudes (see Figure 2.1). Furthermore, the atmosphere is denser in this region compared to higher altitudes, leading to a higher collision rate, and thus a greater recombination rate. This layer is absent at night due to the low overall electron density and high recombination rate. The E layer is the region from ∼90 km to ∼150 km altitude. This layer is mainly driven by the equilibrium between production and loss, with the transport term having a minimal effect on plasma distribution. The most remarkable feature in the E-region is the sporadic-E, an irregular thin layer of ≃1 km extension in height (Barclay, 2003). This is particularly strong at low latitudes and it may reflect signals that otherwise would penetrate higher altitudes. The E-region is present throughout the night, but remains weakly ionised. The F layer is found between ∼150 km and ∼600 km, and comprises of the F1 and F2 sub-layers. This is the most important layer for radio propagation as it has the greatest density of electrons of any layer. Photoionisation is the main driver in this layer during the day.

Diffusion becomes more important than recombination as the height increases due to the decreasing density of the neutral atmosphere (Figure 2.1). This change in the dominant process leads to a division of the F layer into F1 and F2 layers. The F1 layer can be considered as a transition region between the E-layer and the upper ionosphere as it is also driven by the equilibrium between production and loss. The F2 layer peaks where recombination and diffusion are equally important. At night, only the F2 layer survives, as it has the highest electron density concentration in the ionosphere and the recombination rate is smaller due to the decrease in the density of the neutral atmosphere.

Above the F2-region, from about 600 to 1000 km, the electron density decreases exponentially with altitude. This region is known as the topside ionosphere. Beyond 1000 km, the topside ionosphere gives way to the plasmasphere, which is dominated by the geomagnetic field. The plasmasphere is often considered a part of the ionosphere for radio and satellite navigation applications, as although the electron density is very low in the plasmasphere, it has an impact on radio waves that propagate through the region (Garriott and Rishbeth, 1969).

#### 2.2.2.2 Global morphology

The global distribution of free electrons within the ionosphere is not homogeneous, and varies in both latitude and longitude. The longitudinal variation of the ionospheric plasma density is mainly related to the change in the solar zenith angle, which results in a local diurnal variation. The latitudinal variation, on the other hand, is affected mainly by the geomagnetic field, resulting in significant differences between low, middle and high latitude regions. The ionosphere at low-latitudes or the equatorial region, is mainly driven by photoionisation from solar radiation, and loss due to recombination. As the geomagnetic field is closed, no direct impact from particle precipitation is observed in this region. A dominant feature in the global ionospheric electron density at these latitudes is the equatorial anomaly (Hargreaves, 1979). The plasma at the equator is uplifted during the day. During post sunset hours there is a strong enhancement in the electric field, causing the plasma to reach higher altitudes. As it travel upwards at the magnetic equator, the plasma is guided along the magnetic field lines to lower altitudes on either side of the (magnetic) equator, resulting in an enhanced electron density at higher equatorial latitudes. This phenomenon is also known as the fountain effect (Hargreaves, 1979). The enhancements are located about $10 - 20^{\circ}$ either side of the magnetic equator in the F region (see Figure 2.3), and is usually where the largest electron densities are found.

Similar to equatorial latitudes, the mid-latitude region is mainly defined by solar photoionisation and chemical recombination. It is the least variable of the regions. The electron density distribution at mid-latitudes is dominated by the solar zenith angle and changes minimally during the day. The mid-latitude region is directly linked to the polar regions, and can therefore suffer significant variability during geomagnetic disturbances in the polar regions.

In the high latitude or polar region, ionospheric behaviour is closely coupled with to the near-space environment. The magnetosphere acts like a shield against the energy particles within the solar wind, forcing them to be swept around the Earth. The geomagnetic field at the poles however are open, which enables the solar wind to couple with this open field and penetrate into the polar ionosphere. This particle precipitation from the solar wind makes the region dynamic and more accessible to sporadic solar events (Hunsucker and Hargreaves, 2003). These events can be extremely intense, especially during high solar activity periods.

The electron density in the ionosphere is commonly characterised using the Total Electron Content (TEC) along a defined path. The vertically integrated electron density is known as Vertical Total Electron Content (vTEC). Figure 2.3 shows the ionospheric vTEC obtained from the International Reference Ionosphere (IRI)-2016 model (Bilitza et al., 2017). This model describes the monthly averages of electron density for the altitude range of 60 km to 2000 km, measured using different sources such as ionosondes and incoherent scatter radars. Both the TEC and vTEC are usually given in TEC units (TECu) (1 TECu = $10^{16}$ electrons per $m^2$).

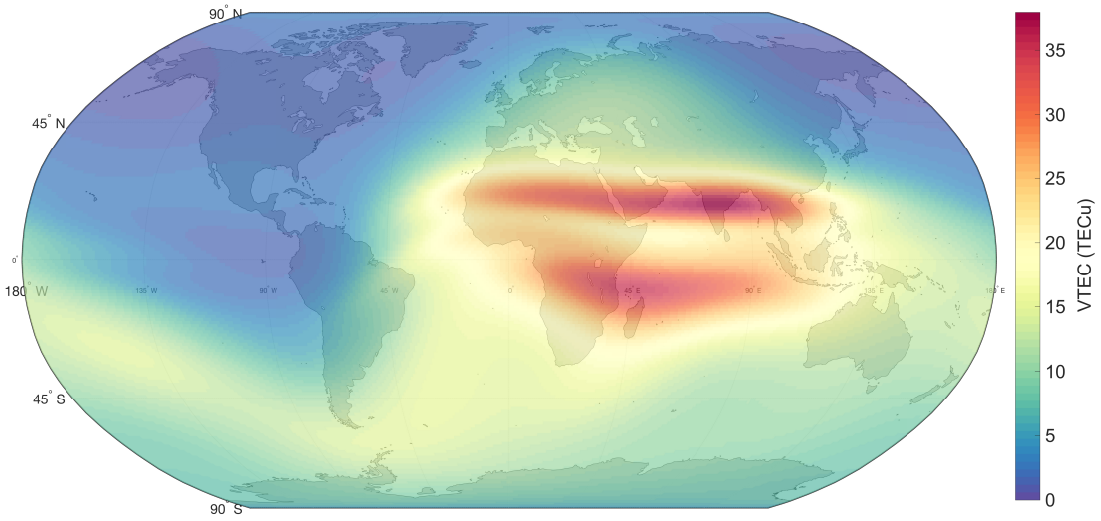


Figure 2.3: Ionospheric vTEC obtained from the IRI-2016 model for 1 January 2020 at 9:30 UTC.

## 2.3 Ionospheric radio propagation

Electromagnetic waves propagating the ionosphere interact with free electrons in the region, which affect their propagation velocities to varying degrees based on the signal frequency. This is because the ionosphere is a dispersive medium where the refractive index is dependent on both the frequency of the electromagnetic signal and the electron density of the ionosphere. In an ionised medium, the refractive index ($n$) is given by the Appleton-Hartree equation (Appleton, 1924):

$$n^2 = 1 + \frac{X}{1 - jZ - \frac{Y^2}{2(1 - X - jZ)} \pm \sqrt{(\frac{Y^4}{4(1 - X - jZ)^2} + Y^2)}} \tag{2.2}$$

where $X, Y$ and $Z$ are dimensionless terms that define the medium and its relationship with the frequency of the signal:

$$X = \frac{Ne^2}{m_e \varepsilon_0 \omega^2} \qquad \text{where} \qquad \omega = 2\pi f$$

$$Y = \frac{Be}{m_e} \qquad \text{and} \qquad Z = \frac{r_{col}}{\omega^2} \tag{2.3}$$

where $N$ is the electron density, $e$ is the electron charge, $m_e$ is the electron mass, $\varepsilon_0$ is the permitivity of free space, $\omega$ corresponds to the angular frequency of the radio signal, $f$ is the frequency of the radio signal, $B$ is the magnetic flux density and $r_{col}$ is the rate of collision between electrons and other particles (Davies, 1990). If collisions are considered to be negligible ($r_{col} = 0$) and the magnetic field is neglected ($B = 0$), the refractive index, $n$, can be approximated to:

$$n^2 = 1 + X = 1 + \frac{Ne^2}{m_e \varepsilon_0 \omega^2} \tag{2.4}$$

From Equation 2.4, it can be seen that the refractive index changes with the frequency of the signal. This makes the ionosphere a dispersive medium, which means that electromagnetic waves propagating through the region experience different velocities depending on the frequency of the signal. For a modulated signal — i.e. one that can have two or more signals of different frequencies (the envelope) superimposed on a another signal (the carrier) of a different frequency — that is travelling through the ionosphere, this means the different frequency components of the signal travel at different velocities. Due to this effect the ionosphere has on the carrier phase and envelope of the signal (which are of two different frequencies), the refractive index of the ionosphere can be divided into two components — the phase ($n_{ph}$) and group ($n_{gr}$) refractive indices.

$$n_{ph} = \frac{c}{v_{ph}} \qquad\qquad n_{gr} = \frac{c}{v_{gr}} \tag{2.5}$$

where $v_{ph}$ and $v_{gr}$ correspond to the phase and group velocities, respectively, and $c$ is the speed of light in vacuum. $v_{ph}$ and $v_{gr}$ in the plasma are defined as (Davies, 1990):

$$v_{ph} = \frac{\omega}{\kappa} \qquad \text{and} \qquad v_{gr} = \frac{d\omega}{d\kappa} \tag{2.6}$$

where $\kappa$ corresponds to the wave number and $\omega$ is the angular frequency. These parameters are given as:

$$\kappa^2 = \frac{\omega^2 - \omega_p^2}{c^2} \qquad \text{and} \qquad \omega_p = 2\pi f_p \tag{2.7}$$

where $\omega_p$ is the plasma angular frequency and $f_p$, the plasma frequency, corresponds to the oscillation frequency of electrons in the ionosphere (Rishbeth and Garriott, 1969).

Substituting Equation 2.7 into Equation 2.6 the phase and group velocities can be expressed as:

$$v_{ph} = \frac{c}{\sqrt{1 - \frac{f_p^2}{f^2}}} \qquad v_{gr} = \frac{c}{\sqrt{1 + \frac{f_p^2}{f^2}}} \tag{2.8}$$

From Equation 2.8, it can be seen that the phase velocity will always be larger than the group velocity. This translates to an advancement of the phase by the same amount as the group is delayed, and are generally referred to as phase advance and group delay. Substituting Equation 2.8 in Equation 2.5, the $n_{ph}$ and $n_{gr}$ refractive indices can be approximated by:

$$n_{ph} = \sqrt{1 - \frac{f_p^2}{f^2}} \simeq 1 - \frac{1}{2} \times \frac{f_p^2}{f^2} \qquad n_{gr} = \sqrt{1 + \frac{f_p^2}{f^2}} \simeq 1 + \frac{1}{2} \times \frac{f_p^2}{f^2} \tag{2.9}$$

The approximation $\sqrt{1 \pm a^2} \simeq 1 \pm \frac{1}{2} \times a^2$ can only be used when $a << 1$. In this case, $f$ (order of GHz) is much larger than $f_p$ (order of MHz), and thus this approximation is justified. Referring back to Equation 2.4, the plasma frequency ($f_p$) can be defined in terms of the electron density ($N$) as:

$$f_p^2 = \frac{Ne^2}{4\pi^2 m_e \varepsilon_0} \tag{2.10}$$

The plasma frequency at the peak of an ionised region is also referred to as the critical penetration frequency. When a radio signal arrives at the ionosphere from below, two possible scenarios can occur. If the signal has a frequency lower than $f_p$, it is reflected back to the Earth. If the frequency of the signal is larger than the local $f_p$, the signal passes through the ionosphere without reflection. In other words, $f_p$ indicates the minimum frequency needed for a signal to travel through a specific region of the ionosphere at a given time.

Substituting Equation 2.10 in Equation 2.9, the phase and group refractive indices of a medium relative to local electron density can be defined as:

$$n_{ph} = 1 - \frac{Ne^2}{8\pi^2 \varepsilon_0 m_e f^2} \qquad n_{gr} = 1 + \frac{Ne^2}{8\pi^2 \varepsilon_0 m_e f^2} \tag{2.11}$$

It must be noted that, as the plasma frequency changes with $N$, the propagation of a given signal depends on the electron density of the ionosphere. Under nominal ionospheric conditions, signals transmitted from the Earth with frequencies $\lessapprox 7$ MHz can be typically considered to be reflected back towards the ground. In reality however, if the signal is below the critical frequency, it is continuously refracted towards the Earth's surface as the refractive index changes with the electron density. This occurs until such an angle is reached that the signal is 'reflected' back towards the Earth. In contrast, signals with frequencies $\gtrapprox 9$ MHz typically travel through the ionosphere and reach outer space. The two processes of signal propagation are illustrated in Figure 2.4.

The dynamic behaviour of the ionosphere, which changes constantly and has a daily periodicity, has therefore a significant impact on radio propagation. As $f_p$ is a function of the ionospheric electron density, variations in the electron density will impact the propagation of a signal with a given frequency and determine if it would propagate through or get reflected back towards Earth. In addition, the take-off angle — the angle at which the signal is transmitted at relative to the ground — is of important consideration. Signals transmitted with lower take-off angles travel through more ionospheric plasma, and can therefore be reflected back more easily than signals transmitted with high take-off angles.

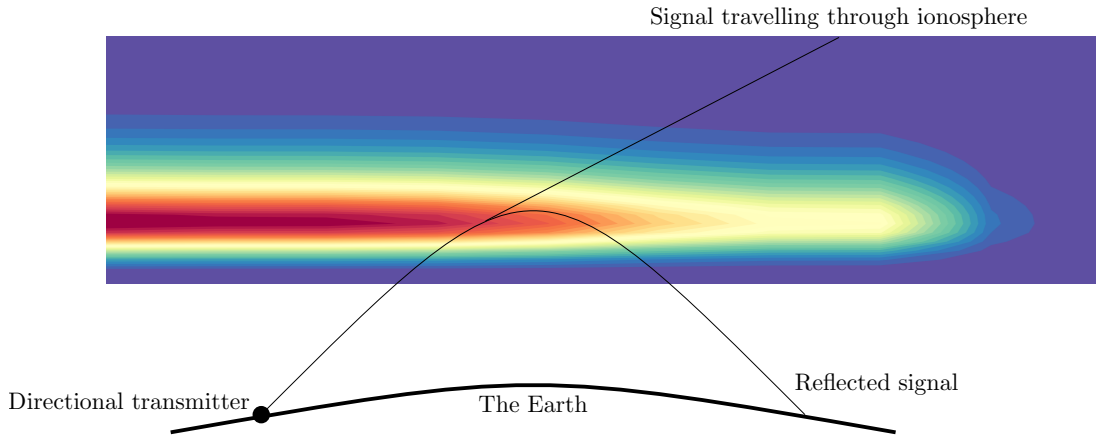


Figure 2.4: Example of one of multiple propagation paths of refracted and trans-ionospheric signals.

### 2.3.1 Propagation of satellite navigation signals

In satellite navigation, the frequencies of the waves travelling from satellites in space to the Earth lie between 1-3 GHz. These signals travel through the ionosphere, as their

frequencies are much larger than $f_p$ in the ionosphere ($0.1 - 9$ MHz). As mentioned in Section 2.2, TEC is the total electron density integrated along a given signal path, which is the path between the transmission satellite (S) and receiver (R) for satellite navigation systems.

$$sTEC \text{ (TECu)} = \int_S^R N dl \tag{2.12}$$

where Slant Total Electron Content (sTEC) corresponds to the TEC along the path from satellite to receiver. For TEC derived from satellite-receiver ray paths, the term sTEC is generally used to distinguish from vTEC that is commonly used in ionospheric research. An illustration of vTEC and sTEC between a satellite and ground receiver is given in Figure 2.5.

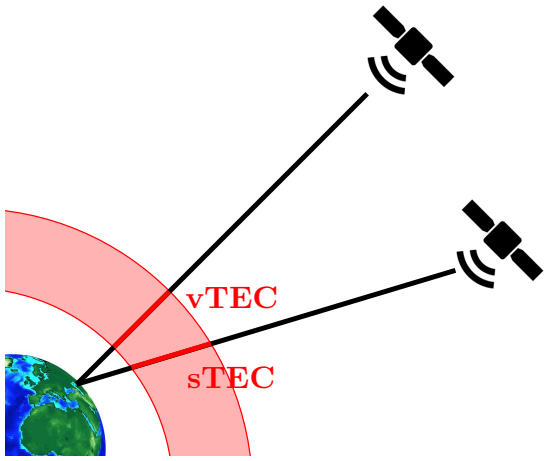


Figure 2.5: Illustration of ionospheric vTEC and satellite to receiver sTEC.

As the signal from the satellite is refracted when travelling through the ionosphere on its way to a receiver on the Earth, the path length ($l$) and geometric distance ($p$) between satellite and receiver are not equal.

$$\begin{aligned} l = c\int_S^R dt_{vacuum} + dt_{iono} = c\int_S^R \frac{dl_{vacuum}}{c} + \frac{dl_{iono}}{v_{iono}} = \\ = c\int_S^R \frac{p - dl_{iono}}{c} + \frac{dl_{iono}}{v_{iono}} = \int_S^R (p - dl_{iono}) + n\, dl_{iono} = p + \int_S^R (n-1) dl \end{aligned} \tag{2.13}$$

Therefore, the ionospheric path length delay/advance produced in the signal due to

the ionospheric electron density ($I$) is the integration of the refractive indices through the satellite to receiver path (McNamara, 1991):

$$I(m) = \int_S^R (n-1)dl \tag{2.14}$$

Using Equation 2.11 in Equation 2.14, the relation between ionospheric delay, the refractive indices ($n_{ph}$ and $n_{gr}$) and frequency of a propagating satellite navigation signal can be expressed as:

$$\begin{aligned} I(m) = \int_S^R (1 \pm \frac{e^2 N dl}{8\pi^2 \varepsilon_0 m_e f^2} - 1) = \pm \frac{e^2}{8\pi^2 \varepsilon_0 m_e f^2} \int_S^R (N dl) = \\ = \pm \frac{e^2}{8\pi^2 \varepsilon_0 m_e f^2} \times sTEC = \frac{40.3 \times 10^{16}}{f^2} \times sTEC \end{aligned} \tag{2.15}$$

## 2.4 Summary

This chapter provided an overview of the driving processes that create the ionosphere, the morphology of the ionospheric plasma and the effect free electrons within the ionosphere have on radio signals propagating the region.

The ionosphere is the ionised layer of the upper atmosphere. It is created from the ionisation of the neutral atmosphere from solar radiation, and particle precipitation along the geomagnetic field at high latitudes. The density of the plasma containing ions and free electrons varies both spatially and temporally. The electron density changes with latitude and has three main regions: low-latitude (or equatorial), mid-latitude and high latitude (or polar). It also changes with altitude as the density and pressure of the neutral atmosphere changes. Variation of the electron density with time is seen diurnally, seasonally and with the solar cycle as the ionisation processes are driven by solar activity and related emissions from the Sun.

The ionosphere acts as a dispersive medium to electromagnetic signals, where free electrons within the ionosphere change the phase and group velocities of propagating radio signals. The effect on the signals is driven by the refractive index, which is dependent on the frequency of the signal and the electron density of the ionosphere. Depending on the frequency of the radio signal arriving at the ionosphere and the local plasma frequency, the signal can be reflected back or refracted when travelling through

the ionosphere.

The impact the ionospheric electron density has on satellite-based applications, such as satellite navigation systems, is an important consideration, as these signals must propagate through the ionosphere. The upper atmosphere introduces an advance/delay in the path relative to the signal frequency and sTEC measured between the satellite and the receiver. A comprehensive understanding of the ionosphere and its behaviour is therefore required to ensure successful correction of the ionospheric delay and therefore successful operation of these systems. The next chapter discusses sensing techniques that can be used to measure and study the ionosphere.

# 3 Ionospheric sensing techniques

## Introduction

Various techniques have been developed to calculate the ionospheric electron density distribution over time and space, from the lowest part of the ionosphere and into the plasmasphere.

A review of three different instruments for measuring the ionospheric electron density is provided in this chapter, with a focus on the limitations and capabilities of each of them. These instruments are the GNSS constellation of satellites, vertical radio sounding instruments (also known as ionosondes) and Incoherent Scatter Radars (ISRs). GNSS are able to provide global-scale and near real-time coverage of the ionospheric total electron content, whereas ionosondes and ISRs can observe the electron density with high accuracy over their locations. These instruments provide key measurements for the research described in this thesis, both as input parameters and as validation measurements.

## 3.1 Global Navigation Satellite Systems

Global Navigation Satellite Systems (GNSS) are composed of constellations of satellites orbiting around the Earth. These satellites broadcast radio signals that carry information about their position and the time when the signals were transmitted. GNSS receivers on the ground or in space can use these signals from multiple satellites and estimate their Position, Velocity and Time (PVT). The signals from these satellite constellations are a unique and important resource for ionospheric measurements as they provide near real-time global coverage.

GNSS satellites orbit the Earth in the Medium Earth Orbit (MEO), at an altitude of $\sim$22000 km. They transmit electromagnetic waves with frequencies between $\simeq$ 1.2 and 1.6 GHz. Current operational systems have at least two allocated bands for transmission, each one with a different centre frequency. The first successful satellite positioning system was the Navy Navigation Satellite System (NNSS), also known as TRANSIT, built by the U.S. military in the 1960s (Parkinson and Gilbert, 1983). In 1996, it was substituted by the Global Positioning System (GPS) (Parkinson et al.,

1996). Other countries have also launched their own global navigation satellite systems. Russia developed GLObalnaya NAvigatsionnaya Sputnikovaya Sistema (GLONASS) in 1982 (Ivanov and Salischev, 1992; Dvorkin et al., 2009), intended initially for military purposes, but now available for civilian use. BeiDou (Chengqi, 2012), the Chinese GNSS, became fully operational in 2012. Finally, the European Galileo project (Benedicto et al., 2000), is the first GNSS developed under civilian control. The first generation of satellites (full constellation of 22 satellites) were fully operational by 2020, while the second generation of satellites is planned to be available by 2025.

In addition to GNSS, Regional Navigation Satellite Systems (RNSS) have also been launched by several countries to augment existing GNSS services. These systems enhance precise Positioning, Navigation and Timing (PNT) applications over specific areas of the Earth, and can therefore have a great impact regionally. Currently operational RNSS are the Japanese Quasi-Zenith Satellite System (QZSS) (Takahashi, 2004; Murai, 2014) and the Indian Regional Navigation Satellite System (IRNSS) (Ganeshan et al., 2005); the latter recently renamed as NAVigation with Indian Constellation (NavIC). QZSS's orbits are designed to continuously provide at least one satellite near zenith over Japan, intended to overcome the probable obstruction of GPS signals by high-rise buildings in urban areas. The NavIC, on the other hand, serves as a complementary system in India and over an area extending up to 1500 km from its boundaries.

### 3.1.1 GNSS observations

The fundamental quantity measured by any GNSS receiver is the time delay of the signal when propagating between a satellite and receiver. This is converted to the corresponding distance (or range $p$) by multiplying it by the speed of light ($c$).

$$p = (t_r - t_s) \times c \tag{3.1}$$

where $t_r$ and $t_s$ represent reception and transmission time respectively. In an ideal system, three simultaneous satellites are needed to determine the exact position of the receiver in three dimensional space. Each satellite gives the position of the receiver somewhere on a sphere of radius $p$ centred at the position of the satellite. The intersection point of different spheres from different satellites gives the location of the receiver (Figure 3.1).

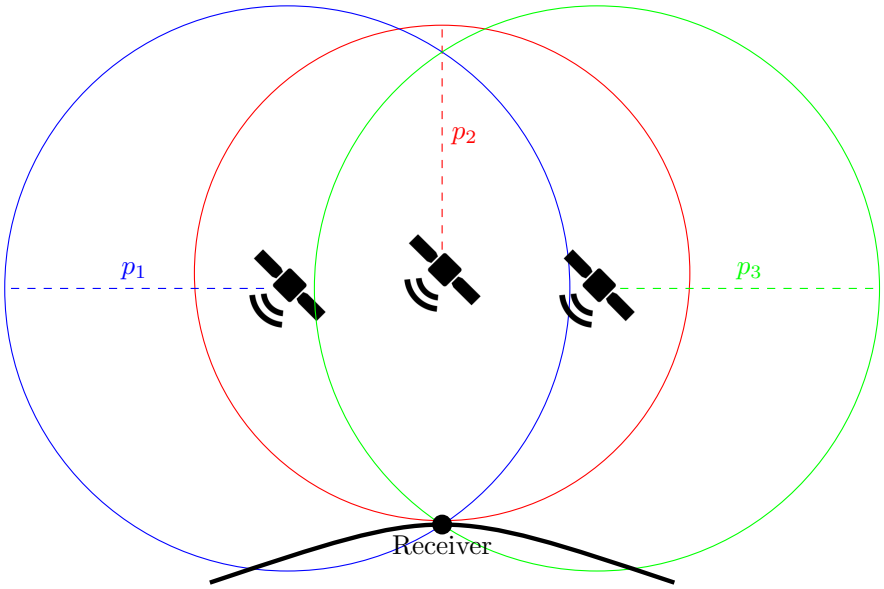


Figure 3.1: GNSS positioning theory

In a real system, however, the range measurement of the receiver ($p$) is biased by instrumental errors, atmospheric delays and other errors such as noise and multipath, resulting in the measured range between the satellite and receiver usually being referred to as pseudorange ($\rho$). The mathematical expression taking into account these effects on the signal gives the expressions for the pseudorange:

$$\rho = p + p_{sag} + c \times (b_r - b_s - b_{clk}^{rel} + b_{del}^{rel}) + c \times (d_r + d_s) + T + I + \varepsilon \tag{3.2}$$

where $p_{sag}$ corresponds to the Sagnac delay, $b_r$ and $b_s$ correspond to receiver and satellite clock errors, $b_{clk}^{rel}$ and $b_{del}^{rel}$ correspond to the relativistic clock error and the relativistic signal delay due to space-time curvature, $d_r$ and $d_s$ refer to receiver and satellite instrumental biases, and $T$ and $I$ represent the errors generated as the signal propagates through the troposphere and the ionosphere, respectively. Any unmodelled errors, such as multipath or hardware noise, are represented by $\varepsilon$. Once all errors are accounted for, the position of the receiver can be calculated from $\rho$ (see Figure 3.1). While the receiver position (x, y, z) would theoretically require observations from 3 satellites, as the user has to estimate the receiver clock error ($b_r$), simultaneous observations from at least four satellites are needed to accurately arrive at the position solution.

The range $p$ may also be derived from the carrier phase ($\varphi$, presented in meters) of the signal, which can be represented in a similar way:

$$\varphi = p + c \times (b_r - b_s - b_{clk}^{rel} + b_{del}^{rel}) + c \times (\delta_r + \delta_s) + T - I + \lambda M + \varepsilon \tag{3.3}$$

where $\delta_r$ and $\delta_s$ correspond to the receiver and satellite instrumental biases in the carrier phase measurement and $M$ is the integer ambiguity term, which introduces a delay that is proportional to the wavelength $\lambda$ of the signal (i.e. the number of cycles of the wavelength). It can also be seen that the $I$ term has a negative sign in Equation 3.3, as opposed to a positive term in Equation 3.2. This is because, as mentioned in Section 2.3, the phase of the signal is advanced and the group is delayed when travelling through the ionosphere. In contrast to the pseudorange being calculated from the total time delay the signal travels from satellite to receiver, the carrier phase is calculated from the number of cycles of the signal that was required to travel from the satellite to the receiver. As the wave-length of the carrier phase is short (∼19-25 cm), the carrier phase measurement is much more precise than the code-based pseudorange measurement (Teunissen and Montenbruck, 2017).

### 3.1.2 Estimating the ionospheric delay

GNSS signals propagating from a satellite to a receiver on the Earth are delayed/advanced as they pass through the ionised upper atmosphere. As given in Equations 2.12 and 2.15, this effect of the ionosphere on the signal ($I$) is directly proportional to the integral of the refractive index along the satellite to receiver ray path.

$$I = \int_R^S (1 - n) dl = \frac{40.3 \times 10^{16}}{f^2} \times sTEC \tag{3.4}$$

The $40.3 \times 10^{16}/f^2$ factor translates the sTEC from TECu to delay in metres. Equation 3.4 shows that $I$ changes with the signal frequency $f$, which shows the dispersive nature of the medium. By recording pseudorange (Equation 3.2) or phase (Equation 3.3) observations at two different frequencies from the same satellite, the frequency-dependent terms can be isolated and the sTEC along the satellite-receiver ray path derived. This is called the geometry-free linear combination (Mannucci et al., 1998).

$$\rho_1 - \rho_2 = \rho_{GF} = c \times (d_{r,1} - d_{r,2}) + c \times (d_{s,1} - d_{s,2}) + (I_1 - I_2) + \varepsilon_{GF} \tag{3.5}$$

where $\rho_{GF}$ corresponds to the geometry-free pseudorange observation. The same differential process can also be applied to phase observations.

$$\varphi_1 - \varphi_2 = \varphi_{GF} = c\times(\delta_{r,1} - \delta_{r,2}) + c\times(\delta_{s,1} - \delta_{s,2}) - (I_1 - I_2) + (\lambda_1 M_1 - \lambda_2 M_2) + \varepsilon_{GF} \quad (3.6)$$

where $\varphi_{GF}$ corresponds to the geometry-free carrier-phase observation. By substituting Equation 3.4 in Equation 3.5 or 3.6, all the frequency dependent terms, such as the satellite to receiver sTEC (sTEC), can be obtained.

#### 3.1.2.1 Inter-frequency differential code biases

The differences between the instrumental biases of the code-based pseudorange at two different frequencies are known as inter-frequency differential code biases, or Differential Code Bias (DCB) for short (Lanyi and Roth, 1988).

$$DCB_r = d_{r,1} - d_{r,2} \qquad DCB_s = d_{s,1} - d_{s,2} \quad (3.7)$$

where $DCB_r$ and $DCB_s$ represent the receiver and satellite DCBs respectively. The $d_r$ and $d_s$ biases are generated by the analog and digital processes of the signal generation unit and of the antenna of both the satellite and receiver. The absolute bias of a single signal is not observable as the biases are frequency dependant and can only be observed through signal differencing. Therefore, only the differential code biases between signals can be observed. The DCBs can be constant throughout the day or even over several days based on the stability of the satellite and receiver hardware (Coco et al., 1991; Wilson and Mannucci, 1993).

It must be noted that, although both Equations 3.5 and 3.6 can be used to measure the $I$, the sTEC derived from the two equations will be different. This is because, the sTEC obtained from the differential pseudorange (Equation 3.5) provides absolute values biased by the DCBs. These values tend to be very noisy due to the precision of the pseudorange measurements, especially at low elevations ($< 10°$) when the signal is subject to multipath. In contrast, sTEC calculated using the carrier phase (Equation 3.6) are more precise and have minimal noise. However, the presence of the $M$ terms in Equation 3.6 makes the sTEC results relative if the integer ambiguity term is not accounted for, and cannot provide information on the true sTEC along the path.

One solution to obtain the absolute sTEC with minimal noise is the Carrier-to-Code Levelling (CCL) method (Ciraolo et al., 2007). This technique is based on the geometry-free linear combinations of both the code and phase measurements. By computing the average difference between phase and code for every satellite pass (arc), the TEC retrieved from the $\varphi_{GF}$ can be calibrated, and an absolute sTEC can therefore be derived, which also has minimal noise.

$$\langle \varphi_{GF,arc} - \rho_{GF,arc} \rangle = \delta_{r,GF} + \delta_{s,GF} + \lambda M - DCB_r - DCB_s - \varepsilon_{GF,arc} \tag{3.8}$$

It is worth mentioning that Equation 3.8 does not consider the effect of noise and multipath on $\varphi_{GF,arc}$, as these effects are $\simeq \times 100$ smaller than the ones in $\rho_{GF,arc}$. The $\delta_r$, $\delta_s$ and $M$ terms are assumed to be constant for the duration of the arc. $\varphi_{GF} - \langle \varphi_{GF,arc} - \rho_{GF,arc} \rangle$ therefore removes these terms, but introduces DCBs, noise and multipath coming from the code (pseudorange) measurement ($\rho_{GF}$):

$$\varphi_{GF} - \langle \varphi_{GF,arc} - \rho_{GF,arc} \rangle = sTEC_{CCL} = sTEC_{absolute} + DCB_s + DCB_r + \varepsilon_{GF} \tag{3.9}$$

where $sTEC_{CCL}$ is the measured CCL sTEC and $sTEC_{absolute}$ corresponds to the absolute sTEC. The average $\varepsilon_{GF}$ can be assumed to be negligible over each satellite pass by using a suitable elevation cut-off to minimise multipath, and the effect can be ignored in the carrier-to-code levelling process (Ciraolo et al., 2007). $sTEC_{absolute}$ can then be obtained by calculating satellite and receiver DCBs and removing their effect from $sTEC_{CCL}$. The sTEC based on pseudorange, phase and CCL are illustrated in Figure 3.2.

#### 3.1.2.2 Estimating inter-frequency differential code biases

Different techniques have been developed to estimate DCBs from GNSS satellites and receivers, which can be categorised into two main groups: techniques that estimate ionospheric sTEC/vTEC and DCBs together, and those that estimate the electron density distribution first (or rely on third party solutions for the estimate) and then calculate the DCBs. The methods that simultaneously compute the vTEC and the satellite and receiver DCBs are introduced first, followed by the second approach that uses a two-step process.

For a given receiver, the sTEC unknowns for each satellite have different time and geometry dependencies. In addition, the DCBs have to be estimated. This makes the

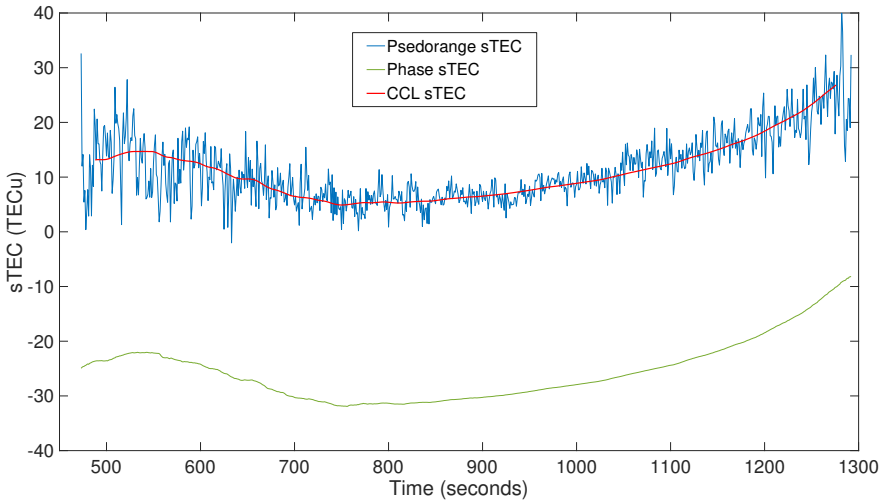


Figure 3.2: Differential pseudorange and carrier-phase from GPS G03 satellite on the 1st of January 2019.

observation equation system rank deficient, meaning that the system has more unknowns than equations, and cannot be directly solved. This can be addressed by translating all sTEC measurements to vTEC by means of an elevation-dependent geometry scaling factor. This removes the geometry dependency from the sTEC, decreasing the number of unknowns in the system (1 vTEC per receiver vs. 1 sTEC per satellite-receiver pair) and making it solvable. The most common technique to independently solve all unknowns is by means of the least squares method as demonstrated by Wilson et al. (1995), Mannucci et al. (1998), Ma et al. (2014), and Vierinen et al. (2016). In N. Wang et al. (2016) and Zha et al. (2019), the combined $DCB_s + DCB_r$ is computed alongside the vTEC by least squares estimation. In these works, a second step is incorporated to separate the satellite and receiver DCBs by assuming a zero-mean satellite DCB reference regularisation for each individual constellation. Another method introduced by Sardón et al. (1994) was the use of a Kalman Filter to estimate the DCBs and vTEC simultaneously. In this case, a receiver was set as the reference and the remaining biases were estimated relative to that receiver.

The second approach to estimating DCBs is less common, as it requires a two-step process or relies on external information. Montenbruck et al. (2014) used ionospheric TEC from the Global Ionospheric Map (GIM) estimated by different International GNSS Service (IGS) Analysis Centres. sTEC values were calculated using these maps, and the combined DCBs were then estimated using the least squares method. To separate satellite and receiver DCBs, the same zero-mean satellite reference method as

in N. Wang et al. (2016) was used.

In Dear and Mitchell (2006) a variation of the second approach was implemented where ionospheric tomography was used to obtain absolute sTEC ($sTEC_{absolute}$). The $DCB_{combined}$ ($DCB_s + DCB_r$) were retrieved by comparing the sTEC values from ionospheric tomography with the $sTEC_{CCL}$ for each satellite-receiver pair:

$$DCB_{combined} = sTEC_{CCL} - sTEC_{absolute} \tag{3.10}$$

### 3.1.3 Positioning theory

One of the methods to assess ionospheric tomography is in the positioning domain (Chapter 7). In this work, single-frequency pseudorange observations from GPS only are used in a Single Point Positioning (SPP) algorithm. This method provides epoch-wise positions, without carrying any information from epoch to epoch. As this method only uses pseudorange observations to calculate the position, no phase ambiguities have to be estimated.

As discussed in Section 3.1.1, pseudorange observations have generally larger noise than carrier-phase observations. Therefore, to reduce the noise in the solution, a pseudorange smoothing technique, as defined by Hatch (1983) and Teunissen (1991) is used. This results in pseudorange observations with carrier-phase noise levels. In order to compute the position from Equation 3.2 all error terms defined in the equation must be corrected for. These terms, and how they can be solved for are discussed in the following sections.

#### 3.1.3.1 Sagnac effect

The Sagnac delay ($p_{sag}$) refers to the delay generated by the rotation of the Earth-Centred Earth-Fixed reference frame during signal propagation. One possibility to correct the delay is to rotate the satellite position backwards around the Earth by an angle relative to the signal travel time ($t_{travel}$) (Ashby, 1995).

$$p_{sag} = \vec{\Omega} \times t_{travel} \qquad \text{where} \qquad t_{travel} = \frac{\vec{R} \times \vec{S}}{c} \tag{3.11}$$

where $\vec{\Omega}$ is the rotation vector of the Earth, $\vec{R}$ corresponds to the receiver position vector, $\vec{S}$ is the satellite position vector and $c$ is the speed of light in vacuum. This

approach has been used in this thesis.

#### 3.1.3.2 Satellite clock and instrumental delay

Estimates for each of the satellite clock errors $b_s$ are calculated and made publicly available by the IGS. These clocks corrections are calculated from the ionosphere-free linear combination, which combines signals from two different frequencies. To use these satellite clock corrections for single frequency positioning, a term called Timing Group Delay (TGD) must be applied to the satellite clock error provided by IGS:

$$TGD = DCB_{nm} \times \frac{f_n^{-2}}{f_n^{-2} - f_m^{-2}} \tag{3.12}$$

where $DCB_{nm}$ is the differential code bias between signal frequency suffix $n$ and $m$, and $f$ is the frequency of the signal.

In addition to the satellite clock corrections, the excess clock relativistic error ($b_{clk}^{rel}$) is also calculated and corrected for. This effect is caused by the orbital eccentricity that causes a residual variation in distance and velocity over and above that which has already been compensated for in a circular orbit. The correction term is calculated following Ashby (1995):

$$b_{clk}^{rel} = -2 \times \frac{S \times V}{c^2} \tag{3.13}$$

where $S$ and $V$ corresponds to satellite position and velocity respectively. The additional term of the relativistic path delay ($b_{del}^{rel}$) is neglected in this work, as it is ∼1000 times smaller than the clock relativistic effect, only accounting for ∼2 cm error in the positioning estimation (Teunissen and Montenbruck, 2017)).

#### 3.1.3.3 Tropospheric delay

The tropospheric delay ($T$) is calculated in two steps. First, the zenith tropospheric delay ($ZTD$) is estimated using the Saastamoinen model (Saastamoinen, 1972):

$$ZTD = \frac{0.0022767 \times P0}{1 - 0.00266 \times \cos(2\Phi) - 0.00028 \times h} + 0022767 \times \left[\frac{1255}{T0} + 0.05\right] \times wp \tag{3.14}$$

where:

$$T0 = 288.15 - \frac{6.5 \times h}{1000} \qquad P0 = 1013.25(\frac{288.15}{T0})^{-5.255877}$$
$$wp = 0.5 \times \exp\left(24.3702 - \frac{6162.3496}{T0}\right)$$

where $P0$ corresponds to the atmospheric pressure, $\Phi$ is the receiver's latitude, $h$ is the receiver's height, $T0$ corresponds to the atmospheric temperature and $wp$ is the pressure of water vapour. This model provides zenith tropospheric delay. To obtain the slant tropospheric delay, the Ifadis mapping function (Ifadis, 1986) is used:

$$MF = \frac{1 + \left[\frac{a}{1 + b/(1 + c)}\right]}{\sin(e) + \left[\frac{a}{\sin(e) + b/(\sin(e) + c)}\right]} \tag{3.15}$$

where e is the elevation angle, and $a$, $b$, $c$ are parameters that depend on atmospheric temperature and pressure. The values of these parameters are retrieved from (Ifadis, 1986). Therefore, the tropospheric delay is given by:

$$T = MF \times ZTD \tag{3.16}$$

#### 3.1.3.4 Satellite transmission time correction

Although RINEX files store observations at the time of reception, no information about the satellite transmission time is saved. Therefore, the time of transmission has to be calculated, which is done by subtracting the signal's time of travel $t_{travel}$ (Equation 3.11) from the reception time. This is then used to calculate the satellite position at the time of transmission. As $t_{travel}$ is a function of the satellite position ($S$), which is unknown at transmission time, an iterative approach is needed. On each iteration, the updated satellite position is used compute a refined estimate of $t_{travel}$. It has been demonstrated that three iterations are sufficient to get differences between $t_{travel}$ of the last two iterations within the order of $3^{-7}$ second (De Jonge, 1998).

#### 3.1.3.5 Ionospheric delay

Each GNSS provides ionospheric corrections for single-frequency users based on different models, which are broadcast within the satellite navigation signals. For example, GPS uses the Klobuchar model (Klobuchar, 1987), whereas Galileo uses the NeQuick model (European Commission, 2016). These broadcast models are capable of removing

$\sim 50 - 70\%$ of the ionospheric delay.

An alternative solution to the use of models is to use real-time ionospheric mapping to estimate the ionospheric delay, which provide both two-dimensional vTEC and satellite DCBs. The biases are important because they need to be accounted for to make use of the information correctly. Analysis centres within the IGS, such as Centre for Orbit DEtermination (CODE), provide GIMs on a daily basis and the usage of these maps for ionospheric corrections has been validated in several studies. Ionospheric corrections from GIMs were included in Precise Point Positioning (PPP) models in Banville et al. (2014) and Rovira-Garcia et al. (2016), where the results showed improvements in convergence time in both single and Dual-Frequency Precise Point Positioning (DF PPP) of ∼60% over results without using GIM information. Rovira-Garcia et al. (2020) and Zhang et al. (2019) show that sub-meter level positioning accuracies can be achieved in Single-Frequency Precise Point Positioning (SF PPP) with corrections from different GIMs. The benefit of using GIMs over broadcast models to provide ionospheric corrections in SF PPP, DF PPP and SF SPP are presented in Su et al. (2019).

One drawback of using GIMs is that they generally approximate the ionospheric electron density to a single height layer. An elevation-dependent geometry factor is therefore needed to transform the vTEC into sTEC, which may introduce additional errors. An alternative method is to create three-dimensional maps with multiple vertical layers using ionospheric tomography. The impact on SF SPP accuracy of an additional layer in height in GIMs was evaluated by N. Wang et al. (2018). The results show significant improvement when using 2-layer GIMs than single layer maps to provide ionospheric corrections. GPS ionospheric tomography has previously been reported as a valid source to provide ionospheric corrections for SF SPP (Allain and Mitchell, 2009; Allain and Mitchell, 2010). All these methods provide sTEC measurements, from which the ionospheric delay can be retrieved following Equation 3.4.

#### 3.1.3.6 Positioning method

Once all the error terms are addressed, the corrected pseudorange ($\tilde{\rho}$) is now given by:

$$\tilde{\rho} = \rho - p_{sag} + c \times (b_s + b_{clk}^{rel} - TGD) - T - I \tag{3.17}$$

In this work, to compute the position of the receiver, the single-frequency SPP Best Linear Unbiased minimum variance Estimator method, or BLUE method (Teunissen,

2000), is used to calculate the position. This algorithm subtracts the computed pseudo-range from the observed measurements ($\Delta\tilde{\rho} = \tilde{\rho} - p_{meas}$), where $p_{meas}$ is the distance from the given satellite to the estimated receiver position. Thus, the equations for a single epoch can be given as:

$$\underbrace{\begin{bmatrix} \Delta\tilde{\rho}_1 \\ \Delta\tilde{\rho}_2 \\ \vdots \\ \Delta\tilde{\rho}_m \end{bmatrix}}_{y} = \underbrace{\begin{bmatrix} LOS_1(t) & 1 \\ LOS_2(t) & 1 \\ \vdots & \vdots \\ LOS_m(t) & 1 \end{bmatrix}}_{A} \underbrace{\begin{bmatrix} \Delta r_r(t) \\ dt_r \end{bmatrix}}_{x} \tag{3.18}$$

where $LOS$ corresponds to the satellite-receiver line-of-sight unit vector, $\Delta r$ is the estimated receiver position correction, $dt_r$ corresponds to the estimated receiver clock error and $m$ denotes the number of visible satellites with elevation $> 10$ degrees at the given epoch $t$. This elevation cut-off is selected to mitigate the effect of multipath.

Due to signals having different elevations and thus different multipath and noise effects, the quality of the data varies. Therefore, a weighting matrix $W$ is used to account for the different quality of each observation.

$$W = \begin{bmatrix} \frac{1}{\sigma_{i,1}^2} & & \\ & \ddots & \\ & & \frac{1}{\sigma_{i,j}^2} \end{bmatrix} \tag{3.19}$$

where $\sigma_{i,j}$ corresponds to the uncertainty of the observations between satellite $i$ and receiver $j$. The uncertainty of a measurement is determined using an elevation-dependent function that gives larger weights to observations at higher elevations.

$$\sigma_{i,j} \propto \sin(e) \tag{3.20}$$

$x$ is now solved by means of weighted least squares:

$$x = (A^T W A)^{-1} A^T W y \tag{3.21}$$

As the least squares method solves the position of the receiver by iteration, each iteration the position of the receiver is corrected and updated for the next iteration. A maximum of 10 iterations for each epoch is used in this analysis. As the location of each receiver is unknown, for the first iteration of every epoch the receiver is set at $x = y = z = 0$. The estimated clock value ($dt_r$) is a combination of the receiver clock error plus the receiver hardware delay.

While GNSS is a valuable source of observations in the field of ionospheric imaging, it might not be always sufficient to estimate the global ionospheric electron density distribution. This is because, the quality of GNSS-based outputs is influenced by the GNSS receiver network coverage, which determines the amount of available GNSS data. In challenging scenarios, such as regions with sparse ground receiver coverage, the available data may not be sufficient to cover the entire globe with high accuracy. In addition, GNSS only provide sTEC measurements, but not information on the electron distribution along the signal path. In such cases, other data sources can be used to enhance ionospheric tomography imaging (Chapter 4). Two of the most common instruments used to support tomography are ionosondes and Incoherent Scatter Radars (ISRs). Ionosondes can provide an estimate of the full height profile up to the F-layer peak, while Incoherent Scatter Radio detection and ranging (ISR)s can reach altitudes comparable to the topside of the F-layer.

## 3.2 Ionosondes

Ionosondes are vertical sounding instruments used to measure the vertical profile of the ionosphere up to the F2 peak height. The principle of the vertical sounding technique was first introduced in 1925 (Appleton and Barnett, 1925; Breit and Tuve, 1925) with the goal of confirming the existence of the ionosphere. The technique consists of a High Frequency (HF) radio transmitter and a receiver, either co-located (mono-static) or separated from each other (bi-static) (Hunsucker and Hargreaves, 2003). The HF radio signals are reflected from the ionosphere where the plasma frequency corresponds to the transmitted radio frequency.

Ionosondes transmit a discrete set of frequencies generally between $1.5 - 12$ MHz,

and measure the time taken for each signal to be reflected back. Using this time of arrival, the distance to the height where the reflection occurred can be calculated. This provides a profile of plasma frequency (frequency of the signal at reflection) with height. As the plasma frequency is related to the electron density in the ionosphere (Equation 2.10), these ionosonde measurements can be used to calculate the vertical profile of the electron density in the ionosphere. Figure 3.3 shows an idealised ionogram (Hunsucker and Hargreaves, 2003), which is a visual representation of the virtual height of reflection calculated by ionosondes against the transmitted frequency. The height is referred to as "virtual height" due to the delay introduced by the ionosphere, which causes the measured delay to be longer than the real delay. This results in the measured height of the reflection point being larger than the true reflection height.

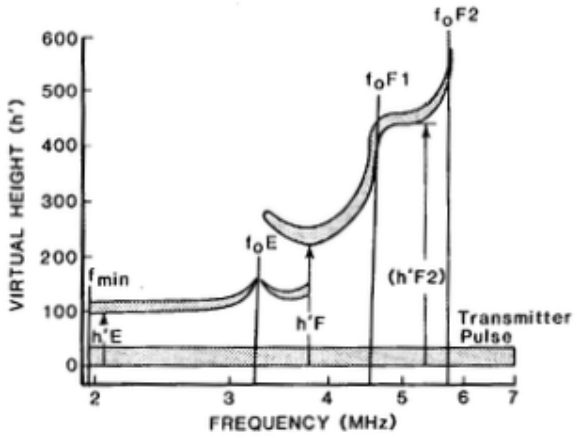


Figure 3.3: Idealised ionogram (Hunsucker and Hargreaves, 2003)

It must be noted that ionosonde observations only reach up to the F2 peak height, as signals exceeding the plasma frequency are not reflected back and propagate through the ionosphere. Therefore, the electron density in the topside of the ionosphere has to be estimated. The technique used in this thesis to estimate this topside ionospheric electron density is by approximating the vertical profile of the topside electron density to a Chapman profile (Chapman, 1931):

$$N_{topside}(h) = N_m(F_2) \times e^{(1-z_h(h)-e^{-z_h(h)})} \quad \text{where} \quad z_h(h) = \frac{h - h_m(F_2)}{H_T} \tag{3.22}$$

where $N_m(F_2)$ is the electron density at the F2 peak height, $h$ is the height of the current

electron density value, $h_m(F_2)$ corresponds to the F2 layer peak height, $H_T$ is known as the scale height and $z_h$ is the normalised height. $N_m(F_2)$ and $h_m(F_2)$ can be directly retrieved from the ionosonde measurements, whereas the $H_T$ is generally calculated from the bottomside electron density profile generated from the measurements (Huang and Reinisch, 2001).

With the advances in technology over the last century, ionosondes have become relatively portable and light devices compared to the first standard ionosondes and other ionospheric sensing devices. The main limitation of ionosondes is the incapability to obtain information of the ionosphere above the maximum ionisation point of the F2 layer. Nevertheless, ionosonde measurements have been widely used for validation of ionospheric sensing methods and models in the past, and continue to be used in current research. Observations from ionosondes are also used alongside GNSS measurements to improve the vertical resolution of ionospheric sensing techniques, in particular ionospheric tomography (Chartier et al., 2012), addressing a traditional weakness when using ground GNSS receivers only.

## 3.3 Incoherent Scatter Radars (ISRs)

Over the last decades, ISRs have been widely used to measure the ionospheric electron density, and to provide independent verification for other experimental techniques such as ionospheric tomography. These radars provide vertical ionospheric electron density profiles, similar to the ionosondes, but for both above and below the F2 peak. These instruments can also scan the ionosphere in slant directions, as opposed to only vertically. In addition, multiple ionospheric parameters, such as electron and ion temperatures, can be inferred from the radar return.

ISRs were first introduced by Gordon (1958). The theory behind ISRs, as described in Beynon and P. J. S. Williams (1978), involves the back scattering of small amounts of energy from ionospheric electron density fluctuations. From the energy scattered back, electron and ion densities, temperature and mass can be obtained. As the energy scattered back is very small, very high precision receivers are needed, which consequently makes the estimation of the parameters very precise. ISRs operate at higher frequencies than ionosondes, typically between 50 MHz to 1000 MHz. As the transmitted frequencies are larger than the ionospheric plasma frequency range ($0.1 - 9$ MHz), the retrieval of electron density height profiles for the entire ionosphere is enabled. The radars consist of steering antennas, which makes it possible to gather electron density distributions along

different paths around the antenna. This feature enables the creation of two-dimensional electron density scans of the radars' sky view. The main ISRs used in ionospheric studies are the following:

- Jicamarca Radio Observatory, Peru (-76.52° longitude and -11.57° latitude)
- Arecibo Observatory, Puerto Rico (-66.45° longitude and 18.20° latitude)
- Millstone Hill radar, Haystack Observatory, USA (-71.29° longitude and 42.37° latitude)
- European Incoherent SCATter (EISCAT) radar, Scandinavia (19.2° longitude and 69.6° latitude, and 16.03° longitude and 78.15° latitude)

Only EISCAT and Millstone Hill radars are introduced in this chapter, as they are the only ISRs relevant to this thesis.

### 3.3.1 EISCAT radar

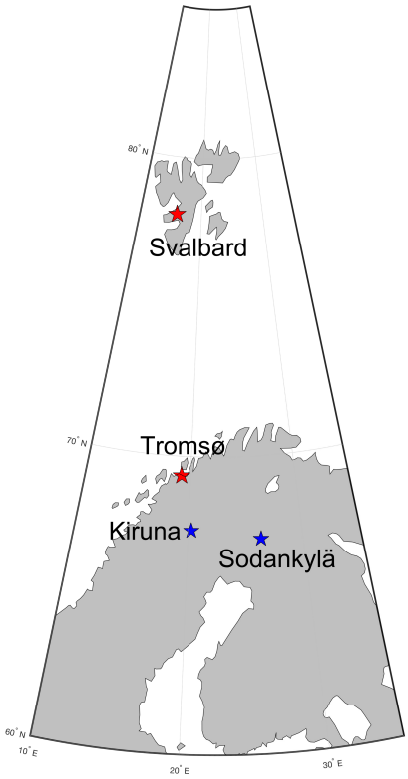


Figure 3.4: EISCAT radar locations.

EISCAT has three radar systems in Scandinavia: two transmitters co-located with their receivers near Tromsø, Norway (19.2° longitude and 69.6° latitude), and another transmitter in Svalbard, Norway (16.03° longitude and 78.15° latitude). Two further receivers at Kiruna in Sweden and Sodankylä in Finland enable the radar to operate as a tristatic system if required (Rishbeth and P. Williams, 1985). The location of each radar is shown in Figure 3.4. The benefit of using a multi-static system is that larger resolutions in height can be achieved by the intersection of two or more beams. Rishbeth and P. Williams (1985) reviewed how physical principles of the ISR sensing technique can be applied for the EISCAT radar in particular, describing how experiments were designed and how data was analysed. EISCAT was first used as an independent verification of ionospheric tomography in 1992, as reported by Pryse and Kersley (1992). EISCAT's coverage extends from the north of Europe up to the north pole, which makes it ideal for studying the polar ionosphere.

### 3.3.2 Millstone Hill radar

The Millstone Hill radar has its transmitter and receiver antennas co-located in the Haystack Observatory, Massachusetts (USA). It was built in 1963, and the physical theory behind the radar's parameter estimation processes and first results were introduced by Evans (1965). The location of the observatory at sub-auroral latitudes, combined with the steerable antenna's operational range, permits observations over a latitude span encompassing the region between the polar and the near-equatorial ionosphere.

In addition to their contribution to the physical understanding of the ionosphere, ISRs have proven to be important instruments in providing independent verification for other experimental techniques such as ionospheric tomography (Pryse and Kersley, 1992; Walker et al., 1996; Meggs et al., 2005; Bust et al., 2007; Van De Kamp, 2013). It must be noted, however, that ISRs need high power transmitters and hardware capable of receiving very weak signals. Therefore, in comparison with other ionospheric measurement instruments, ISR is an expensive sensing tool, which has resulted in only a limited number of radars having been constructed.

## 3.4 Summary

This chapter reviewed some of the most common techniques used to observe the ionospheric electron density distribution.

With the availability of multiple constellations, GNSS has become an important tool for studying the ionosphere. The GNSS constellations are a unique resource for ionospheric measurements as they provide instantaneous global coverage, continuous operation, high temporal resolution and near real-time data acquisition. The ionospheric measurements from GNSS makes use of the delay of the radio signal (due to the electron density) as it propagates through the ionosphere. As this is dependent on the frequency of the signal, it makes multi-frequency GNSS signals an ideal source for ionospheric sensing. These instruments, however, do not provide information about the vertical distribution of electrons along the signal path, which must be supplied from other instruments in order to derive accurate estimations of the ionospheric electron density.

Ionosondes can provide very accurate vertical electron density measurements up to the peak electron density using HF radio signals reflected from the ionosphere. These instruments can be used to retrieve the electron density at different heights by transmitting signals with different discrete frequencies vertically into the ionosphere

and calculating the time taken to receive the reflected signals. The measurements are used to create ionograms that provide height information with varying frequency, which can be translated to electron density. These profiles can be used to validate (Wen et al., 2008) or enhance (Hernández-Pajares et al., 1999) ionospheric tomography.

Incoherent scatter radars are another important instrument used for ionospheric sensing. They measure the small amount of energy of a transmitted signal that is back scattered from electron density structures in the ionosphere. These instruments are capable of sensing the ionospheric electron density with high accuracy, thus making them very reliable tools for ionospheric tomography validation. However, this comes at a high cost due to its power requirements as high power transmitters and hardware capable of receiving very weak signals are needed. ISRs are widely used over different locations, such as at high latitudes (e.g. Scandinavia) (Walker et al., 1996; Meggs et al., 2005; Spencer and Mitchell, 2007) or equatorial regions (Chartier et al., 2012). They are, however, geographically limited to measure only the area over the radar location.

# 4 Ionospheric tomography

## Introduction

The use of radio tomography to determine the distribution and density of free electrons in the ionosphere (ionospheric tomography) was first proposed by Austen et al. in 1986. Advances in the field now enable full three or four-dimensional imaging of the ionosphere as demonstrated in Fremouw et al. (1992), Hernández-Pajares et al. (1998), Mitchell and Spencer (2003), and Bust and Mitchell (2008).

The use of sTEC measurements from a global GNSS ground receiver network in tomography is a powerful method for producing accurate global-scale electron density maps of the ionosphere (Davies and Hartmann, 1997; Jakowski et al., 2001). The technique is widely used within the scientific community for different purposes, such as to better understand the ionosphere and its behaviour, and to provide ionospheric delay corrections for GNSS positioning. Improved availability of data in the last two decades, due to densification of ground-based GNSS receiver networks and the availability of several GNSS systems, allows for more accurate ionospheric mapping, especially over regions with dense GNSS receiver networks.

This chapter explains the theory behind ionospheric tomography, followed by a review of Multi Instrument Data Analysis System (MIDAS), the ionospheric tomography software used for the research described within this thesis. While MIDAS can use different data from different instruments, due to the nature of this research project (i.e. providing ionospheric corrections for GNSS), the discussion is focused on the use of GNSS measurements as the input data source to MIDAS. The chapter closes with an overview of current alternative state of the art in ionospheric tomography software and finally, a summary.

## 4.1 Reconstruction theory

Radio tomography was first introduced by Radon in 1917, while the first experimental work using tomography to estimate the ionospheric electron density was described in Austen et al. (1988). Tomography is an inverse problem (Hounsfield, 1980) that involves the reconstruction of an object of interest from line-integral measurements of

signals passing through the object. It allows to create two, three or four-dimensional images of the object of interest. In the case of ionospheric tomography, the line-integral observations are sTEC measurements, derived from GNSS phase or pseudorange observations:

$$sTEC = \int_S^R N(l)\, dl \tag{4.1}$$

where $N$ is the electron density per unit volume, $l$ the distance along the ray path from satellite (S) to receiver (R) and sTEC is the columnar electron density expressed in TECu, where 1 $TECu = 10^{16}$ electrons/$m^2$. While individual sTEC measurements provide no information about the electron distribution along the ray path, a series of sTEC data from ray paths crossing each other in the ionosphere can be inverted into spatial maps of electron density. sTEC measurements can be used for ionospheric tomography when a GNSS receiver network consisting of a sufficient number of receivers that enables large spatial coverage is available.

In ionospheric tomography, the electron density is assumed constant within a sufficiently small volume around a point (a 'voxel') in the ionosphere. The contribution to the measured sTEC of each length of ray passing through a voxel is then the multiplication of that electron density and the length of the ray path passing through the voxel. The total sTEC of a single ray path is the summation of these segments. For $k$ ray paths and $m$ voxels, this may be expressed as:

$$\vec{y} = \sum_{i=1}^{i=k} \sum_{j=1}^{j=m} A_{i,j} \times x_j \tag{4.2}$$

where $\vec{y}$ contains all the sTEC measurements, $A_{i,j}$ is an array containing the lengths of the $k$ rays within individual $m$ voxels, and $x$ contains the electron density in each of the $m$ voxels. Figure 4.1 shows an illustrated example of voxels and rays in a two-dimensional representation of the ionosphere.

Equation 4.2 can also be expressed in matrix form as:

$$\vec{y} = \mathbf{A}\vec{x} \tag{4.3}$$

where $\mathbf{A}$ is an $k \times m$ matrix of the path lengths within each voxel, $\vec{x}$ is the electron

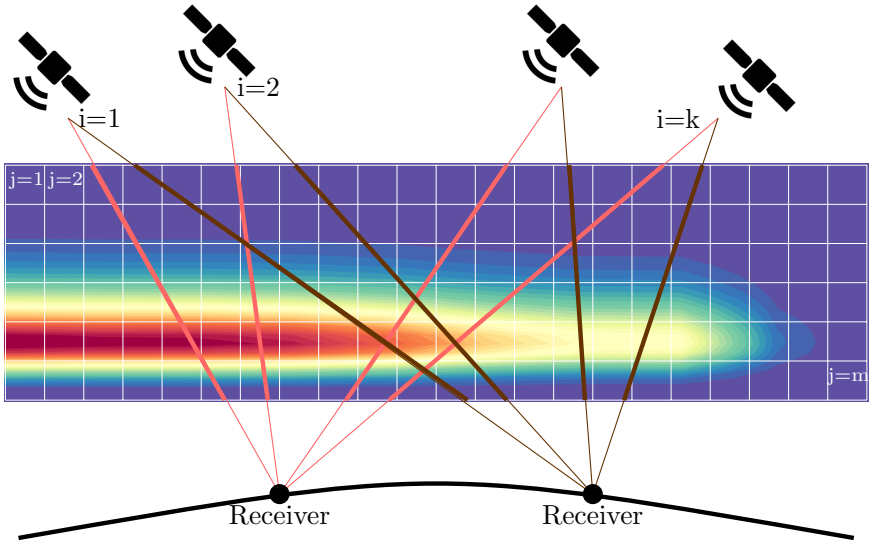


Figure 4.1: Ionospheric tomography example, showing ray paths intersecting a grid of voxels

density within each of the $m$ voxels, and $\vec{y}$ are the $k$ observed sTECs. This gives an inverse problem for which $\vec{x}$ has to be solved.

## 4.2 MIDAS

The Multi-Instrument Data Analysis System (MIDAS) (Mitchell and Spencer, 2003) is a MATLAB software suite that uses data from different instruments to reconstruct the ionospheric electron density distribution using tomography. It is based on the theory introduced in Section 4.1, and can ingest data such as line integral measurements from ground and space-based GNSS observations or ionosonde data. An example of a three-dimensional ionospheric map created using MIDAS is given in Figure 4.2.

While MIDAS can ingest data from many instruments, the main data source for ionospheric tomography with the software has so far been GPS. The algorithm primarily uses two types of data as input to compute the ionospheric image when using GPS (or GNSS) measurements. First, to obtain phase and pseudorange observations from GNSS, Receiver INdependent EXchange (RINEX) files from a list of ground-receivers are used. Second, orbital information for each satellite is retrieved from Standard Product 3 orbit (SP3) files. These data are used to compute the observed ionospheric sTEC measurements ($\vec{y}$) and the corresponding raypath geometry ($\mathbf{A}$), from which three-dimensional images of the electron densities of the ionosphere ($\vec{x}$) are reconstructed.

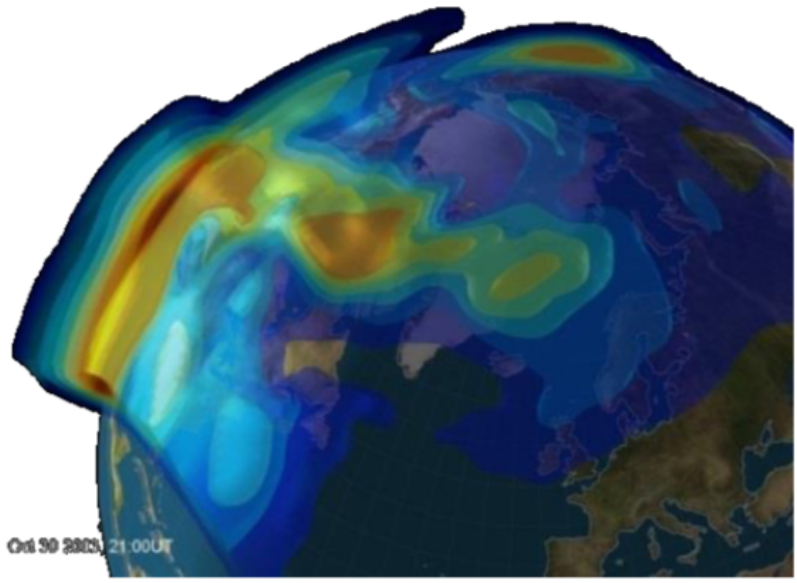

Figure 4.2: Three-dimensional mapping of the ionosphere using MIDAS for October 30, 2003, 21:00 UT, from Mitchell et al. (2013)

### 4.2.1 MIDAS tomography

Ionospheric tomography with MIDAS using GNSS as the source data enables accurate imaging of the electron density. However, it is limited by the satellite-to-receiver geometry when only ground-based receivers are used because of the lack of horizontal ray-paths through the ionosphere; which results in limited information on the vertical distribution of the ionospheric electron density. Another limitation is not having sufficient data to cover the entire geographical area with evenly-distributed receivers. These limitations can cause the problem to have more unknowns than equations, and thus make the inversion underdetermined.

MIDAS algorithm can address this lack of observations from GNSS by using Empirical Orthonormal Functions (EOFs) to map the voxel-based problem into a function-based problem, in either the vertical, the horizontal or in both domains. These functions can provide a realistic approximation of the vertical and horizontal distribution of the electron density to compensate for the possible lack of observations in the reconstruction. The standard MIDAS setup uses both function-based and voxel-based problems, which enables the combination of voxels in the horizontal domain with EOFs in the vertical domain. The vertical orthonormal functions are the singular values derived from a set of

normalised ionospheric vertical profiles either from models such as Chapman (Chapman, 1931), or from external data sources such as ionosondes or ISRs. Figure 4.3 gives an example of 5 Chapman EOFs.

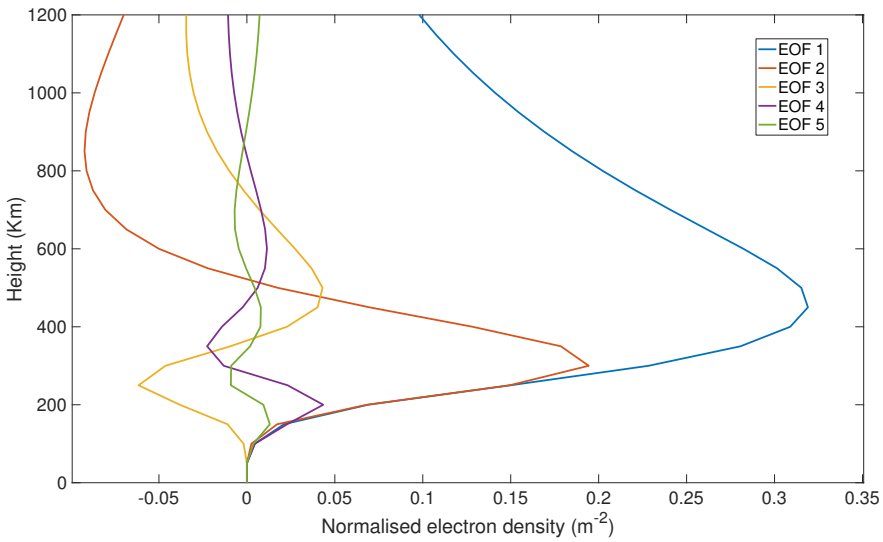


Figure 4.3: Example of 5 EOFs calculated from Chapman vertical profiles.

The EOFs, either vertical or horizontal, are included in the inversion problem as a mapping matrix $\mathbf{M}$, which transforms the problem from voxel-based to one for which the unknowns are the coefficients of the orthonormal basis functions. The problem defined in Equation 4.3 is now expressed mathematically as:

$$\vec{y} = \mathbf{AM}\vec{z} \tag{4.4}$$

where $\vec{z}$ is the unknown coefficients of each orthonormal basis function and matrix $\mathbf{M}$ defines the mapping from a voxel-based representation to a function-based one by using basis functions; such that $\mathbf{AM}$ defines a basis set of line integrations of electron density through the geometry volume defined by $\mathbf{A}$.

The inverse solution may still be unstable because the problem is still ill-posed due to limited data coverage over a given geographical area, which makes the solution unsolvable. To make the problem well-posed, and therefore the solution unique, MIDAS is capable of aiding the inverse problem with various techniques, such as regularisation (Mitchell and Spencer, 2003; Panicciari et al., 2015), Kalman filtering (Spencer and Mitchell, 2007) or data assimilation on a physics-based model (Da Dalt et al., 2014).

In this thesis, only the first version, which uses regularisation techniques, is considered. This option uses the well-established Tikhonov regularisation (Tikhonov and Arsenin, 1977). Instead of selecting all possible values in the geographical space defined by **A**, Tikhonov regularisation only selects the subset with reliable values — i.e. with best receiver coverage. To do this, Tikhonov introduced the following parametric cost function:

$$f(z) = ||\vec{y} - \mathbf{AM}\vec{z}||^2 + \eta||\mathbf{RM}\vec{z}||^2 \tag{4.5}$$

where $f$ is the cost function of the method with respect to $\vec{z}$, $\eta$ is the regularisation tuning parameter and **R** refers to the regularisation matrix. The inversion is now solved by the Regularised Least Square (RLS) technique, which minimises the cost of $f(z)$:

$$\vec{z} = (\mathbf{M}^T\mathbf{A}^T\mathbf{AM} + \eta\mathbf{M}^T\mathbf{R}^T\mathbf{RM})^{-1}\mathbf{A}^T\mathbf{M}^T\vec{y} \tag{4.6}$$

It must be noted that while this approach enables a unique solution to be obtained, it is now highly dependent on the regularisation. This is because the $\eta$ parameter sets the influence of the regularisation on the inversion. A small $\eta$ value will reduce the effect of the regularisation, which, if the problem is ill-conditioned, the solution may enhance small artefacts and noise in the solution. Conversely, as the $\eta$ value gets bigger, the regularisation will drive the solution according to **R**. This means, if $\eta$ is too big, the regularisation would smoothen the solution and small structures in the electron density would disappear from the reconstructed images.

Once $\vec{z}$ is obtained, the electron density $\vec{x}$ is calculated by combining Equations 4.3 and 4.4:

$$\vec{x} = \mathbf{M}\vec{z} \tag{4.7}$$

Using $\vec{x}$, it is now possible to evaluate the accuracy of the inverse problem by calculating the predicted observation $\widehat{y}$ and comparing with real observed data $\vec{y}$.

$$\widehat{y} = \mathbf{A}\vec{x} \tag{4.8}$$

For a successful tomographic inversion, the predicted observation has to be as close

to the real observed data vector $\vec{y}$ as possible. Any differences between $\widehat{y}$ and $\vec{y}$ can be due to a number of factors, such as poor data coverage, poor data quality or a poorly defined $\mathbf{R}$ (Panicciari et al., 2015).

### 4.2.2 TEC calibration

As mentioned in Section 3.1.2, the sTEC observations coming from either $\rho_{GF}$, $\varphi_{GF}$ or CCL are offset by either DCBs or phase ambiguities. MIDAS addresses the impact these parameters may have on the estimation of $\vec{z}$ by removing them through observation-differencing. To calibrate sTEC measurements, all frequency dependent terms and constants over time for each satellite pass, such as phase ambiguities and DCBs, are removed using the ray differencing technique (Andreeva et al., 1992). This method computes the time-differences in raypath geometries ($\mathbf{A}$) and measurements ($\vec{y}$):

$$\mathbf{D}\vec{y} = \mathbf{D}(\mathbf{A}\vec{x}) \tag{4.9}$$

$$\mathbf{D}\vec{y} = (\mathbf{DA})\vec{x} + \mathbf{A}(\mathbf{D}\vec{x}) \tag{4.10}$$

where $\mathbf{D}$ corresponds to the matrix containing the differential rays over time. If short enough time periods are considered, the ionospheric electron density can be assumed to remain constant, thus $\mathbf{D}\vec{x} \simeq 0$. During this period, all offsets in $\vec{y}$, such as DCBs, are also assumed to remain constant, isolating the sTEC information within $\vec{y}$. This means the $\mathbf{D}$ matrix only applies to $\mathbf{A}$ and $\vec{y}$ parameters.

$$\mathbf{D}\vec{y} = \mathbf{DA}\vec{x} \tag{4.11}$$

Combining Equation 4.11 with Equation 4.6, $\vec{z}$ can now be defined as:

$$\vec{z} = (\mathbf{M}^T\mathbf{A}^T\mathbf{D}^T\mathbf{DAM} + \eta\mathbf{D}^T\mathbf{R}^T\mathbf{M}^T\mathbf{RMD})^{-1}\mathbf{M}^T\mathbf{A}^T\mathbf{D}^T\mathbf{D}\vec{y} \tag{4.12}$$

Solving this equation for $\vec{z}$ and using Equation 4.7, the tomographic algorithm can now provide absolute $\vec{x}$ values without any biases from uncalibrated observations.

As mentioned before, apart from GPS observations (see e.g. Bernhardt et al., 1998; Materassi and Mitchell, 2005; Rose et al., 2011), additional measurements from different instruments can be used in MIDAS as input or validation data. These additional measurements generally come from ionosondes and ISRs, introduced earlier in Chapter 3. The use of these instruments with MIDAS was demonstrated in Chartier et al. (2012),

where ionosonde peak densities were used as absolute point measurements in addition to GPS data, and observations from the Jicamarca ISR, were used to assess the accuracy of the method. In Meggs et al. (2005) and Spencer and Mitchell (2007), data from the EISCAT radar was used as an independent verification of MIDAS images over the Northern hemisphere. More details on the use of different data sources in MIDAS are summarised in Mitchell and Spencer (2003).

## 4.3 State of the art

This section gives a brief review on other most relevant ionospheric tomography methods currently available.

### 4.3.1 IDA4D

Ionospheric Data Assimilation Four-Dimensional (IDA4D) (Bust et al., 2004) was developed by the Applied Research Laboratories at the University of Texas. It is based on the Four-Dimensional VARiational (4DVAR) data assimilation technique (Daley, 1991), where the underlying idea is to create a method to combine a background model with actual measurement data. It is capable of ingesting different types of ionospheric electron density measurements, such as ground and space-based GPS, ionosondes and radars. The background specification for the IDA4D algorithm can be based on empirical models or global representations of the ionosphere, which is used as the initial guess. Using a minimisation technique that takes the data, its deviation from the background model and their covariances into account, the three-dimensional electron density distribution is estimated. These images are then projected forward in time through a Kalman filter, where they are used as the background model for the next step.

The main advantage of IDA4D is the flexibility it provides. The three-dimensional electron density grid can be entirely irregular, which makes it possible to increase or decrease the resolution of the results in given regions without compromising the image quality. In addition, 4DVAR can determine the influence the input measurements and background model have on the results using their covariances. In comparison to MIDAS, the main drawback of IDA4D is the need of a background ionosphere to be used as an initial guess, which introduces a potential source of noise and errors. The use of a Kalman filter instead of a regularisation technique to estimate the electron density is another difference compared to the version of MIDAS used in this thesis.

### 4.3.2 GAIM

The Global Assimilative Ionospheric Model (GAIM) (C. Wang et al., 2004) was developed by the University of Southern California and Jet Propulsion Laboratory. GAIM is based on a physics-based ionospheric model, which is then refined by the 4DVAR data assimilation technique to retrieve the 3-dimensional electron density. Line-of-sight TEC measurements from different ionospheric sensing instruments, such as ionosondes and ground and space-based GPS receivers are provided as observed inputs into the 4DVAR assimilation. GAIM uses electron density measurements from a database of post-processed observations to adjust the parameters of the physics-based model, such as ion production rates, temperature and neutral wind. This updated model is then combined with available real-time measurements in a Kalman filter-based assimilation. GAIM can provide near-real time and short-term forecasts of ionospheric electron density distributions.

The use of the updated physics-based model is the main feature of GAIM. As the model is updated with real measurements, the electron density distribution described by GAIM becomes increasingly representative of the real conditions, which consequently improves the convergence of the Kalman filter. However, the mandatory use of a physics-based model and the need for its continuous update can be a potential source of errors, and can be a drawback when compared to other tomography techniques. As with IDA4D, the need of a background ionosphere (a physics-based model in this case) and the use of a Kalman filter instead of a regularisation technique to estimate the electron density are the main differences in GAIM compared to the MIDAS version used in this work.

### 4.3.3 Fast PPP

Fast Precise Point Positioning (Fast-PPP) is a method that provides ionospheric corrections for GNSS in real-time (Rovira-Garcia et al., 2015). It was developed by the Research Group of Astronomy and Geomatics (gAGE) at the Universitat Politècnica de Catalunya (UPC). This method uses available GPS TEC measurements to estimate the ionospheric electron density and satellite and receiver DCBs. The method consist of three Kalman filters. In the first Kalman filter, the satellite and receiver clock corrections are estimated. The second Kalman filter estimates the slow-varying parameters — the tropospheric delay, carrier-phase ambiguities and satellite orbit corrections. The ambiguities are used to adjust the geometry-free phase measurements ($\varphi_{GF}$) and calculate the absolute sTEC. The sTEC measurements are then ingested into the third

Kalman filter, which performs two-layer ionospheric tomography and refines the DCBs. Fast-PPP provides vTEC for two vertical layers of the ionosphere with limits at 50, 500 and 5000 km from the Earth's surface, which provides higher accuracy than single-layer tomography (Juan et al., 1997; Allain and Mitchell, 2009). The accuracy of the DCBs and ionospheric delays are typically $\simeq 1$ TECu, which allows this method to provide ionospheric corrections for precise positioning applications, such as PPP.

The main benefit of using Fast-PPP is that, apart from the ionospheric electron density and DCBs, it also continuously estimates GNSS-related parameters such as phase ambiguities, satellite orbits and clock errors. In addition, it does not require a background model ionosphere as an initial guess. However, Fast-PPP needs to estimate the phase ambiguities in the second filter to calibrate the phase sTEC measurements used for ionospheric tomography, which can introduce additional errors to the estimated electron density. This tomography technique also only solves for the electron distribution over a two-layer grid, while other methods, such as MIDAS, can estimate the electron density distribution over a larger number of vertical layers.

## 4.4 Summary

This chapter reviewed the theory behind ionospheric tomography — an imaging technique that reconstructs the ionospheric electron density from line-integral measurements in an inversion process. A well established data source for ionospheric tomography is sTEC derived from GNSS satellite-to-receiver ray-paths, which can be fed into the inversion method.

The ionospheric tomography algorithm used in this thesis, MIDAS, can ingest both phase and pseudorange dual-frequency observations of GNSS to derive either calibrated or uncalibrated (relative) sTEC measurements. The measurements are then inverted to reconstruct four-dimensional images of the ionospheric electron density as a function of latitude, longitude, height and time. This makes MIDAS an ideal method for sensing the global ionospheric electron density.

In addition to MIDAS, this chapter also provided an overview of alternative ionospheric tomography methods currently in use. IDA4D and GAIM algorithms, based on the 4DVAR data assimilation technique, use a background ionospheric model as a reference and assimilate TEC measurements from different sources into this background ionosphere model. The Fast-PPP method, in contrast, does not use any ionospheric

model, but combines three different Kalman filters to calculate satellite and ionospheric corrections for GNSS. The first filter estimates the satellite and receiver clock errors, while the second calculates the tropospheric delays, phase ambiguities and satellite orbit corrections. In the final Kalman filter, two-layer ionospheric electron density maps and satellite DCBs are generated from phase observations. The corrections from this techniques can be used in application such as PPP.

# 5 Ionospheric tomography evaluation

## Introduction

Assessing the accuracy of tomographic algorithms is a challenging task as no reference specification is available to define the true ionosphere. Ionospheric tomography is typically verified using other independent experimental data sources as has been demonstrated in previous studies, such as incoherent scatter radars (Pryse and Kersley, 1992; Walker et al., 1996; Mitchell et al., 1995; Meggs et al., 2005) and ionosondes (Hernández-Pajares et al., 1998; Lee et al., 2008). However, such a verification is complicated by the fact that all instruments have associated measurement errors, and the evaluation is limited by the accuracy of the instruments. Furthermore, the majority of these systems are localised and do not cover large regions of the Earth.

This chapter outlines a new simulation approach that enables the evaluation of the quality of ionospheric tomography inversions. The approach uses two-dimensional ionospheric electron density distributions derived from ISR (see Section 3.3) and ionosonde (see Section 3.2) observations, which are spatially extrapolated to create a realistic 3-dimensional ionospheric representation. sTEC measurements are then simulated by integrating the electron density along signal paths propagating this ionosphere, defined by real geometries between GPS satellites and ground receivers. This data set, for which the reference ionosphere is now known, is used as an input to MIDAS to estimate the spatial distribution of the ionospheric electron density. The reconstructed ionospheric maps are then compared with the reference ionosphere to calculate the difference between the images and the reference. Three of the most critical issues when imaging the ionosphere with GPS are tested: the impact of satellite and receiver DCBs, receiver coverage of the geographical grid, and the lack of horizontal rays. MIDAS is evaluated for three geographic regions with differing ground-receiver networks, which evaluates the impact ground-receiver coverage has on the reconstructions.

The chapter is structured as follows. Section 5.1 gives a brief introduction to the evaluation framework. Section 5.2 discusses the creation of the ionospheric models

and introduces the simulated observations. The important parameters needed for the reconstruction are then described and selected in Section 5.3. Finally, the results are shown and discussed in Section 5.4. The chapter is concluded with a summary.

## 5.1 The evaluation framework

The framework used to evaluate the inversion outputs of MIDAS is based on ISR two-dimensional electron density distributions across latitude and height, and vertical ionosonde observations. These maps are used to create a reference ionosphere which can be used to find the best approach for imaging the ionosphere with MIDAS and to assess its accuracy. Data from two different ISRs and co-located ionosondes are used in this chapter. The first is the the EISCAT radar located in Scandinavia, while the second ISR is located at the Millstone Hill observatory in Massachusetts, USA. The ISRs enable two different models to be created that represent the different ionospheric electron density conditions observed in these regions.

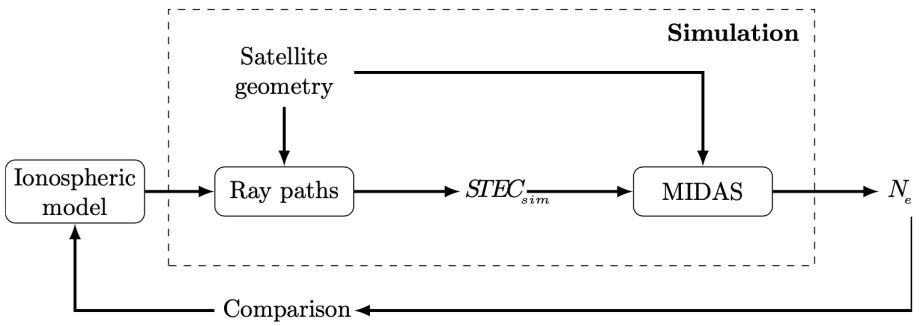


Figure 5.1: Flowchart of the evaluation method described in this chapter.

The flowchart in Figure 5.1 presents the simulation framework used for assessing MIDAS. Simulated sTEC measurements ($STEC_{sim}$ in Figure 5.1) are obtained by integrating through the ionospheric representation (Ionospheric model in Figure 5.1) using real satellite-receiver geometries for the ray paths (Ray paths in Figure 5.1). These measurements are then input to MIDAS to reconstruct and estimate the three-dimensional electron density using tomography ($N_{estimated}$ in Figure 5.1). The accuracy of MIDAS is evaluated by comparing the $N_{estimated}$ against the ionospheric model.

It is helpful at this stage to define some of the terminology used in this chapter.

'Ionospheric model' refers to the three-dimensional distribution of the ionospheric electron density generated using ISR two-dimensional distributions and ionosonde vertical distributions. The model is considered to be the reference ionosphere that is used to test the tomography procedure and against which the inversions are compared. 'Simulation' refers to the creation of artificial observations ($STEC_{sim}$ in the flowchart) of the ionospheric model, which are used as an input to MIDAS. 'Reconstruction' refers to the use of these simulated observations to create a representation of the ionosphere by MIDAS ($N_{estimated}$ in the flowchart).

## 5.2 The reference ionospheric models and simulated observations

### 5.2.1 Specification of the reference ionosphere

As mentioned before, two reference ionospheric models are created using observations from two different ISRs and co-located ionosondes. The models are created for the evaluation of MIDAS as they provide more realistic electron density values and structures than the ones provided by a statistical model such as IRI-2016. This is important as it allows to assess the achievable accuracy of MIDAS in conditions as close to reality as possible.

The EISCAT measurements were obtained for 07 January 2002 12:30 UT and used to image the ionospheric electron density from latitude 64°-78° N at longitude 19° E. The altitude range of the image is from 80-600 km altitude (Figure 5.2a)). The Millstone Hill ISR measurements were gathered at 16:15 UT on 30 July 2010, as seen in Figure 5.2b). The data measured the electron density of the ionosphere from latitude 42°-48° N at longitude 72° W, and 80-600 km altitude.

As ISRs only provide two-dimensional representations of the ionospheric electron density, the data from these radars must be extended over a larger grid to create three-dimensional ionospheric representation, which are created using the following 4 steps:

1. First, a three-dimensional ionospheric background distributions is created using the IRI-2016 model.

2. The vertical electron density profile of this background model is augmented by normalised ionosonde electron density values from co-located ionosondes. This

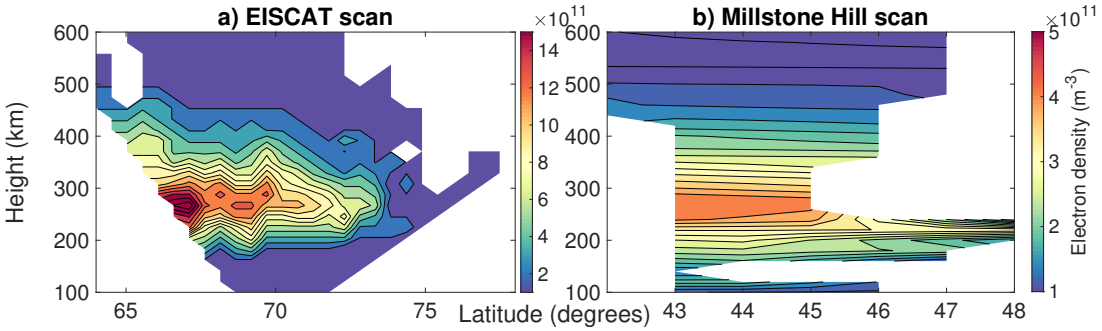


Figure 5.2: **a)** Original EISCAT radar electron density distribution from 2002-01-07 at 12:30 UT and **b)** Original Millstone Hill ISR electron density distribution from 2010-07-30 at 16:15 UT.

is performed by normalising the electron density profile from the ionosonde, and multiplying it with the densities in the background IRI model.

3. The electron density values from the ISRs are added at their respective coordinates and heights, and the edges of the grid are described by the background ionosphere derived from IRI and ionosonde data.

4. Finally, linear interpolation is used to define gaps in the grid between regions described by the ISR electron density and boundaries described by the IRI model.

The model derived from EISCAT is extended to 30° - 80° N latitudes, 15° W - 40° E longitude and up to 800 km altitude. The second ionospheric model, created with observations from the Millstone Hill ISR, is extended to cover latitudes from from 20° - 70° N, longitudes from 125° - 70° W and up to 800 km altitude.

The two ISR are located in different latitudes, EISCAT is located in high-latitude whereas Millstone Hills is in mid-latitude. Therefore, each model provides information on different ionospheric conditions. EISCAT model shows more spatial variability in the electron density distribution and will therefore be more challenging to reconstruct using ionospheric tomography. Millstone Hill model, on the other hand, shows a very quiet ionosphere, and will provide a baseline of the expected performance of MIDAS under stable conditions. Figure 5.3a) shows a latitudinal slice for the EISCAT-based model (22° E longitude) and Figure 5.3b) for the Millstone Hill-based model (72° W longitude).

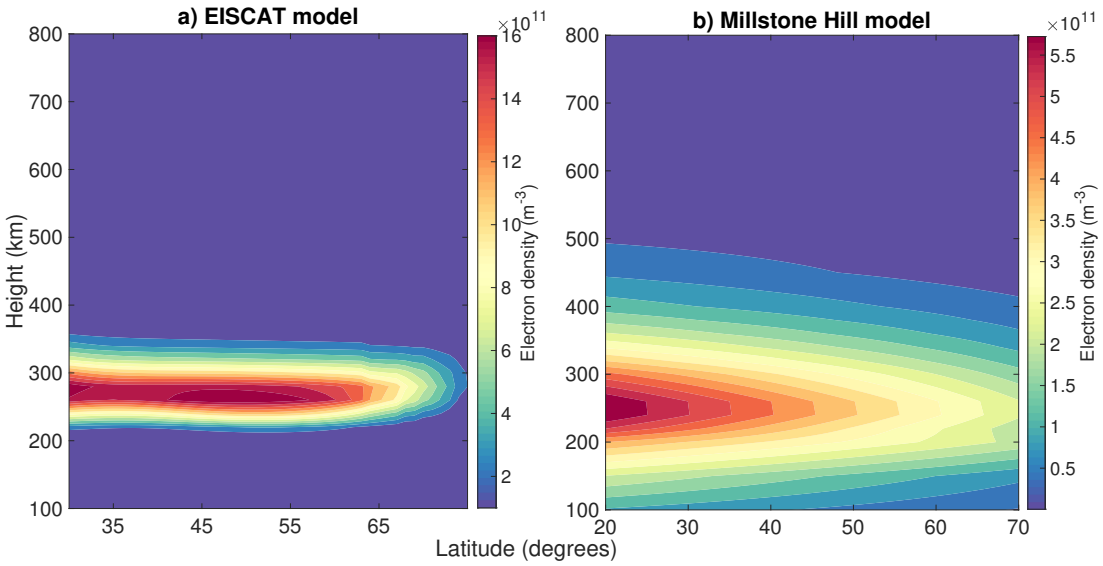


Figure 5.3: **a)** EISCAT ionospheric model's latitudinal slice at 22° E longitude derived from measurements obtained on 2002-01-07 at 12:30 UT, and **b)** Millstone Hill input model's latitudinal slice at 72° W longitude derived from measurements obtained on 2010-07-30 at 16:15 UT.

### 5.2.2 Simulated observations associated with the reference ionosphere

The two ionospheric models making up the reference ionosphere are used to test three of the most critical issues when imaging the ionosphere with GPS: the impact of satellite and receiver DCBs, poor receiver coverage of the geographical grid, and the lack of horizontal rays that provide information on the vertical distribution of the electron density. If the algorithm is not robust against DCBs, the reconstructed electron density may be shifted by a constant value proportional to the biases. Meanwhile, an uneven coverage or lack of horizontal rays may harm the horizontal and/or vertical accuracy of the reconstructed ionosphere. It is important to note that observations from GPS only are used in this chapter.

Following the flowchart in Figure 5.1, once the ionospheric models are defined, the first step in the simulation framework is to calculate the simulated GPS sTEC measurements, which provide input data for MIDAS. The electron density given by the ionospheric models is integrated along satellite-to-receiver ray paths propagating the ionosphere for a set of actual satellite positions and receiver locations. To evaluate the impact of DCBs, real satellite DCBs from CODE and normally distributed random receiver DCBs ($\mu = 0$ and $\sigma = 10$ TECu) are added to each TEC measurement to make

the simulated observations realistic. The effect, if any, that these satellite and receiver DCBs have on the reconstructions is then analysed.

The effect of the density and distribution of the GPS ground receivers is tested by using three receiver networks in three different geographical regions: Europe, North Asia and North America. These regions are selected as they present very different ground-receiver geographical distributions, which are shown in Figure 5.4. The cyan dots represent the GPS receiver positions in each region, and the highlighted areas are regions with higher receiver densities used later in Section 5.4. The impact of the receiver density in each of these three different regions is analysed using the two ionospheric models in Section 5.2.1, separately. This provides information about the influence of receiver distribution and density on the reconstructions of each reference model.

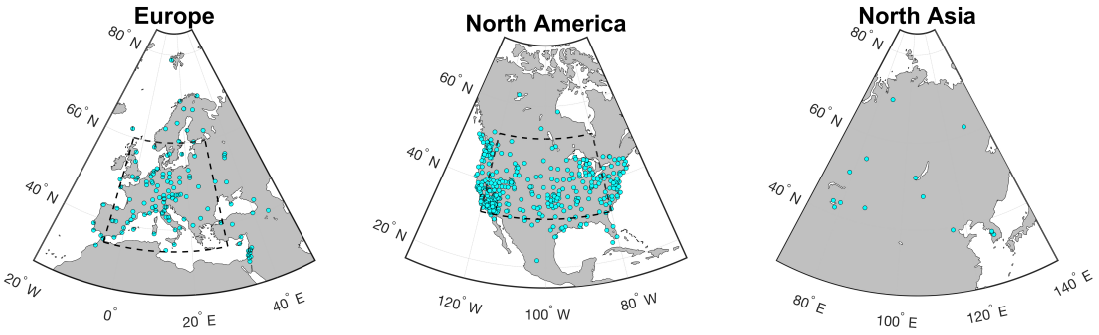


Figure 5.4: Location of the GPS receivers used for the reconstruction.

## 5.3 Selection of optimal parameters for MIDAS

MIDAS requires the configuration of certain parameters — i.e. the desired electron density image size and resolution, and the source and number of EOFs. Therefore, once the input observations for the reconstruction are simulated (using the ISR/IRI/ionosonde model), the two critical parameters within the MIDAS algorithm need to be configured to optimise the performance of MIDAS.

### 5.3.1 Grid resolution

The first step after creating the ionospheric models and choosing the receiver networks is determining the three-dimensional grid resolution to be used for each experiment. The aim is to select the resolution that provides the most accurate images for each

ground-receiver configuration. This is done by conducting a receiver density analysis, where the performance of ionospheric reconstructions with different grid resolutions and numbers of receivers are evaluated. For this analysis, idealised, evenly distributed receiver networks are considered for all regions (Europe, North Asia and North America), and sTEC measurements are simulated from the EISCAT reference ionosphere model as described in Section 5.2.2. These measurements are inverted with MIDAS into three-dimensional ionospheric maps, which are compared with the reference model by computing mean errors in vTEC relative to the reference ionosphere. Figure 5.5 shows three examples of idealised receiver densities used, where the receivers are evenly distributed over Europe.

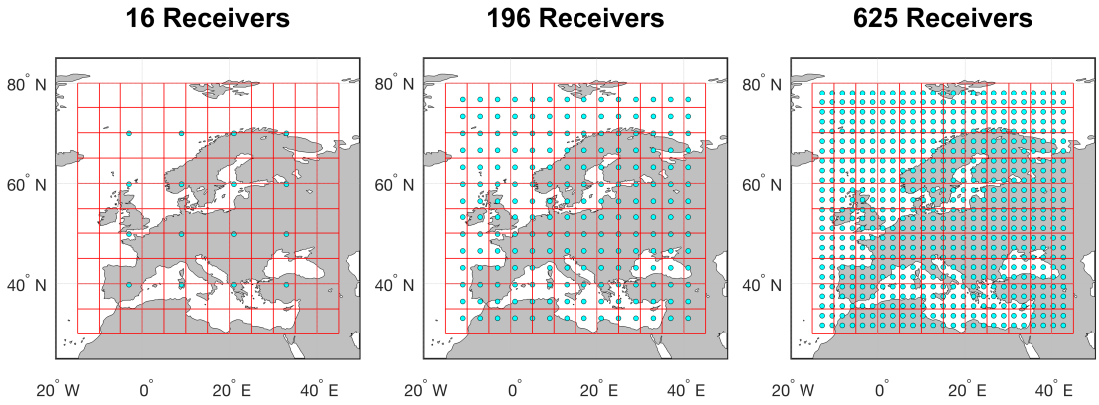


Figure 5.5: Three examples of the receivers distribution over the grid and 5x5 degree bins.

In order to provide a comparison between results of this investigation and a realistic ground receiver distribution, results with the receiver distributions given in Figure 5.4 are also analysed. The grids for the receiver networks are divided into 5x5 degree latitude and longitude bins (see Figure 5.5), and the number of receivers per bin is calculated. This analysis provides a close approximation to the grid resolution that is required, depending on the receiver density and distribution of each scenario.

The simulation reconstructs the ionospheric electron density with 5, 2, 1 and 0.5 degree steps in latitude and longitude and using from 4 to 625 receivers in total equally distributed over the region. Figure 5.6 presents the results from the experiment. The mean (diamond) and standard deviation (line) of the number of receivers per bin for each of the three regions from Figure 5.4 is shown in Figure 5.6a). Mean errors in vTEC in the idealised scenario are presented as a function of number of receivers per bin in Figure 5.6b).

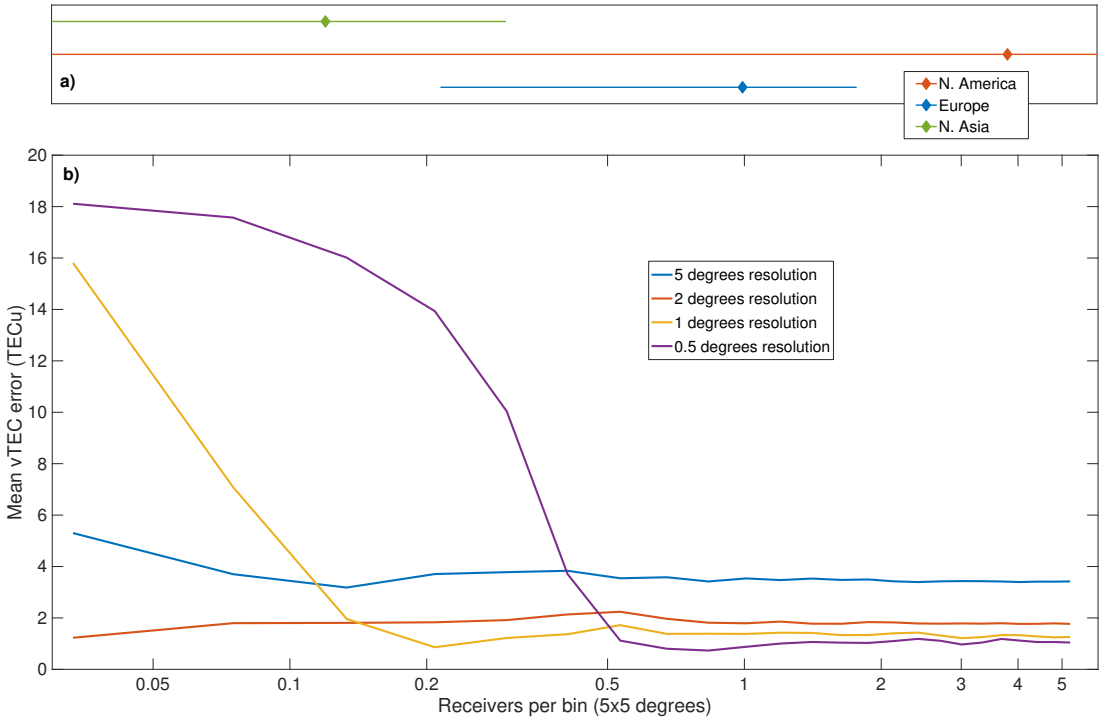


Figure 5.6: **a)** Mean and standard deviation of receivers per bin for the three scenarios under study. **b)** Mean error in vTEC for different numbers of receivers within each 5x5 degree bin. The horizontal axis has a logarithmic scale.

It can be seen from Figure 5.6b) that there is a significant improvement when moving from a reconstruction with 5° resolution to one with 2° resolution for all receiver densities. Errors with 1° resolution stay lower than 2° for receiver densities up to 0.2 receivers per bin, but starts to increase rapidly for receiver densities lower than this. The difference between the vTEC errors when using 1° and 0.5° steps is very small (around 0.2 TECu) for receiver densities $> 1$ receivers per bin. The errors increase dramatically for 1° and 0.5° grids with low receiver density ($< 0.2$ receivers per bin), which is due to insufficient data being available to properly reconstruct the ionosphere at such high resolutions. It is worth mentioning that the higher the resolution of the reconstructed ionospheric electron density, the longer the computational time needed to create the image. Considering the results in Figure 5.6, a resolution of 1° degree in latitude and longitude is selected for Europe and North America, whereas a step of 2° is used in North Asia as it has a lower density of receivers compared to the other two regions.

It must be noted that the distribution of the receivers in this experiment is optimal

in each of the 4 simulated cases, as the receivers are evenly distributed over the region. In reality, the receivers are not as evenly distributed, and the results over regions with sparse receiver coverage will not be as good as in this idealised experiment.

### 5.3.2 Orthonormal basis functions

As introduced in Section 4.2, one of the key features of MIDAS is the use of EOFs in the vertical domain. These functions provide a realistic approximation of the vertical electron density profile to compensate for the lack of vertical accuracy in the reconstruction. Depending on the region of the ISR used to create each ionospheric model, an ionosonde measurement close to the time of the ISR observation (Chilton for EISCAT model and Boulder for Millstone Hill model) is used to calculate the EOFs. As the ionosonde observations only reach up to the F2 peak height, the topside of the ionosphere had to be modelled using the Chapman profile as introduced in Section 3.2. The parameters to calculate the profile are however unknown, and calibration is therefore required. A novel approach to calibrate the ionosonde using accurate vTEC values from MIDAS reconstructions is introduced in this chapter. This approach aims to match the vTEC retrieved from MIDAS reconstructions at the location of the given ionosonde to the vTEC obtained from the ionosonde once the topside profile is calculated. The scale heights, ($H_T$), needed to reconstruct the topsides are calculated (see Equation 3.22). These values are retrieved by iteration. The ($H_T$) value that makes the ionosonde full profile vTEC closer to the MIDAS vTEC at each grid point is used to create new Chapman function. These functions are used to retrieve the EOFs that aid MIDAS. This novel method is later referred to as topside calibrated ionosonde. The results using this method and the full ionosonde profiles provided by each instrument manufacturer as sources to calculate the EOFs for MIDAS are later compared in Section 5.4.3. Only 1 and 2 EOFs are used in MIDAS in this analysis.

## 5.4 Results

This section presents the results from the analysis of DCB estimation, and of horizontal and vertical accuracy of MIDAS electron density for the six reconstructed ionospheric images (three regions with different receiver distributions (Figure 5.4) using two ionospheric models). For clarity, the results concerning each critical feature mentioned in Section 5.2.2 – bias estimation, horizontal and vertical accuracy – are investigated separately.

### 5.4.1 Bias estimation

The impact of the satellite/receiver combined DCBs on MIDAS ionospheric electron density reconstructions is first analysed. The errors between the combined DCBs introduced in each simulated sTEC measurement used as input data, and the combined DCBs retrieved from MIDAS are presented here. Only results from Europe are considered for simplicity.

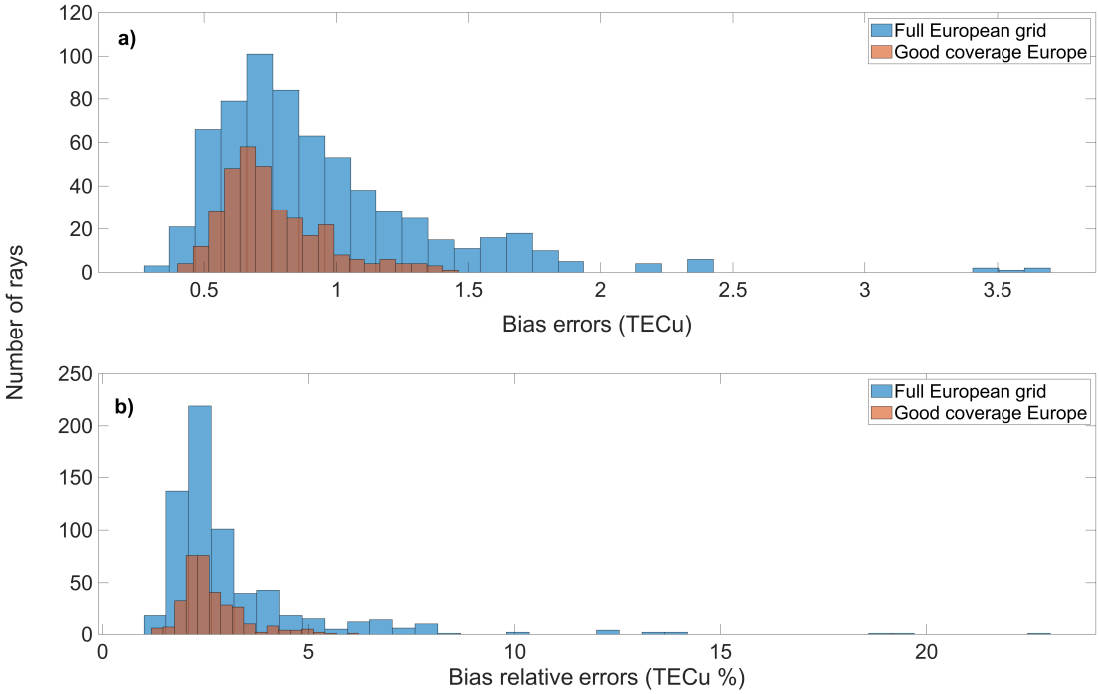


Figure 5.7: Histograms of **a)** DCB estimation errors and **b)** DCB estimation errors percentage, for each ray over Europe.

The satellite and receiver combined DCBs are calculated following the theory introduced in Section 3.1.2.2 (see Equation 3.10). MIDAS calibrates for these biases during the inversion process by using the ray-differencing technique as described in Section 4.2.2. Figure 5.7a) shows the errors between the calculated and the input DCBs for all the satellite-receiver pairs in two areas, the full European grid and a smaller area in central Europe with higher receiver density than the full European region (see highlighted area in Figure 5.4). This region is referred to as the 'good coverage region'. The relative error is calculated by comparing the absolute value of the DCB errors to the measured sTEC of that path. Figure 5.7b) shows how well the biases are estimated for each satellite-receiver pair. The mean of the errors in both areas is approximately

2% of the total sTEC. Approximately 99% of the rays that are in the good coverage region have errors less than 5% of the total sTEC. This generally accounts for errors $< 1$ TECu in mid-latitude regions, which demonstrates the accuracy of MIDAS in DCB estimation.

In order to test if bias estimation errors depend on the measured sTEC, the values of the simulated sTEC observations for each ray-path are multiplied by 10 in the next analysis, without modifying the bias values. Figure 5.8 shows the absolute and relative errors in DCB estimation for results with enhanced sTEC.

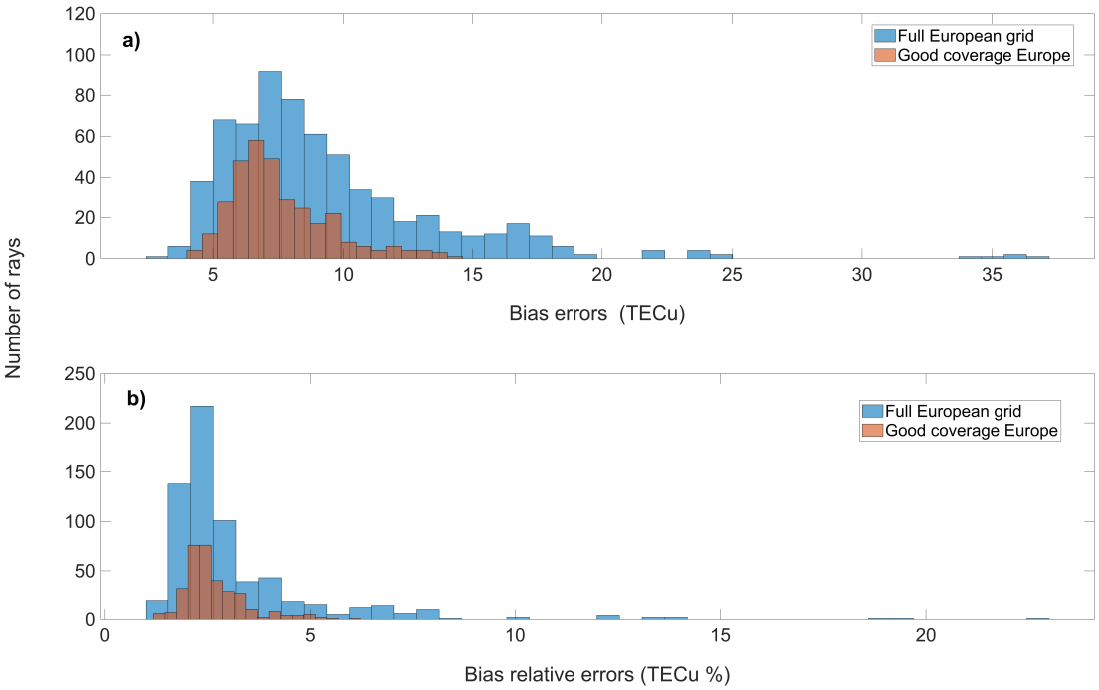


Figure 5.8: Histograms of **a)** DCB estimation errors and **b)** DCB estimation errors percentage, for each ray over Europe after multiplying the TEC values of the simulated observations by 10.

By comparing Figure 5.7 and Figure 5.8, it can be seen that the absolute errors in DCB estimation have increased by a factor of 10 in accordance with the increase in sTEC, without changing the error percentage. Table 5.1 shows numerical mean and standard deviation values for the results shown in Figures 5.7 and 5.8, which also shows the increase in the values by a factor of 10 corresponding to increase in sTEC. This means that the errors do not depend on the values of the DCBs, but on the values of the sTEC.

Table 5.1: Mean and STD of errors in DCB estimation.

| | **Full European grid** | | | | **Good coverage region Europe** | | | |
|---|---|---|---|---|---|---|---|---|
| | Absolute error | | Relative error | | Absolute error | | Relative error | |
| | sTEC | 10 * sTEC | sTEC | 10 * sTEC | sTEC | 10 * sTEC | sTEC | 10 * sTEC |
| **Mean (TECu)** | 0.938 | 9.388 | 3.176% | 3.175% | 0.7564 | 7.564 | 2.665% | 2.665% |
| **STD (TECu)** | 0.443 | 4.429 | 2.148% | 2.147% | 0.194 | 1.942 | 0.751% | 0.751% |

Therefore, in order to analyse the effect the inversion method has on the DCB estimation, reconstructions from MIDAS using simulated measurements that are biased and unbiased by DCBs are compared. From Figure 5.9, it can be seen that vTEC reconstructions in MIDAS from biased and unbiased sTEC simulations are the same. This proves that the errors seen in Figure 5.7 and Figure 5.8 are not caused by the DCBs, and that the method is therefore robust for bias estimation.

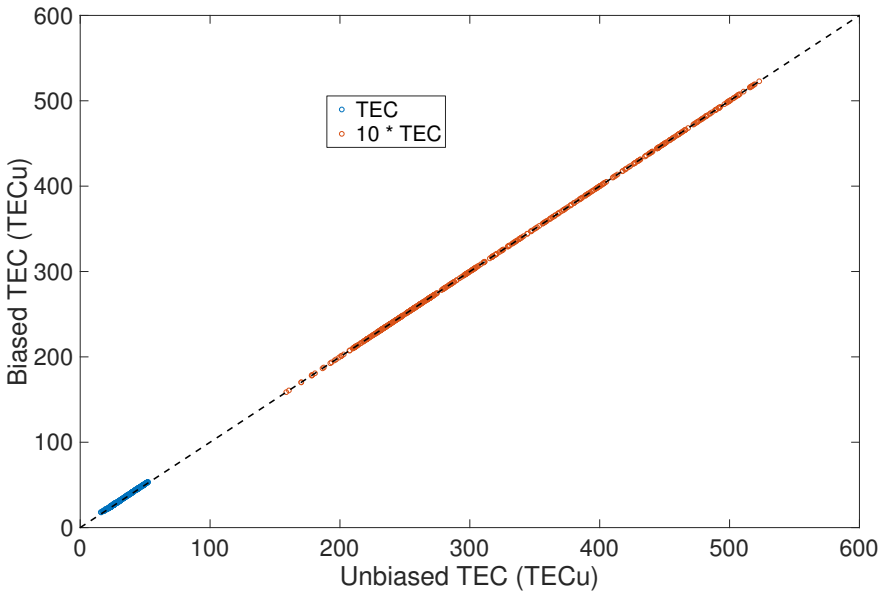


Figure 5.9: Comparison of reconstructed TEC from simulated TEC data with and without DCBs.

### 5.4.2 Horizontal accuracy

A detailed analysis of the effect of receiver coverage on the horizontal accuracy of MIDAS ionospheric reconstructions is shown in this section. This is performed by comparing

reconstructed vTEC results with the reference ionospheric models.

The first analysis illustrates the distribution of absolute vTEC errors across the grid by calculating the vTEC errors relative to the reference ionospheric model. Figure 5.10 shows absolute vTEC errors, limited to 5 TECu to highlight small variations in the errors. Black dots represent the GPS receiver locations. The results from both ionospheric models show the effect of receiver coverage on the quality of the reconstructed data. Areas with few or no receivers (North Asia) show large deviations from the ionospheric model (1-3 TECu), where the algorithm is not able to reconstruct the electron density correctly. Over regions with good coverage such as Europe or North America, where many receivers are available, the errors are in the range of 0-1 TECu. It is worth mentioning that the errors beyond the edges of the grid increase dramatically in all regions. This is due to most of the rays falling out of the grid in those areas, causing a lack of available observations, which is clearly visible in North America.

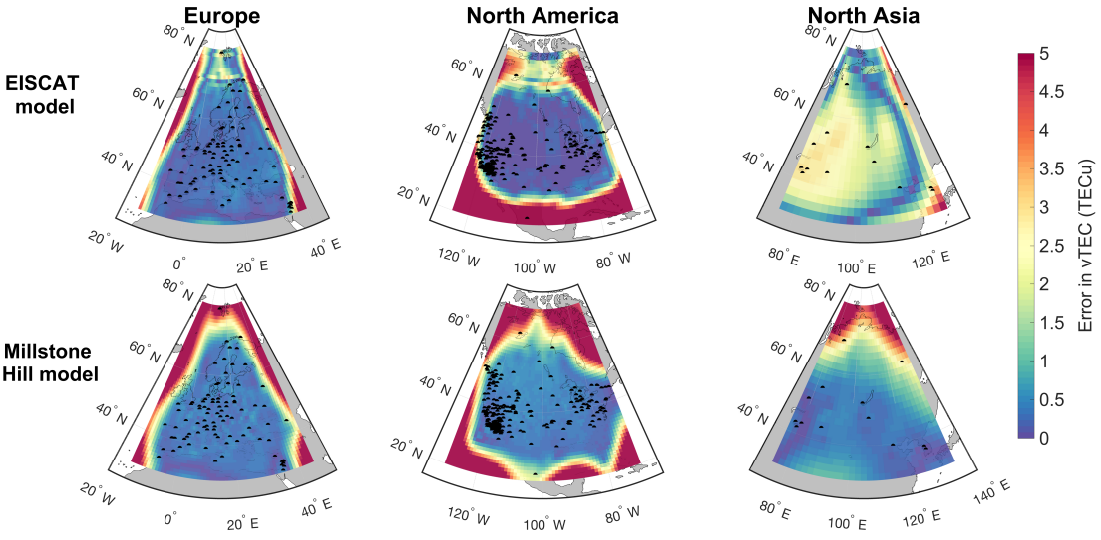


Figure 5.10: Maps of the absolute vTEC errors over Europe, North America and North Asia using EISCAT and Millstone Hill input models.

Figure 5.11 shows relative vTEC errors for the same reconstructions to evaluate the effect of vTEC values of each model on the errors. The colourmap is limited to 10% to highlight small variations at low percentages. Absolute errors over Europe and North America in Figure 5.10 for both models are very similar. Results from the EISCAT model, however, show lower relative errors compared to the Millstone Hill model in Figure 5.11. This is probably because EISCAT model has higher electron density values

than Millstone Hill model. Also noteworthy is that in the region with good receiver coverage the accuracy is 60% to 95% better than in areas with a lower receiver density. This demonstrates that the receiver coverage is an important factor in MIDAS.

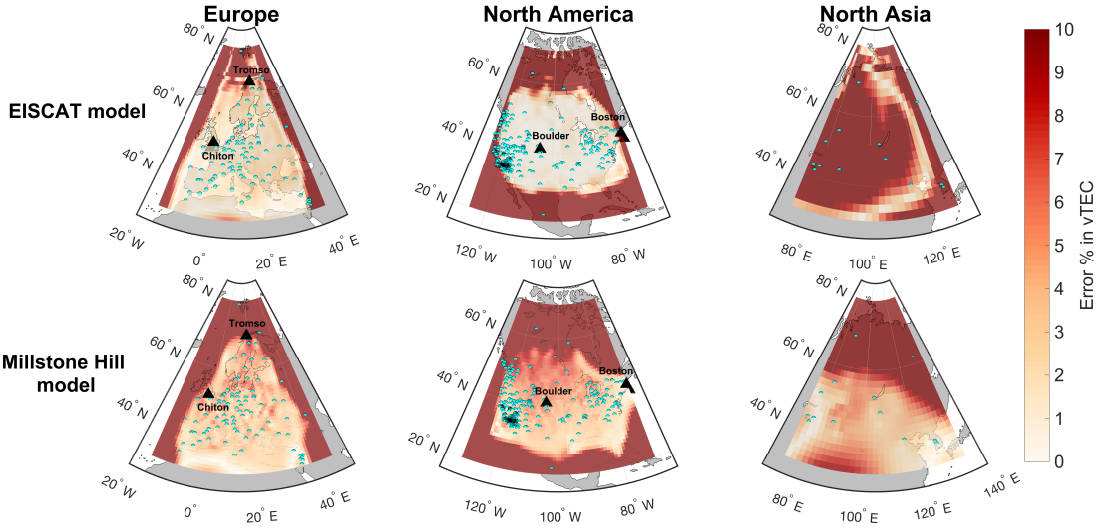


Figure 5.11: Maps of relative vTEC error over Europe, North America and North Asia using EISCAT and Millstone Hill input models. The triangles in the maps correspond to the locations of the ionosondes used to create the reference model (Tromsø and Boston) and the ones used to create the vertical EOFs for MIDAS (Chilton and Boulder).

When comparing the results from Europe and North America with Asia, the effect of the chosen grid resolution can be seen. Overall, if the area of study is sufficiently covered with ground receivers, an accurate representation of the ionospheric total electron content can be obtained. The results over Asia show errors of 1-3 TECu in Figure 5.10 due to the low resolution of the reconstruction. In order to obtain high accuracy results (relative errors below ∼2%), a larger receiver network and a higher resolution reconstruction is needed, as seen in the good coverage region in Europe and North America in Figure 5.11.

### 5.4.3 Vertical accuracy

The accuracy of the vertical electron density distribution of tomographic images is also an important factor for high-precision applications. Therefore, the third goal is to evaluate the vertical accuracy of the MIDAS algorithm. This is done by comparing the vertical electron density distribution of the reconstructions with those of the ionospheric reference models that provide the input to the algorithm. Ionospheric reconstructions

for two regions are investigated to analyse the influence of the type and number of EOFs used to aid MIDAS: Europe with the EISCAT model and North America with the Millstone Hill model. Performance is compared for a single EOF and 2 EOFs, calculated from both original ionosonde profiles as well as topside calibrated ionosonde profiles.

Figure 5.12 presents the reconstructed vertical electron density profiles for the European region with the EISCAT ionosphere model at Tromsø (radar location) and Chilton (ionosonde location) in the upper row. The lower row gives vertical density profiles for the North-American region with the Millstone Hill ionosphere model at Boston (radar location) and Boulder (ionosonde location). These locations are shown in the maps in Figure 5.11. The 'true' vertical electron density profile derived from the reference model at each location is added for comparison.

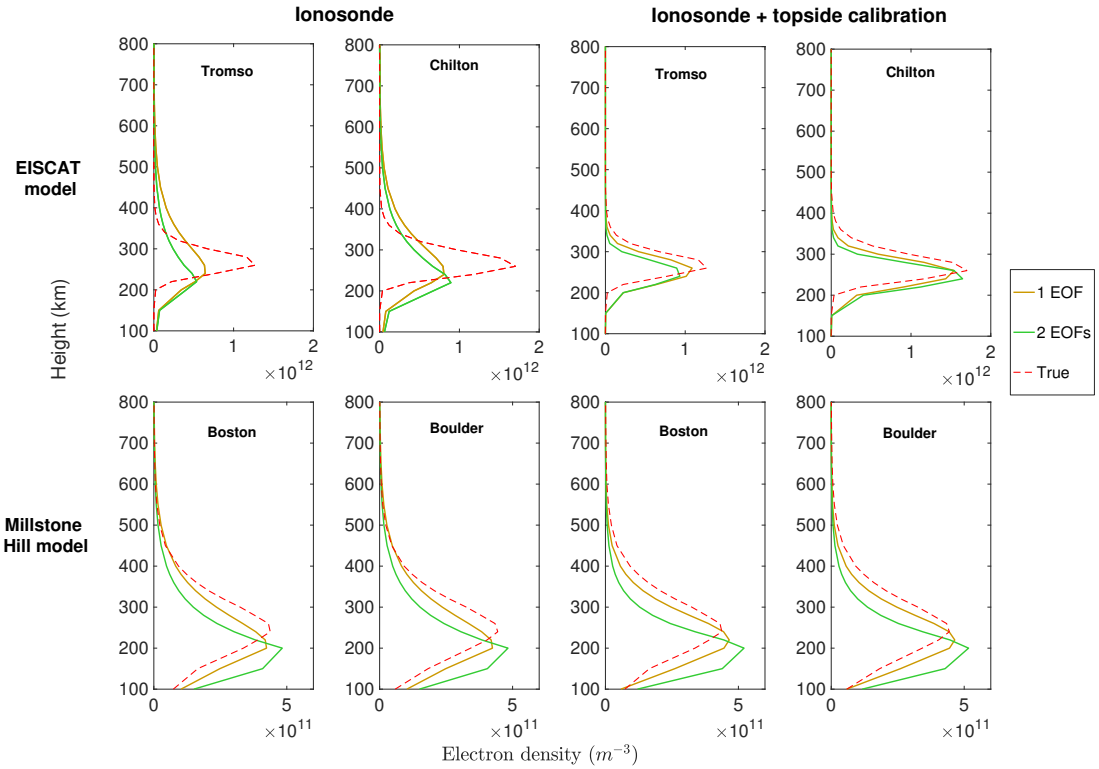


Figure 5.12: Reconstructed vertical electron density profiles at Europe (EISCAT model) and North America (Millstone Hill model) obtained using 1 or 2 EOFs, compared with the true vertical electron density distributions at different locations.

The results in Figure 5.12 shows that the reconstructed ionospheric peak densities are underestimated when using the EISCAT input model and EOFs derived directly

from the Chilton ionosonde data. In contrast, the results using EOFs derived from the topside calibrated ionosonde approach (Section 5.3.2) show closer agreement to the true profile for the majority of the results. An improvement in the thickness of the F region of the profiles can also be seen when using EOFs derived from the calibrated ionosonde data.

The main parameters of the reconstructed ionosphere and their errors at Tromsø, Chilton, Boston and Boulder are summarised in Table 5.2. For both ionospheric models, it can be seen that the results when using only 1 EOF derived from calibrated ionosonde data (the highlighted column in the table) provide the best estimation of the F2 peak electron density.

Analysing the reconstruction of the EISCAT ionospheric model (Table 5.2a and b), it can be seen that by using EOFs derived from calibrated ionosonde data, the errors in the estimations of the peak electron densities have been reduced by $20 - 40\%$ when compared with EOFs from uncalibrated (standard) ionosonde data. The results of the Millstone Hill ionospheric model (Table 5.2c and d), on the other hand, show no major improvement compared to results using original ionosonde data. This is likely because the ionosonde used for the input model (Tromsø) and the ionosonde used for the EOFs (Chilton) are in two different latitudinal regions — high latitude and mid latitude, respectively. This is not the case in the Millstone Hill model, where both ionosondes are in similar latitudes. The improvement seen when using the vTEC topside calibrated ionosonde shows that the influence the topside ionosphere information has on the reconstruction, particularly when the source of the EOFs are in a different region to that of the input model. When considering the impact of the number of EOFs, the errors when using 2 EOFs are larger in comparison with the errors obtained when using 1 EOF only. This is caused by the increase in the number of unknowns when increasing the number of EOFs, which makes the problem more difficult to solve when the data are insufficient.

Given the results in Figure 5.11 and Table 5.2, it can be concluded that the topside calibrated ionosonde method to calculate EOFs improves the overall vertical accuracy of this ionospheric electron density imaging algorithm, even when the location of interest is at a significant distance from the ionosonde that provides information for the EOFs.

Table 5.2: Parameters of the reconstructed ionosphere and their errors at **a)** Tromsø and **b)** Chilton using the EISCAT ionospheric model; and **c)** Boston and **d)** Boulder using the Millstone Hill ionospheric model.

| | **EOFs from ionosonde data** | | | | **EOFs from calibrated ionosonde data** | | | | **Input** |
|---|---|---|---|---|---|---|---|---|---|
| **a) Tromsø** | 1 EOF | Error (%) | 2 EOFs | Error (%) | 1 EOF | Error (%) | 2 EOFs | Error (%) | |
| Peak height (km) | 240 | 20 (7.69%) | 220 | 40 (15.38%) | 260 | 0 (0.0%) | 240 | 20 (7.69%) | 260 |
| Peak density ($\times 10^{11} m^{-3}$) | 6.47 | 6.20 (48.95%) | 6.04 | 6.64 (52.36%) | 10.85 | 1.82 (14.42%) | 9.62 | 3.05 (24.01%) | 12.68 |
| vTEC (TECu) | 11.07 | 1.66 (17.69%) | 7.31 | 2.09 (22.27%) | 9.24 | 0.16 (1.73%) | 7.24 | 2.16 (22.99%) | 9.41 |
| **b) Chilton** | 1 EOF | Error (%) | 2 EOFs | Error (%) | 1 EOF | Error (%) | 2 EOFs | Error (%) | |
| Peak height (km) | 240 | 20 (7.692%) | 220 | 40 (15.384%) | 260 | 0 (0.0%) | 250 | 10 (4.846%) | 260 |
| Peak density ($\times 10^{11} m^{-3}$) | 7.78 | 8.59 (52.47%) | 8.03 | 8.34 (50.94%) | 14.66 | 1.71 (10.47%) | 15.14 | 1.23 (7.53%) | 16.37 |
| vTEC (TECu) | 13.31 | 0.23 (1.78%) | 12.06 | 1.01 (7.74%) | 12.49 | 0.58 (4.49%) | 11.90 | 1.17 (8.99%) | 13.08 |
| **c) Boston** | 1 EOF | Error (%) | 2 EOFs | Error (%) | 1 EOF | Error (%) | 2 EOFs | Error (%) | |
| Peak height (km) | 200 | 40 (16.66%) | 200 | 40 (16.66%) | 220 | 20 (8.33%) | 200 | 40 (16.66%) | 240 |
| Peak density ($\times 10^{11} m^{-3}$) | 4.23 | 0.13 (3.16%) | 4.82 | 0.45 (10.31%) | 4.65 | 0.27 (6.36%) | 5.21 | 0.83 (19.06%) | 4.37 |
| vTEC (TECu) | 8.28 | 0.10 (1.23%) | 7.80 | 0.58 (7.01%) | 8.18 | 0.20 (2.44%) | 7.70 | 0.67 (8.09%) | 8.38 |
| **d) Boulder** | 1 EOF | Error (%) | 2 EOFs | Error (%) | 1 EOF | Error (%) | 2 EOFs | Error (%) | |
| Peak height (km) | 200 | 40 (16.66%) | 200 | 40 (16.66%) | 220 | 20 (8.33%) | 200 | 40 (16.66%) | 240 |
| Peak density ($\times 10^{11} m^{-3}$) | 4.24 | 0.19 (4.48%) | 4.82 | 0.38 (8.65%) | 4.64 | 0.20 (4.57%) | 5.16 | 0.72 (16.25%) | 4.44 |
| vTEC (TECu) | 8.29 | 0.22 (2.68%) | 7.84 | 0.67 (7.92%) | 8.16 | 0.35 (4.19%) | 7.73 | 0.78 (9.19%) | 8.52 |

## 5.5 Conclusions

This study introduced a novel simulation framework in which a realistic reference ionosphere was created based on the combination of ISR/IRI/ionosonde measurement data. Using this method, the accuracy of imaging the ionosphere with MIDAS and GPS signals was evaluated. The results show the importance of the distribution and density of GPS receivers, the selected imaging resolution and the use of a realistic representation of the vertical electron density profile.

From the regions studied, North Asia showed errors in vTEC larger than 10% in the ionospheric reconstructions, caused by the limited resolution due to the small number of receivers distributed over the area. In contrast, in the regions with sufficient receiver coverage (Europe and North America), the errors in vTEC were below 2% for the majority of the area under study.

The Satellite/receiver combined DCBs were estimated and compared to the simulated values. Relative errors $< 2\%$ over Europe were found, which did not increase as the simulated input sTEC increases. In addition, equivalent estimated TEC values from MIDAS reconstructions with and without simulated DCBs in the input measurements were obtained, which therefore demonstrates the robustness of MIDAS against both satellite and receiver DCBs. The potential of this MIDAS to estimate DCBs is therefore demonstrated in this chapter.

The investigations carried out in this chapter also underlined the importance of the data sets and methods used to derive the EOFs. Although the obtained vTEC results were very accurate, the vertical electron density distribution differed from the input models. When using the EISCAT model with original ionosondes to calculate the EOFs, errors over 50% in the peak height and density estimation were observed. However, by using the vTEC topside calibrated ionosonde method, the accuracy of the vertical electron density profile was improved (maximum errors of 14% using 1 EOF), while the absolute vTEC remained as accurate as in previous analysis.

## 5.6 Summary

An evaluation method for ionospheric tomography was presented in this chapter. The main purpose was to create a realistic simulation framework to assess MIDAS. Two electron density representations of the ionosphere were created using data from two-

dimensional electron density distributions from ISRs, vertical electron density profiles from co-located ionosondes, and IRI-2016 model. By integrating through these ionospheric representations, simulated sTEC observations were retrieved.

Satellite and receiver DCB estimation using MIDAS was demonstrated. These biases are of important consideration, as they are related to the satellite to receiver TEC measurements (see Section 3.1.2.1) that are generally used as input to MIDAS. In addition, two ionospheric representations were used as input data in the MIDAS software to test the vertical and horizontal accuracy of the imaging algorithm. The results highlight the influence of the GPS ground receiver coverage, and therefore the data coverage, on the accuracy of the electron density images.

This chapter has proven that one of the most important features for high accuracy ionospheric tomography is the data coverage. Following this line of research, the next chapter investigates the addition of GLONASS and Galileo satellites observations into MIDAS algorithm.

# 6 Multi-constellation ionospheric tomography

## Introduction

The availability of satellites from multiple GNSS constellations has increased the achievable accuracy in precise positioning applications (e.g. Hernández-Pajares et al., 2003; X. Li et al., 2015; Cai et al., 2015; Tegedor et al., 2014)). However, there is still a need to improve the precision of atmospheric and ionospheric corrections to levels required by these applications. The majority of the ionospheric delay, $\simeq$99.9%, can in theory be corrected using dual-frequency ionosphere-free linear combinations (Mannucci et al., 1998), which remove all frequency-dependent effects from the GNSS observables, such as the ionospheric delay. However, this combination, obtained by differencing the time delay of signals of two frequencies, increases the noise in the solution (Teunissen and Montenbruck, 2017) and introduces the need to correct for DCBs (Wilson and Mannucci, 1993; Håkansson et al., 2017). This is because the hardware of both the satellite and receiver introduce a different delay to signals having different carrier frequencies, resulting in a bias in the differenced measurement. Differential multipath from poorly sited antennas can additionally contribute to these biases. DCBs bias sTEC measurements derived from each satellite-receiver pair and the effect is experienced by all GNSS constellations.

Some precise positioning applications rely on externally-provided ionospheric corrections, which generally require ionospheric slant delay corrections that are directly proportional to sTEC. The most common correction sources come from ionospheric tomography images from GPS observations (Hernandez-Pajares et al., 2000; Colombo et al., 2000), Global Ionospheric Maps (GIM) (Banville et al., 2014; X. Li et al., 2013), or ionospheric models (Psychas et al., 2019; Z. Li et al., 2019). It has been demonstrated by previous studies (Juan et al., 1997; Allain and Mitchell, 2009) that three-dimensional ionospheric tomography shows better performance in positioning corrections than two-dimensional 'thin-shell' solutions derived from GIMs or models, as it allows estimation of the electron density along the satellite to receiver path without using a mapping function. The new aspect to this chapter is the use of multiple constellations in tomography and

to investigate the errors through both simulation and experiment.

The use of ionospheric tomography and data assimilation with GPS to study the ionosphere is well established in the research community (e.g. Bernhardt et al., 1998; Materassi and Mitchell, 2005; Saito et al., 2017). Leitinger et al. (1997) first proposed the use of combined GPS and GLONASS data for ionospheric imaging. In recent years, regional and global TEC maps from GPS and GLONASS observations were presented in Kunitsyn et al. (2011), while Yin et al. (2011) used the combination of GPS and GLONASS to create three-dimensional images of the Antarctic ionosphere; where GLONASS was shown to improve the results, in part due to the higher orbital plane used by its satellites. As the European Galileo constellation has not been fully operational for many years yet, not many studies have been conducted to investigate the effect of combining GPS/GLONASS with the Galileo constellation for ionospheric tomography. This chapter evaluates the combination of GPS-GLONASS-Galileo global constellations (hereafter known as Multi) for ionospheric tomography. The aim is to show the potential improvement in horizontal accuracy when imaging the ionospheric electron density with MIDAS.

The chapter is structured as follows. First, an introduction to the method that estimates satellite DCBs is given. This is followed by a simulation to select the optimal horizontal resolution for the ionospheric images, which additionally provides a reference of the achievable accuracy under ideal conditions. Finally, electron density maps and DCBs retrieved using actual data from equatorial (Brazil) and mid-latitude (Europe) regions are presented and discussed.

## 6.1 Satellite DCB estimation

As discussed in Chapter 5, one of the main limiting factors of MIDAS is the limited geometry due to sparse ground-receiver coverage, which can lead to large errors in the electron density estimation (Bruno et al., 2019). This limitation can be addressed in two ways: by increasing the number of ground receivers or the number of satellites from different GNSS constellations used in MIDAS. The impact of different ground-receiver networks was analysed in Chapter 5. The latter technique is addressed in this chapter by combining constellations in MIDAS.

For satellite and receiver DCB estimation, the same approach as that used in Chapter 5 (and described in Section 3.1.2.2) is implemented here, although with an

additional step: The combined DCBs are separated to satellite and receiver DCBs using the method defined in (N. Wang et al., 2016). This method solves the individual satellite and receiver DCBs from the combined DCBs using regularised least squares, where a zero-mean distribution regularisation on all satellite DCBs for each individual constellation is assumed. As this second step is completely independent from ionospheric tomography, this method allows to estimate DCBs from a given constellation even if no observations from that constellation were used to create the ionospheric maps. Therefore, in this work, satellite DCBs from GPS, GLONASS and Galileo constellations are estimated using ionospheric images from both MIDAS-GPS and MIDAS-Multi. An elevation cut-off of 10° is also implemented in this chapter, thereby assuming the average noise ($\epsilon$ in Equation 3.9) to be negligible over each satellite pass.

### 6.1.1 Dataset

Regional ionospheric electron density maps for mid and low latitudes are created in this chapter, both for a simulated scenario (Section 6.2) and with actual observations (Section 6.3). For the mid-latitude analysis (Europe), a total of 99 receivers from the IGS, EUREF and UNAVCO networks are used, all of them providing GPS, GLONASS and Galileo dual-frequency phase and pseudorange observations. For the low-latitude analysis (Brazil), 27 ground receivers from IGS and IBGE networks are used. Figure 6.1 shows the locations of all GNSS receivers used in this chapter.

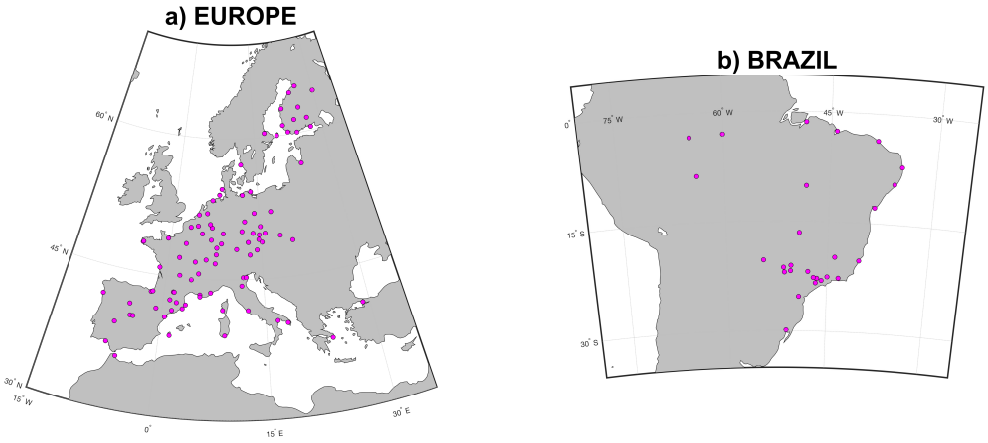


Figure 6.1: Locations of ground GNSS receivers used for inversion in a) Europe and b) Brazil.

The EOFs used to augment the inversions are created from ionosonde observations from Juliusruh (Germany) and Fortaleza (Brazil) to aid the vertical resolution at mid and low latitude images respectively. Ionosonde observations are used as they help estimating the $h_m(F_2)$ for the Chapman profiles. Two EOFs are used in all experiments described in this chapter. These basis functions are incorporated into MIDAS following the theory introduced in Section 4.2.

The region over which an image is analysed is determined based on the availability of observations. Figure 6.2 shows the number of actual TEC observations per vertical column of 1-by-1 degree size over a 2-hour period for the nominal day 18 September 2017. Europe is shown in the top row and Brazil in the bottom row, with the left hand side showing MIDAS-GPS and the right hand side MIDAS-Multi.

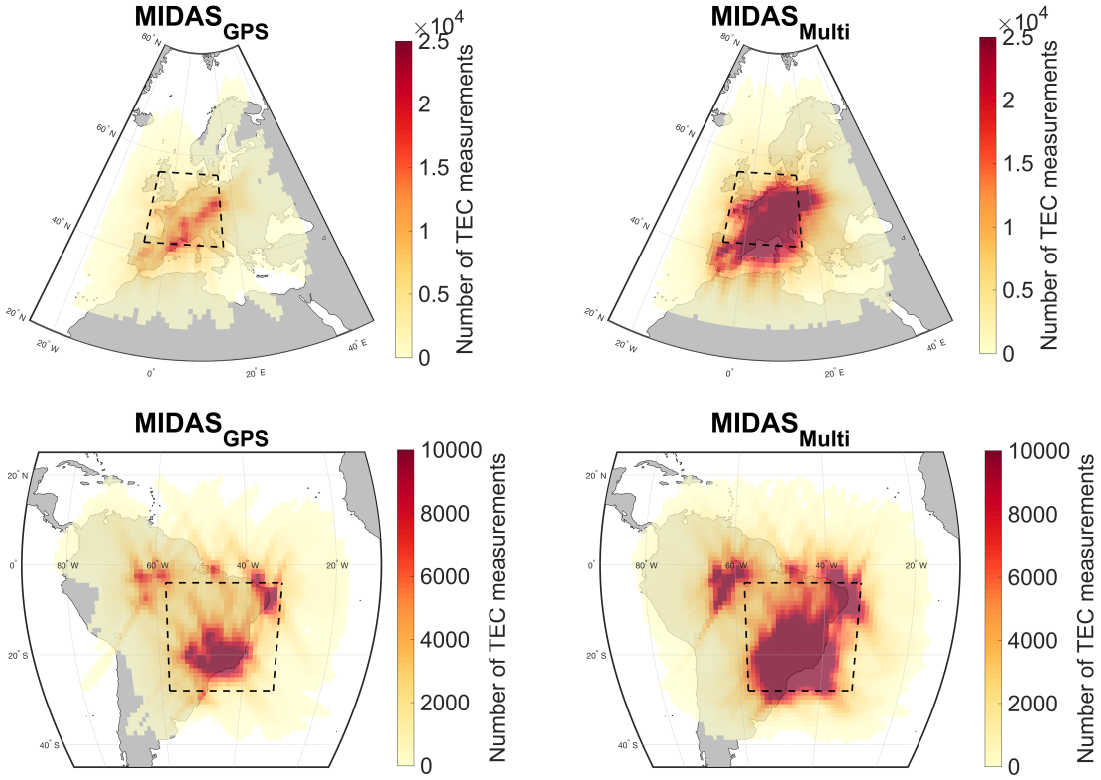


Figure 6.2: Number of TEC measurements used to create a single image in Europe and Brazil from MIDAS-GPS and MIDAS-Multi.

The number of observations decreases dramatically at the edges of the grid where there are less ray-paths. Therefore, only the ionospheric results from the dashed line

areas in Figure 6.2 are analysed in this chapter, unless otherwise stated.

## 6.2 Simulation results

The aim of this research is to evaluate the accuracy and the horizontal resolution improvement that can be achieved when using multiple satellite constellations in ionospheric tomography. Therefore, an end-to-end simulation is performed to determine the achievable accuracy with different three-dimensional grid resolutions that would be suitable for GPS and Multi-constellation tomography. In this stage of the analysis, ionospheric images for 18 September 2017 are generated using different grid resolutions and different combinations of constellations. Simulated GNSS TEC measurements from Europe and Brazil are used as input data for the MIDAS ionospheric tomography algorithm. The TEC is calculated by integrating the electron density along satellite-to-receiver ray paths through a known simulated ionosphere — IRI-2016 (Bilitza et al., 2017). The IRI-2016 model is used in this simulation to provide a reference ionosphere on the same day of the actual observations i.e. on 18 September 2017. Actual receiver (Figure 6.1) and satellite geometries of each constellation are used to obtain the satellite-receiver ray paths for the entire day. To create a more realistic simulation, satellite DCBs, receiver DCBs and random noise are added to each emulated observation. For the satellite DCBs, values from Multi-GNSS EXperiment (MGEX) (Montenbruck et al., 2014) are used, whereas bias values, ranging from 0 to 9.9 and 0 to 2.7 TECu in Europe and Brazil, respectively, are applied as receiver DCBs, with a 0.1 TECu difference between consecutive receivers. Since MIDAS is run in the differential phase mode, these will only affect the final re-estimation of the DCBs. For the noise term, normally distributed random noise ($\mu = 0$ and $\sigma = 5\%$ of the IRI-integrated sTEC) is added to each emulated sTEC. As these noise values are quite large for differential phase noise, the simulation assumes harsh and noisy environments for the receivers. This simulation is therefore considered as a worst-case scenario. Different image resolutions are analysed, namely 5, 4, 3, 2, 1, 0.5, 0.4 and 0.3 degree pixels in latitude-longitude.

The analysis is done by comparing the vTEC and satellite DCBs estimated with MIDAS reconstructions against the IRI reference ionosphere model and reference MGEX DCBs that were used to create the emulated sTEC measurements. The results provide a reference for the error estimates that can be expected under conditions that are represented by the model – i.e. geomagnetically quiet conditions. Figure 6.3 shows the absolute (panels a and c) and relative (panels b and d) vTEC errors for each horizontal grid resolution that was run. The errors are computed by comparing the known IRI

model vTEC with the results from the simulation inversion that was used to generate the electron density maps.

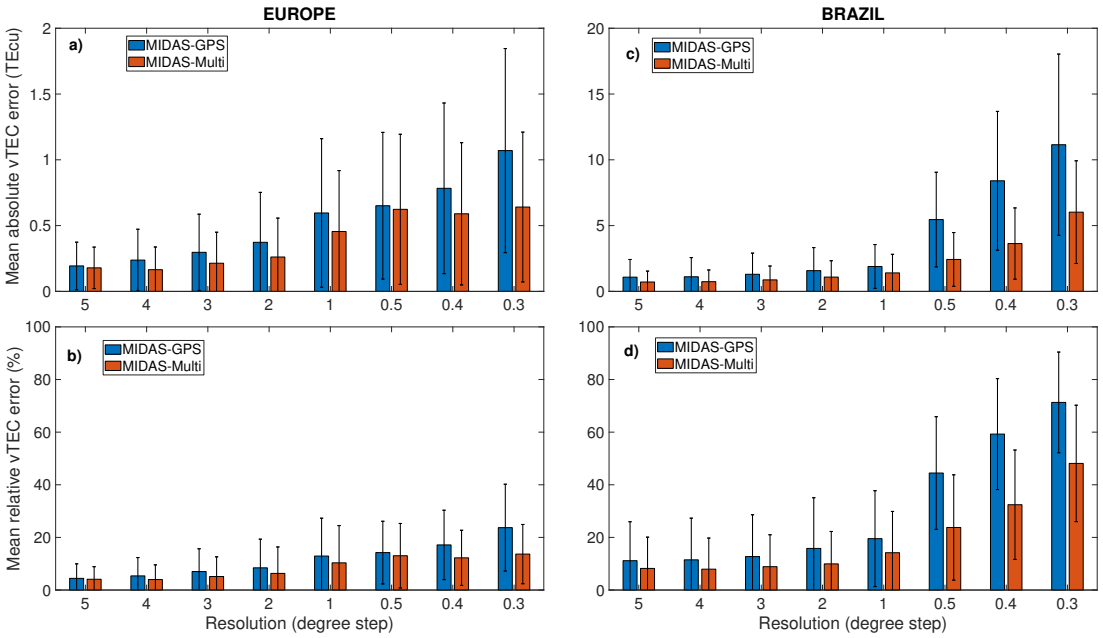


Figure 6.3: Absolute and relative vTEC errors — mean (bars) and standard deviation (black lines) — between IRI and MIDAS-GPS (blue bars) and between IRI and MIDAS-Multi (red bars) images with simulated observations over Europe (panels a-b) and Brazil (panels c-d) for each resolution.

The figures over Europe (panels a-b) and Brazil (panels c-d) show comparable performances for all resolutions down to 1 or 2 degrees, with larger errors for 0.5, 0.4 and 0.3 degree resolutions. Multi constellation tomography reduces the errors compared to GPS-only in all simulations. Noteworthy is that the addition of constellations is more beneficial in Brazil where the receiver network is more sparse, especially at very high resolutions.

Based on the balance between accuracy and resolution, the 2-degree resolution is selected for further investigation,

### 6.2.1 Vertical TEC error distribution

Figures 6.4 and 6.5 show the temporal and spatial vTEC distributions over Europe and Brazil calculated with MIDAS. The mean vTEC results plotted over time for the regions of interest (areas denoted by dashed lines in Figure 6.2) for IRI, MIDAS-GPS

and MIDAS-Multi are presented in Figure 6.4. The vTEC values are averaged for each hourly image to obtain the mean vTEC. In addition, the Root Mean Square Error (RMSE) compared to the reference IRI vTEC is shown in the legend. The values show that there is a definite improvement in the overall error with the multi-constellation results. Considering the mean errors for both MIDAS-GPS and MIDAS-Multi (i.e. the difference between the mean vTEC of each reconstruction and the IRI reference) the values are observed to be below 0.5 TECU for both Europe and Brazil for the majority of the images. It is interesting to note that an increase in the errors by ∼1 TECu over Europe is observed at certain times of day (at 10 UT and 14 UT) with results from MIDAS-GPS. A similar issue is again observed in the Brazil results, with errors ∼ 1-2 TECu at 15 and 23 UT. These errors are reduced with MIDAS-Multi.

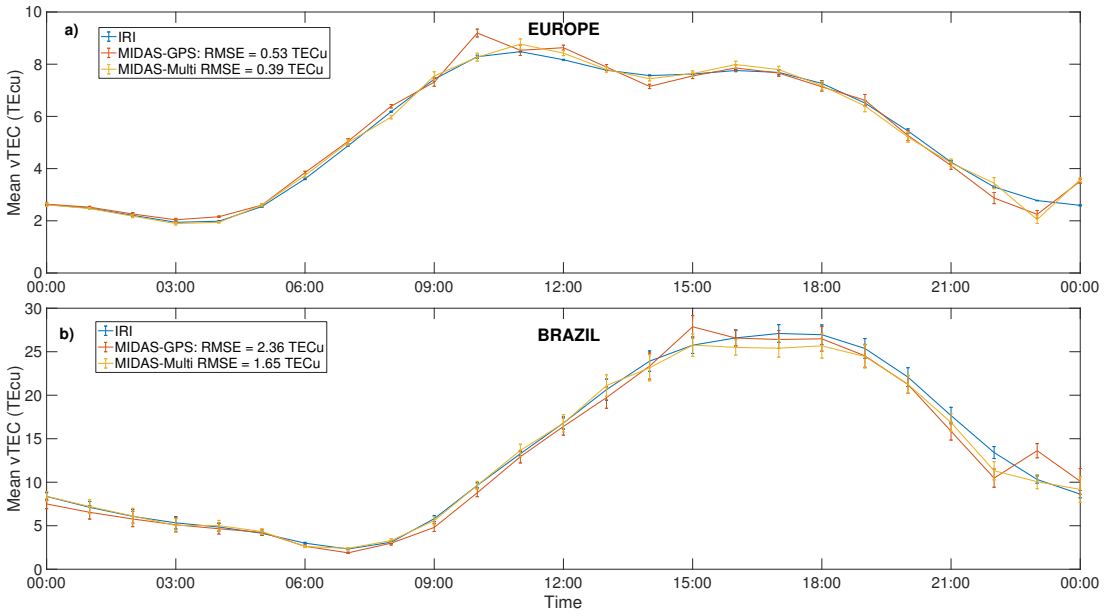


Figure 6.4: Mean vTEC from IRI, MIDAS-GPS and MIDAS-Multi over a) Europe and b) Brazil. Time is in UT hours.

Figure 6.5 shows the vTEC error distribution for each latitude/longitude in Europe and Brazil, where the mean absolute vTEC error value for each latitude/longitude pixel over the entire day is calculated. As mentioned before, larger errors are found at the edges of the grid, as many rays crossing the ionosphere fall out of the area under study. Given the large errors towards the edges of the grids, the region of good data coverage shown by the dashed lines is selected for the analysis for each location, where the errors

are found to be below 0.5 TECu and ∼1.5 TECu in Europe and Brazil, respectively.

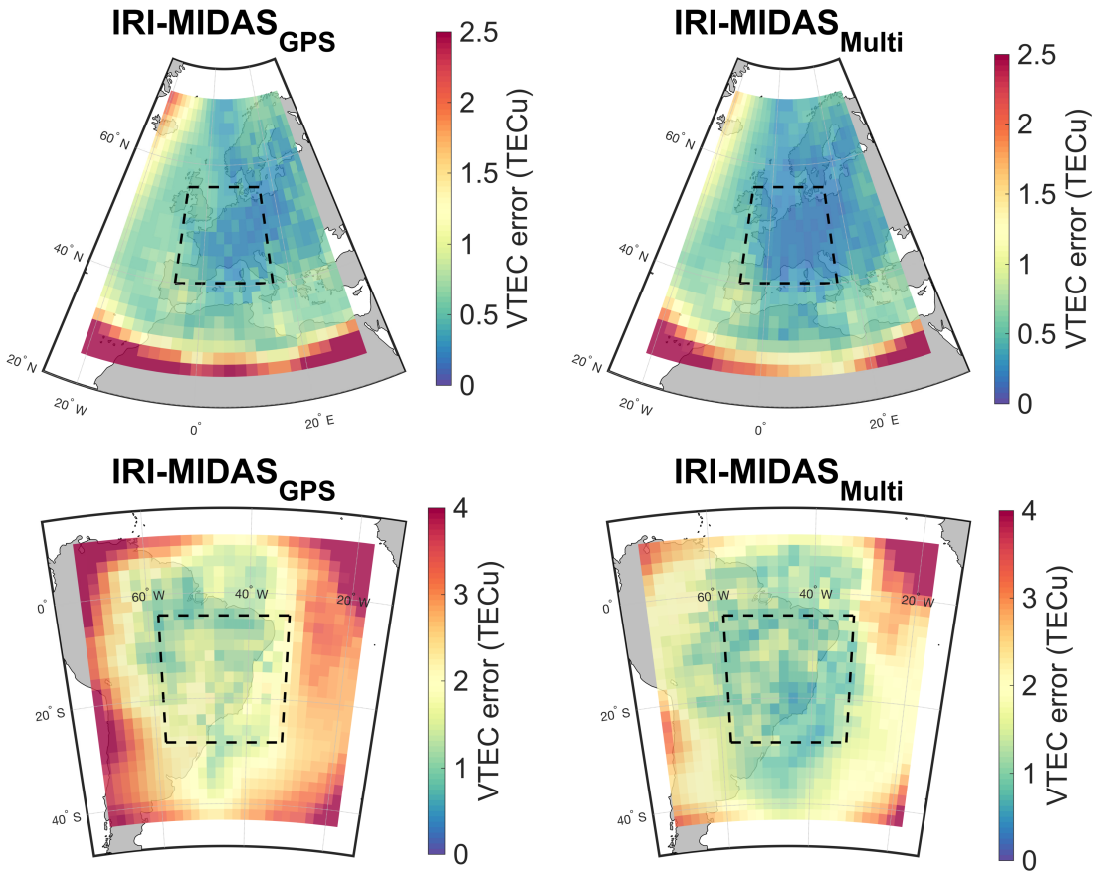


Figure 6.5: Mean absolute vTEC error between IRI and MIDAS-GPS, and IRI and MIDAS-Multi over Europe and Brazil. The dashed lines represent the region of high measurement density.

An improvement in vTEC of ∼ 0.3 TECu and ∼1 TECu is observed with MIDAS-Multi with respect to MIDAS-GPS for Europe and Brazil, respectively.

### 6.2.2 Satellite DCB estimation

The validation of satellite DCBs by comparing the MIDAS-estimated satellite DCBs against the MGEX DCBs from the end-to-end simulations is shown in Figure 6.6. The blue colour represents the GPS, GLONASS and Galileo satellite DCBs calculated from MIDAS-GPS results, while the red colour represents biases from MIDAS-Multi results.

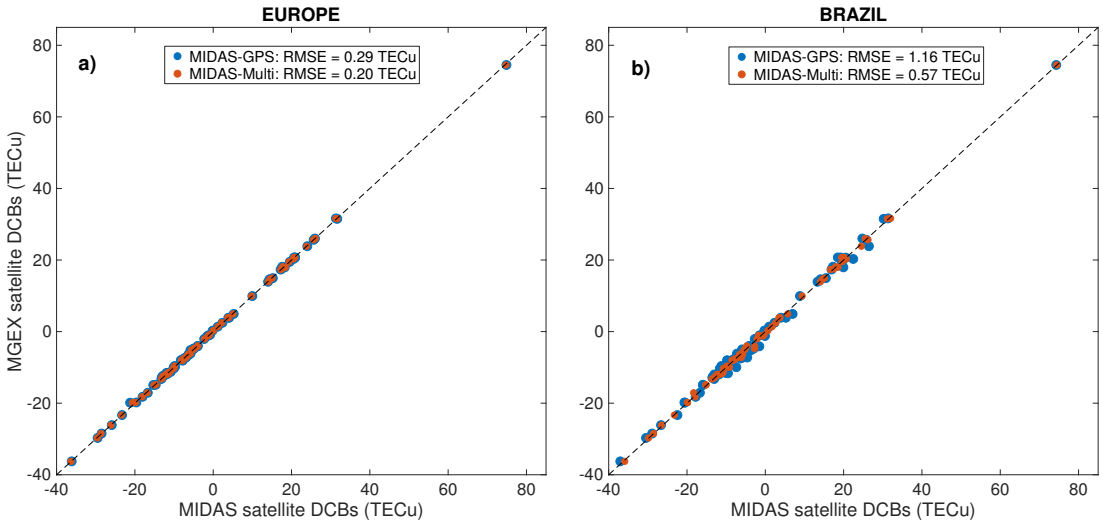


Figure 6.6: MGEX (simulated values) and MIDAS (estimated values) satellite biases across all constellations (TECu). Panel a) show results from Europe and panel b) from Brazil. The RMSE of the satellite bias for both MIDAS-GPS and MIDAS-Multi are given as an inset of the respective panel.

Similar to the vTEC results in previous section, the satellite DCB estimation over Europe shows only a very small improvement between MIDAS-GPS and MIDAS-Multi, with RMSE $< 0.3$ TECu. In contrast, the RMSE over Brazil increases up to 1.16 TECu with MIDAS-GPS, whereas for MIDAS-Multi it increases only up to 0.57 TECu, which represents an improvement of 0.59 TECu. Table 6.1 provides a summary of the RMSE between DCBs from MGEX and DCBs estimated from MIDAS images.

Table 6.1: Summary of RMSE between MGEX and MIDAS with simulated data for all constellations individually. RMSE are given in TECu.

| **Region** | **Images** | **Sat. bias RMSE (MGEX – MIDAS) in TECu** | | |
|---|---|---|---|---|
| | | GPS | GLONASS | Galileo |
| Europe | MIDAS-GPS | 0.22 | 0.22 | 0.45 |
| | MIDAS-Multi | 0.18 | 0.14 | 0.28 |
| Brazil | MIDAS-GPS | 1.13 | 1.19 | 1.18 |
| | MIDAS-Multi | 0.55 | 0.48 | 0.71 |

As can be seen in Table 6.1, MIDAS-Multi provides a small improvement of $0.04-0.17$ TECu in RMSE ($18-37\%$) over Europe. In contrast, Brazil sees a much larger improvement of $0.47-0.71$ TECu in RMSE ($39-59\%$) when using multi-constellation tomography. Larger errors are found over Brazil relative to Europe for all results as less ground receivers are available over the region, which reduces the number of available measurements from each satellite. The multi-constellation observations to some level compensates for the lack of receivers in the region, which is why a significant improvement is observed.

The results shown in Figure 6.4-6.6 and Table 6.1 provide a reference of the achievable accuracy under geomagnetically quiet conditions over Europe and Brazil. Overall, errors below 5% in vTEC and DCB estimation are obtained over Europe and Brazil for MIDAS-Multi.

## 6.3 Experimental results

The receiver network used for the simulation (see Figure 6.1) is also used in the experimental element of this chapter. This section analyses reconstructions of true events created from MIDAS-GPS and MIDAS-Multi for both geomagnetically quiet (13-18 September 2017) and disturbed (07-09 September 2017) periods.

To assess the performance of MIDAS-Multi with actual independent data, the ionospheric electron density maps are compared with vTEC maps (GIMs) from the independent software package MIT Automated Processing of GPS (MAPGPS) (Rideout and Coster, 2006). In addition, the satellite DCBs retrieved from MIDAS are compared with the DCBs from the MGEX. It must be noted that this validation provides a

comparison of the ionospheric results from MIDAS, rather than a complete knowledge of the absolute errors. This is because, the true electron density distribution within the ionosphere is not known to the levels of accuracy being considered in these experimental results. Nevertheless, a consistent approach between the simulation and the experiment is utilised to gain insight into the errors.

### 6.3.1 Vertical TEC errors

This section compares vTEC between MIDAS images and MAPGPS GIMs. Results from MAPGPS are used for this analysis as it provides higher temporal and spatial resolution than any other GIM. The MAPGPS software uses data from more than 2000 globally distributed receivers to produce global TEC maps. For the dates analysed in this thesis, this method uses observations from GPS satellites only. The data is provided in 1-by-1-degree latitude-longitude bins every 5 minutes, over locations where data is available. The maps are made available by the Open Madrigal Initiative. As the GIMs only provide vTEC information, MIDAS images are vertically integrated at each latitude/longitude grid point. A common image resolution is also implemented for both GIMs and MIDAS images where the vTEC values from GIMs are interpolated to match the chosen resolution of the MIDAS images. Figures 6.7 and 6.8 present the comparison of mean and standard deviation of vTEC over time between MAPGPS, MIDAS-GPS and MIDAS-Multi for the geomagnetically quiet period and for the disturbed period, respectively.

The MIDAS-GPS vTEC results given in Figures 6.7 and 6.8 show similar values compared to the MIDAS-Multi images, with differences in the mean vTEC Root Mean Square (RMS) between single and multi-constellation below 0.5 TECu for both quiet (Figure 6.7) and disturbed (Figure 6.8) periods. MIDAS-Multi shows a more stable performance than MIDAS-GPS over Europe, especially on 08 September 2017 (Day Of Year (DOY) 251) when the effect of the geomagnetic storm in the ionosphere was strongest. During the disturbed period, the vTEC results from MIDAS-Multi are in better agreement to MAPGPS, improving results from MIDAS-GPS in $\sim$24% (from 1.85 TECu to 1.41 TECu). On the other hand, the vTEC results from MIDAS-GPS and MIDAS-Multi over Brazil show very similar results regardless of geomagnetic activity, with vTEC RMS differences below 0.4 TECu ($\sim$1%) between them.

Figures 6.9 and 6.10 show the distribution of the differences in mean vTEC between MAPGPS and MIDAS in Europe and Brazil for the geomagnetically quiet (Figure 6.9) and disturbed (Figure 6.10) periods. These maps show not only the highlighted regions

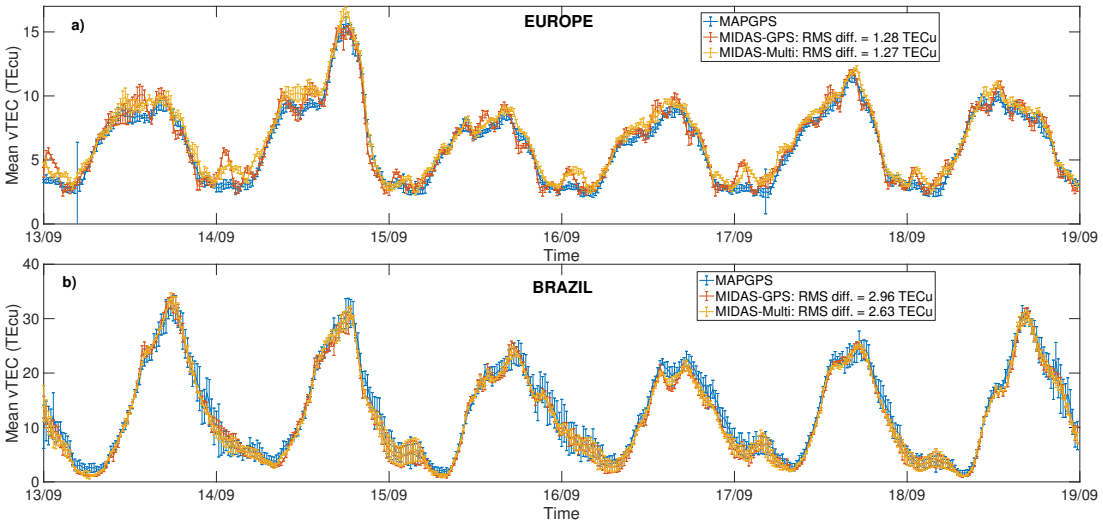


Figure 6.7: Mean (line) and STD (bars) vTEC from MAPGPS, MIDAS-GPS and MIDAS-Multi during the geomagnetically quiet period (13-18 September 2017) over a) Europe and b) Brazil. Time is in UT hours.

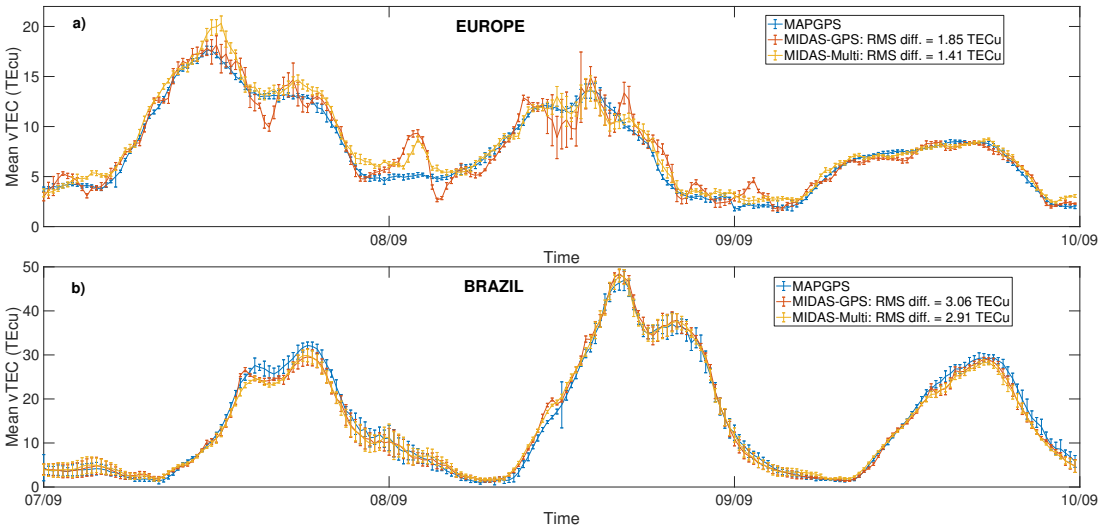


Figure 6.8: Mean (line) and STD (bars) vTEC from MAPGPS, MIDAS-GPS and MIDAS-Multi during the geomagnetically disturbed period (07-09 September 2017) over a) Europe and b) Brazil. Time is in UT hours.

in Figure 6.2, but also the surrounding areas where the grid extends to highlight the larger errors found at the edges of the grid.

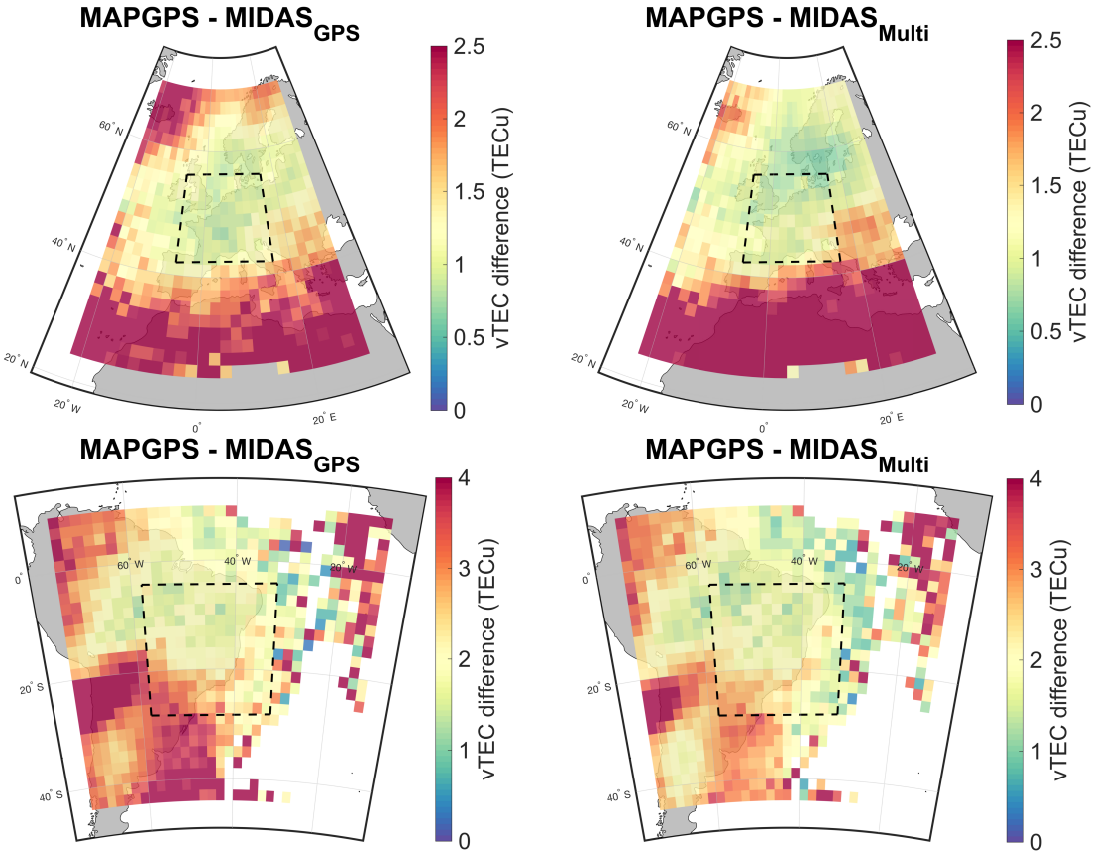


Figure 6.9: Mean absolute vTEC differences between MAPGPS and MIDAS-GPS, and MAPGPS and MIDAS-Multi over Europe and Brazil during the geomagnetically quiet period (13-18 September 2017). The dashed lines represent the region of high measurement density.

An improved agreement between MAPGPS and MIDAS-Multi in electron density estimation, compared to MIDAS-GPS, is observed in these figures. Over Europe, the agreement between MAPGPS and MIDAS vTEC images at high latitudes ($> 60°$) is greatly increased with the addition of GLONASS and Galileo constellations into MIDAS, due to more high-elevation observations provided at higher latitudes by the higher inclination angle (64.8°) of the orbital planes of the satellites in the GLONASS constellation. The improvement is also noticeable over the mainland (highlighted region in Figure 6.2), where the vTEC differences between MAPGPS and MIDAS are reduced to ∼0.5 TECu (quiet period) and ∼1 TECu (disturbed period) when using MIDAS-Multi. Over Brazil, similar vTEC difference distributions are found between MIDAS-GPS and MIDAS-Multi when compared to MAPGPS. The differences are however reduced when using MIDAS-Multi — ∼0.5 TECu smaller than MIDAS-GPS during both quiet and

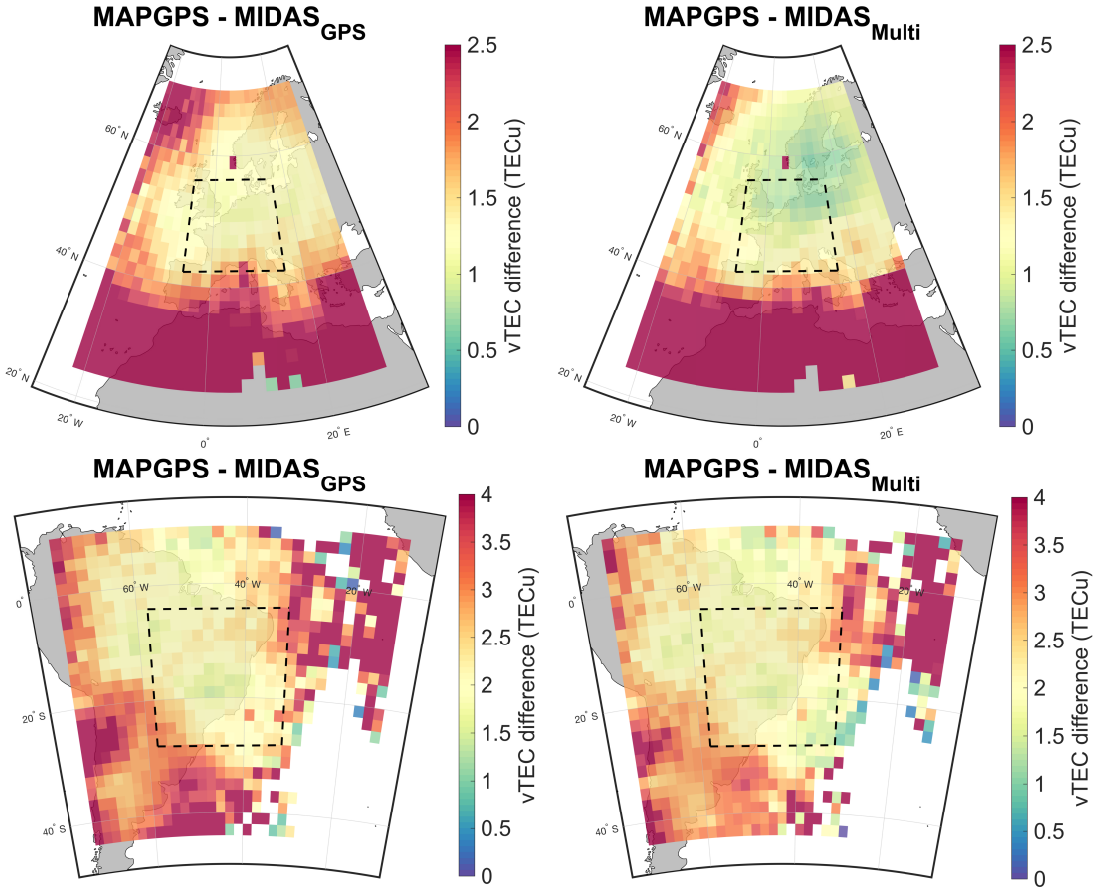


Figure 6.10: Mean absolute vTEC differences between MAPGPS and MIDAS-GPS, and MAPGPS and MIDAS-Multi over Europe and Brazil during the geomagnetically disturbed period (07-09 September 2017). The dashed lines represent the region of high measurement density.

disturbed periods, thereby showing a better estimation of the electron density with MIDAS-Multi relative to MIDAS-GPS for Brazil as well.

### 6.3.2 Satellite DCB estimation

The DCBs retrieved from MIDAS-GPS and MIDAS-Multi are compared to those provided by the MGEX project. Figure 6.11 shows the satellite DCB comparison for the geomagnetically quiet period for Europe and Brazil. The blue colour represents the GPS, GLONASS and Galileo satellite DCBs calculated from MIDAS-GPS, while the red colour represents biases for the same satellites from MIDAS-Multi.

For the geomagnetic quiet period, no significant differences are observed between

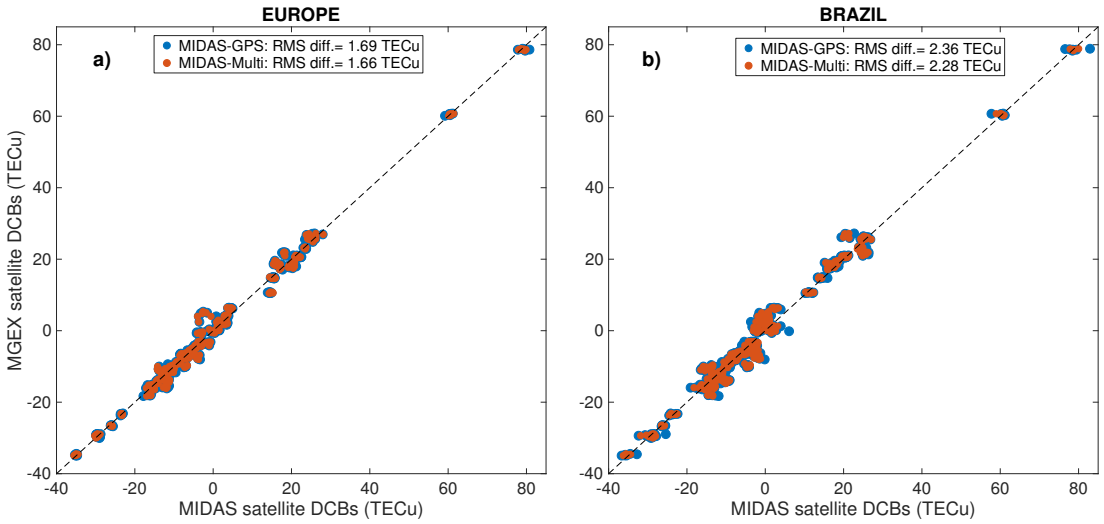


Figure 6.11: MGEX and MIDAS satellite biases (TECu) during the geomagnetically quiet period (13-18 September 2017). Panel a) show results from Europe and panel b) from Brazil. The blue dots represent MIDAS-GPS results, while the red dots represent the MIDAS-Multi results. The RMS difference of the satellite DCBs between MGEX and MIDAS are given as an inset of the respective panel.

DCBs estimated from MIDAS-GPS and MIDAS-Multi. All RMS differences between MGEX and MIDAS are below 1.7 TECu over Europe and 2.4 TECu over Brazil.

For the geomagnetically disturbed period, the bias differences are shown independently for each day so as to isolate the effect of the geomagnetic storm that occurred on DOY 251 (08 September 2017). This comparison is presented in Figure 6.12.

The results show no great impact when using GLONASS and Galileo observations alongside GPS in the European region (panels a)-c)), with a maximum improvement of 0.09 TECu in satellite DCB RMS difference between MIDAS-GPS and MIDAS-Multi. However, a larger improvement is observed when combining different constellations in Brazil (panels d)-f)), where a decrease of 0.24 TECu in DCB RMS difference is observed on DOY 251. A summary of the RMS differences between DCBs from MGEX and DCBs estimated from MIDAS images is given in Table 6.2, which can be compared to the simulation results given in Table 6.1. Satellite DCBs for all constellations, from both MIDAS-GPS and MIDAS-Multi images, are evaluated during both quiet and disturbed periods. For the disturbed period, only DOY 251 is considered since the geomagnetic conditions of DOY 250 and 252 did not have a significant impact on the DCB estimation process.

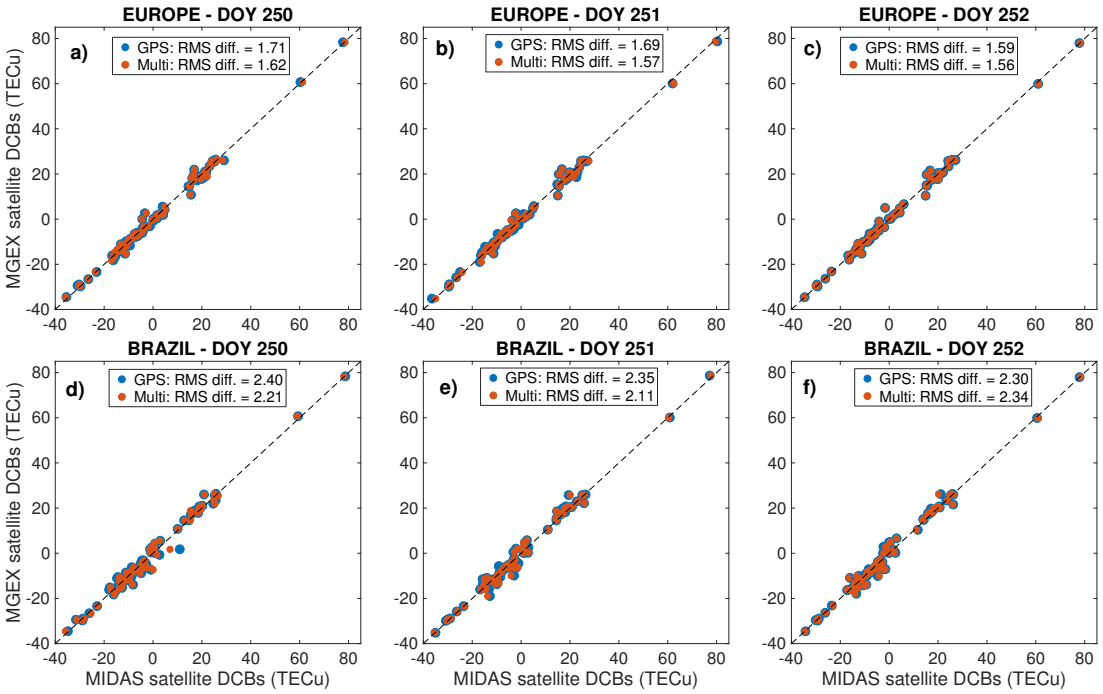


Figure 6.12: MGEX and MIDAS satellite biases (TECu) during the geomagnetically disturbed period (07-09 September 2017). Panels a)-c) show results from Europe and panel d)-f) from Brazil. The blue dots represent MIDAS-GPS results, while the red dots represent the MIDAS-Multi results. The RMS difference of the satellite DCBs between MGEX and MIDAS are given as an inset of the respective panel.

The results show improvements in the RMS difference up to 0.9 TECu between DCBs estimated from single and multi-constellation MIDAS. DCBs for all constellations estimated from MIDAS-Multi are in closer agreement with MGEX than DCBs estimated with MIDAS-GPS only. For both single and multi-constellation images, RMS differences in the biases of $\sim$3 TECu higher over Brazil and $\sim$2 TECu higher over Europe are found in the estimation of GLONASS satellite DCBs with respect to GPS and Galileo satellites, for both quiet and disturbed periods. This is addressed in the following section (Section 6.4).

Table 6.2: Summary of RMS differences between MGEX and MIDAS with actual data for all constellations. RMS differences are given in TECu.

| **Region** | **Period** | **Images** | **Sat. bias RMS difference (MGEX – MIDAS) in TECu** | | |
|---|---|---|---|---|---|
| | | | GPS | GLONASS | Galileo |
| Europe | Quiet period | MIDAS-GPS | 0.87 | 2.60 | 0.28 |
| | | MIDAS-Multi | 0.78 | 2.60 | 0.20 |
| | Disturbed period | MIDAS-GPS | 0.91 | 2.72 | 1.00 |
| | | MIDAS-Multi | 0.85 | 2.62 | 0.82 |
| Brazil | Quiet period | MIDAS-GPS | 0.86 | 3.74 | 0.46 |
| | | MIDAS-Multi | 0.81 | 3.74 | 0.34 |
| | Disturbed period | MIDAS-GPS | 1.13 | 3.77 | 1.58 |
| | | MIDAS-Multi | 1.03 | 3.58 | 0.79 |

## 6.4 Discussion and conclusions

This chapter analyses the potential use of multi-constellation tomography to estimate the ionospheric electron density. A simulated scenario is used to assess the trade-off between accuracy and resolution for single and multi-constellation tomography. Following the results from the simulation, three-dimensional electron density images are created at 2-degree resolution from actual observations to evaluate the achievable accuracy in estimating TEC with GNSS ionospheric tomography.

The simulation provides an estimate of the errors expected under geomagnetically quiet conditions over Europe and Brazil. When evaluating the vTEC over the highlighted region in Figure 6.2, the simulation shows the potential of MIDAS for accurately imaging the ionosphere. For Europe, the mean absolute error (RMSE) with MIDAS-GPS was 0.37 (0.53) TECu, and 0.26 (0.39) TECu with MIDAS-Multi. For Brazil, the mean absolute error (RMSE) with MIDAS-GPS was 1.57 (2.36) TECu, and 1.08 (1.65) TECu with MIDAS-Multi. The simulation therefore indicates that there is an improvement in the estimation of the vTEC over both Europe and Brazil when using the MIDAS-Multi. The mean absolute errors from MIDAS-Multi over Europe account for $\simeq$4 cm delay in L1, and therefore has the potential to be used as ionospheric delay corrections for precise applications (such as PPP) where ionospheric corrections with maximum absolute errors below $\sim$5 cm are generally required (Psychas et al., 2019). Over Brazil, however, the

vTEC mean absolute errors from MIDAS-Multi increases up to 1.57 TECu (∼24 cm), which does not meet the requirements of 5 cm. The implication of this is that the more complex ionospheric dynamics related to the equatorial anomaly and a sparse ground receiver network in the region result in insufficient observations for high accuracy imaging, even with a greater number of satellites contributing to the observations.

The simulation also demonstrates an improvement in the estimate of the satellite DCBs over Brazil when using the MIDAS-Multi, which improves the precision by ∼50% compared to MIDAS-GPS. Over Europe, however, the improvement evaluated by the mean difference and RMSE between single and multi-constellation is smaller (∼0.09 TECu or ∼30%). It can therefore be concluded that MIDAS-Multi gives a better or similar overall performance than MIDAS-GPS in estimating DCBs, depending on data coverage, and has potential to replace MIDAS-GPS in future applications.

The experimental analysis during geomagnetically quiet conditions compares the vTEC maps from MIDAS against vTEC maps from MAPGPS. For Europe, the mean absolute (RMS) difference between MIDAS-GPS and MAPGPS is 1.01 (1.28) TECu, and 1.01 (1.27) TECu between MIDAS-Multi and MAPGPS. For Brazil, the mean absolute (RMS) difference between MIDAS-GPS and MAPGPS is 2.34 (2.96) TECu, and 2.10 (2.63) TECu between MIDAS-Multi and MAPGPS. When comparing the results over Europe from actual observations with the results obtained from the simulated scenario, vTEC RMS differences $> 3 - 5$ times larger are observed in the experimental analysis. Over Brazil, however, the vTEC RMS differences between MIDAS and MAPGPS are only ∼2 times larger than what was expected from the simulation. The vTEC results during the quiet period (∼16 cm in Europe and ∼37 cm in Brazil) do not meet the 5 cm requirement for precise ionospheric corrections. Nevertheless, as mentioned before, the comparison against MAPGPS does not provide absolute errors, as none of the methods are capable of providing actual ionospheric electron density values to within a known accuracy.

During periods of high geomagnetic activity, small irregularities created in the ionospheric plasma make high accuracy imaging of the ionospheric electron density more challenging. In addition, the use of 2 EOFs only could increase the difficulty as all small perturbations in the vertical electron density distribution may be smoothed. For Europe, the mean (RMS) difference between MIDAS-GPS and MAPGPS is 1.28 (1.85) TECu, and 1.02 (1.41) TECu between MIDAS-Multi and MAPGPS. For Brazil, the mean (RMS) difference between MIDAS-GPS and MAPGPS is 2.18 (3.06) TECu,

and 2.10 (2.91) TECu between MIDAS-Multi and MAPGPS. The results during the disturbed period (∼17 cm in Europe and ∼34 cm in Brazil) do not meet the requirement for precise ionospheric corrections. Nevertheless, all differences between quiet and disturbed period are also below 1 TECu, showing that MIDAS performs consistently well regardless of geomagnetic activity.

The differences between satellite DCBs estimated using MIDAS and MGEX with experimental data show a zero-mean distribution for every constellation. The RMS differences for the experimental analysis are provided earlier in Table 6.2. The differences between satellite DCBs estimated with MIDAS and MGEX are also observed to be larger for the real events than with the simulation. It must be noted that Galileo satellite DCBs estimated during the disturbed period experience larger RMS differences compared to the DCBs from GPS and GLONASS satellites — ∼1 and ∼0.75 TECu for MIDAS-GPS and MIDAS-Multi, respectively, compared with ∼0.35 TECu and ∼0.15 TECu for GPS and GLONASS satellites. The larger values (of RMS differences) for Galileo is the result of two of its satellites having very large DCBs (∼60 and ∼80 TECu — the largest in the data), which leads to any small variations on these satellites causing a dramatic increase in the errors. The RMS differences percentage of these satellites only increase around $2 - 3\%$.

An interesting observation in the DCB estimation results for GLONASS is the significantly smaller values (∼4-10 times smaller) obtained for the simulated scenario, than for the real events. These differences may be caused by a known problem related to estimating the inter-frequency biases of GLONASS receivers. Wanninger (2012) shows different inter-frequency biases depending on the frequency of the signal, which in GLONASS is different for each satellite, and the type of receiver, which has a direct impact on the estimation of the satellites DCBs as observations from all receivers are equally processed in MIDAS. Figure 6.13 shows the differences in DCB estimation between MIDAS and MGEX for GLONASS satellites, both in TECu (a) and nanoseconds (b), and sorted by frequency channel. The relationship between the channel and the DCB difference is clearly visible, with larger differences at channels further from the central frequency. This distribution is aligned with the results found by other authors using the MGEX ground receiver network (N. Wang et al., 2016; N. Wang et al., 2020).

Overall, the differences between MIDAS-GPS and MIDAS-Multi show that small improvements can be achieved with multi-constellation tomography at 2-degree resolution. Differences below 0.3 TECu ($< 1\%$) are seen between MIDAS-GPS and MIDAS-Multi

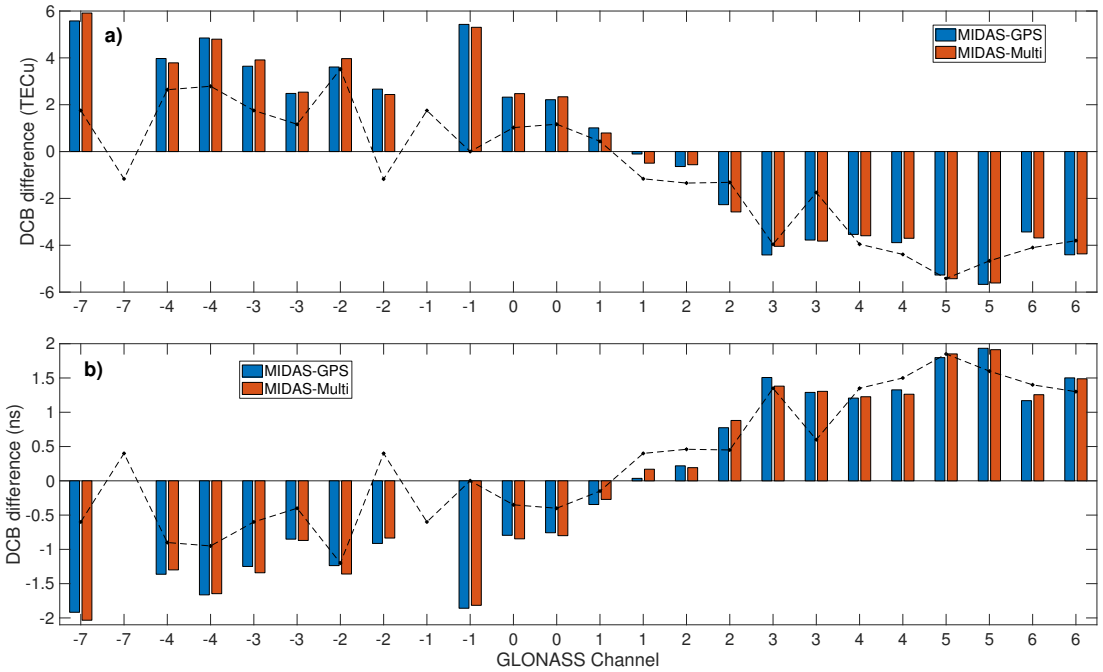


Figure 6.13: Differences between GLONASS satellite DCBs from MGEX and GLONASS satellite DCBs estimated with MIDAS (blue from MIDAS-GPS and red from MIDAS-Multi), both in TECu (a) and nanoseconds (b). The DCBs are sorted by channel. The black dashed line represents the results from N. Wang et al. (2016).

in vTEC RMS during the quiet period, which increase to a maximum of 1 TECu (2%) in RMS during disturbed periods. The differences in DCB estimation between single and multi-constellation tomography are also found to be very small for images over Europe and Brazil, with DCB differences $< 0.54$ TECu. Although these results indicate the benefit of including multiple constellations for tomography-based satellite DCB estimation is small, it is worth mentioning the values are also dependent on the image resolution. The simulation process, presented in Section 6.2, showed that larger improvements can be achieved at very high resolutions (0.3 degrees). However, the simulation study is limited, as IRI provides a smooth representation of the ionospheric electron density, and structures like Travelling Ionospheric Disturbances (TIDs) and scintillation-inducing density gradients are not modelled, which can cause larger errors in the electron density estimation in MIDAS and losses of lock on the signals at the receiver.

## 6.5 Summary

This chapter presented an approach to use multiple GNSS constellations to estimate the three-dimensional ionospheric electron density. The work carried out has demonstrated the potential benefit of multi-constellation tomography within the MIDAS algorithms.

The tomographic reconstructions of electron density using single and multi-constellation GNSS data were compared with vTEC images retrieved from the Open Madrigal Initiative, calculated using the MAPGPS software from MIT. The results from MIDAS-Multi images show a small improvement compared to MIDAS-GPS. This shows that there is a quantifiable advantage, even if small, in using the multiple constellations for ionospheric imaging using tomography.

Satellite and receiver DCBs were also independently estimated from the ionospheric images, assuming a zero mean, with daily bias values validated against DCBs provided by MGEX. During the geomagnetically quiet period, only small differences are observed between MIDAS-GPS and MIDAS-Multi DCBs estimations. However, during the disturbed period, larger differences are observed when estimating DCBs from MIDAS-GPS when compared to MIDAS-Multi.

The results during the quiet period are also validated in a simulated scenario. Overall, differences in vTEC are observed over Europe between results from the simulation and the actual data, with values below 1 and 0.5 TECu in RMSE for MIDAS-GPS and MIDAS-Multi, respectively. The results from Europe are well within the 5 cm requirement for ionospheric precise corrections in precise positioning application. Over Brazil, the differences are observed to be $\sim$2 TECu and $\sim$1 TECu for single and multi-constellation images respectively.

It must be noted, however, that the results presented in this chapter do not provide an actual ground-truth validation for the experimental part of the results. This is addressed in the next chapter where MIDAS-Multi is validated in the positioning domain.

# 7 Ionospheric tomography corrections for single-frequency positioning

## Introduction

The excess delay caused by the ionospheric electron density can be corrected using the dual-frequency ionosphere-free linear combination. However, this technique is not valid in single-frequency GNSS receivers. With these receivers, additional information of the actual ionospheric electron density is required to estimate the excess signal delay introduced by the ionosphere. The most common approach used by single frequency receivers to correct for ionospheric delay is the use of empirical models.

The aim of this chapter is to test the achievable accuracy of ionospheric tomography using multiple GNSS constellations, which has been proven as a valid alternative to GPS tomography in Chapter 6. The true electron density distribution within the ionosphere is unknown. The position of the receiver, however, is known at the cm-level, and the navigation accuracy can therefore be used as ground-truth for validation. Different approaches are used to calculate the unknown ionospheric delay on single frequency signals: (1) no corrections, (2) Multi-GNSS tomography, (3) GIMs from the IGS and (4) dual-frequency positioning. The latter serves as a reference that gives the best achievable position solution in terms of ionospheric corrections.

## 7.1 Receiver position estimation

This chapter analyses positioning results from GNSS ground receivers throughout the year 2019. This year is selected because of the availability of multi-constellation GNSS receivers. Ionospheric electron density maps are created using Multi-GNSS MIDAS using RINEXv3 files from globally distributed multi-constellation GNSS receivers from the MGEX project (Montenbruck et al., 2017). These receivers provide observations every 30 seconds from GPS, GLONASS and Galileo constellations simultaneously. In addition to the electron density maps, satellite DCBs are also estimated. Figure 7.1

shows the location of the receivers used to create MIDAS maps, and the ones used for validation.

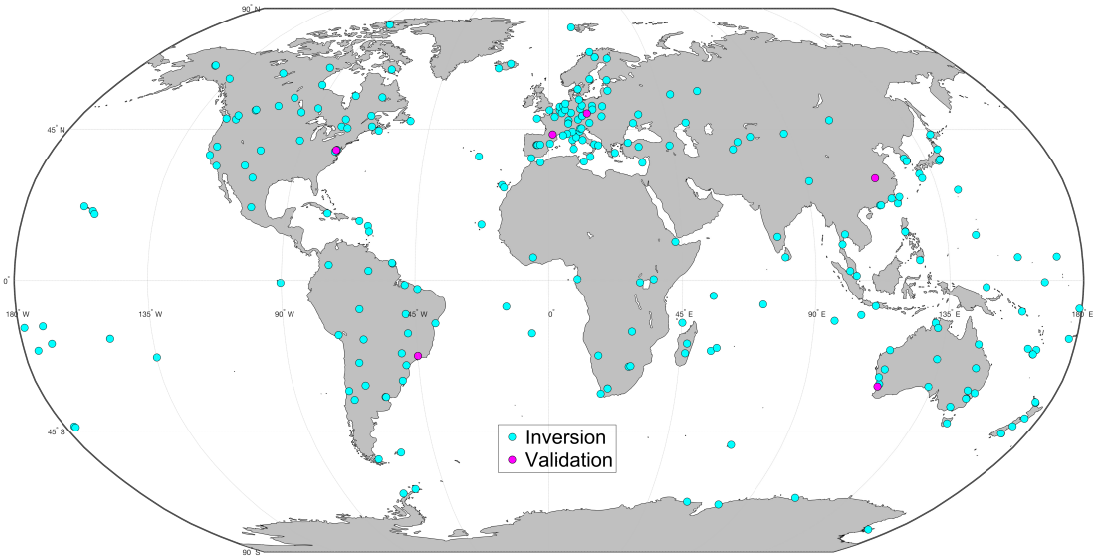


Figure 7.1: Locations of ground GNSS receivers used for inversion and validation.

Orbital information for all constellations is provided by MGEX, which gives satellite positions every 15 minutes. A 9th order Lagrange interpolation is therefore used to retrieve satellite positions and velocities every 30 seconds. The maps created from MIDAS are run for a spatial resolution of 2.5 degrees in latitude, 5 degrees in longitude and 100 km in height, from 0 to 1200 km above the Earth's surface. The temporal resolution of the maps is selected to be 1 hour.

### 7.1.1 Positioning method

The single-frequency positioning method described in Section 3.1.3 is used in this chapter to estimate the position of the receivers. As described in Section 3.1.2, the ionospheric delay can be corrected through multiple means such as GIMs, ionospheric models and ionospheric tomography. In this chapter, the accuracy of the ionospheric delay corrections from four different sources are assessed. First, the position estimated with no ionospheric corrections (hereafter Uncorrected) is used as reference to observe the improvement of the other correction methods. The second approach is the use ionospheric tomography with MIDAS for ionospheric correction. As many researchers have shown the improvement of using 2D and 3D GIMs or models over the Klobuchar or NeQuick broadcast models (Allain and Mitchell, 2009; Feltens et al., 2011; N. Wang et al., 2018; Su et al., 2019), GIMs from CODE are then considered to calculate ionospheric correc-

tions (hereafter CODE). Finally, the dual-frequency combination is used to calculate the position (hereafter Dual). This combination removes the first order ionospheric delay, although the process introduces noise and increases multipath errors in the final solution.

In the case of the Uncorrected and Dual approaches, no additional ionospheric corrections are required. In the case of MIDAS, the sTEC is retrieved by integrating the satellite-to-receiver raypaths through each three-dimensional electron density image. Hourly MIDAS images are interpolated in time to match the GNSS receiver cadence (30 seconds) and therefore provide standalone solutions every epoch. In contrast, the GIMs from CODE provide two-dimensional electron density maps only. Therefore, to retrieve the sTEC from the GIMs, the mapping and interpolation method described in Schaer et al. (1998) is performed. As introduced earlier, satellite DCBs (for MIDAS and CODE cases only) are used to calculate the TGD, and hence correct the satellite clock errors.

## 7.2 Experimental results

This section presents a comparison of ionospheric products between MIDAS and CODE, as well as positioning accuracy results from all four ionospheric correction sources. Six receivers from different regions around the Earth (see Figure 7.1) are used for the validation of the results.

### 7.2.1 Ionospheric comparison

A comparison between ionospheric electron density and satellite DCBs from MIDAS and CODE is provided in this section. VTEC differences between maps from the two approaches for every electron density map (1 every hour) are calculated for the entire year, and the RMS for each latitude-longitude voxel is performed. Figure 7.2 shows the geographical distribution of the RMS vTEC differences between MIDAS and CODE maps for 2019.

The figure shows the largest differences between MIDAS and CODE over the oceans, where few receivers are available. Over the mainland at low latitude, where some validation receivers are located, the RMS difference is below 4 TECu, which corresponds to ∼60 cm in L1. At mid latitude, however, the differences are below 2 TECu.

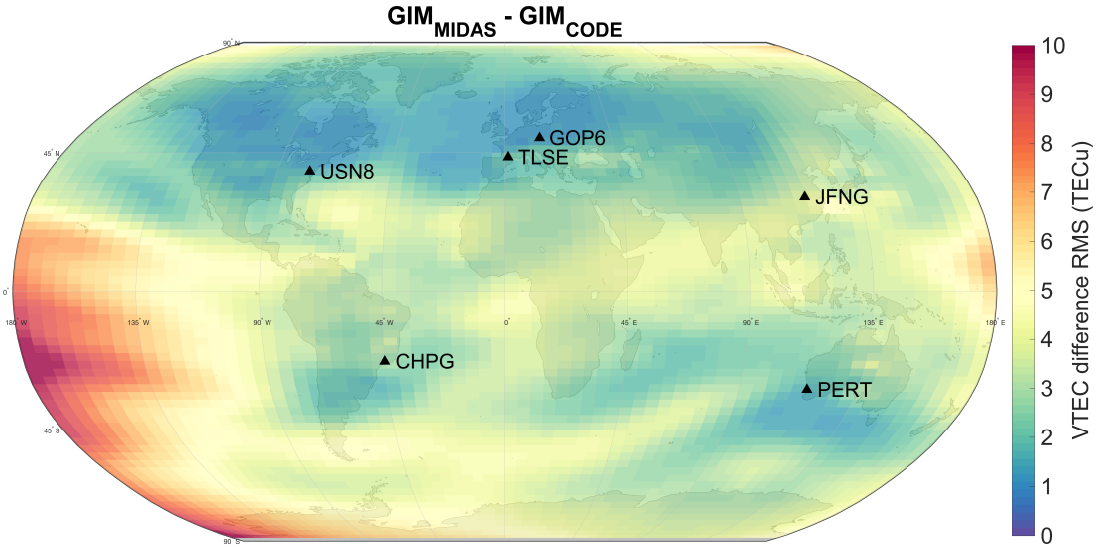


Figure 7.2: Map of the RMS of the vTEC differences between MIDAS and CODE maps from 2019.

Figure 7.3 shows the estimated satellite DCB comparison between MIDAS and CODE. RMS differences for each GPS satellite for the entire year are calculated from daily satellite DCBs.

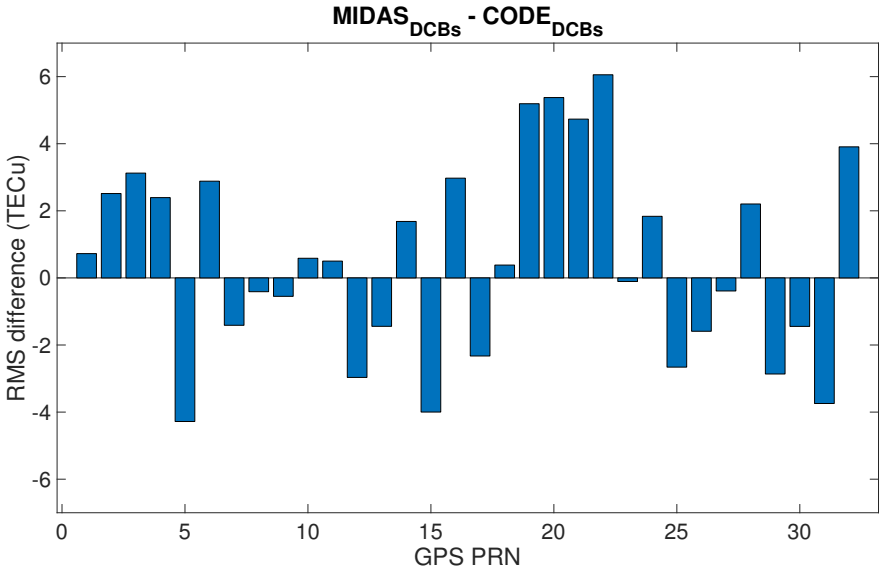


Figure 7.3: Differences in RMS between MIDAS and CODE daily satellite DCBs for 2019.

68% of the satellites (22 out of 32) have differences below 3 TECu, while differences between $4.5-6$ TECu are found for PRNs 19-22. These differences have a direct impact on the MIDAS and CODE ionosphere-corrected position estimation.

### 7.2.2 Positioning validation

Data from six ground receivers are used to carry out the position validation following ionospheric corrections based on the four different methods. Figures 7.4 and 7.5 show the diurnal variation of horizontal and vertical position errors, respectively, for results from PERT (Australia), GOP6 (Europe) and CHPG (South America). Positions are calculated every epoch (30 s) for the entire year of 2019. The yearly average for each epoch is then retrieved, thus providing the diurnal variation of position errors. The RMS Error (RMSE) for the whole year for each ionospheric correction method is provided as an inset on each figure.

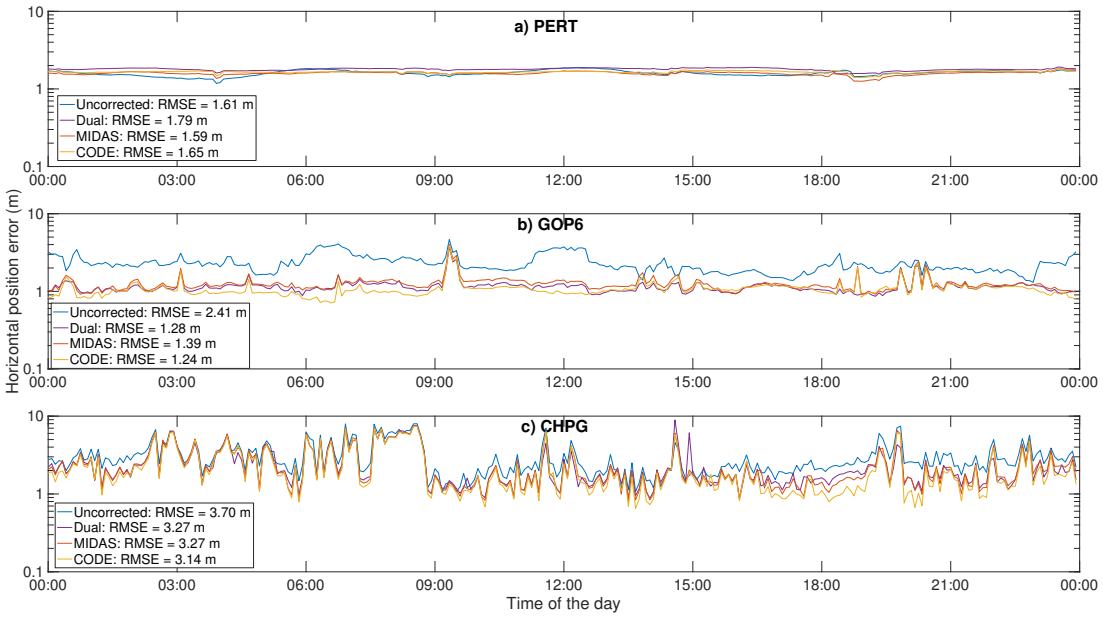


Figure 7.4: Diurnal variation of horizontal errors in the positioning estimation of a) PERT, b) GOP6 and c) CHPG with ionospheric delay uncorrected (blue), estimated from MIDAS (red), from CODE (yellow) and position estimated from dual-frequency observations (purple).

The results show that PERT and GOP6 experience RMSEs below 2 and 4 metres, respectively, for all ionospheric correction sources (MIDAS, CODE and Dual). Larger errors are found in CHPG, especially during local post-sunset (0-9 h UTC) when the

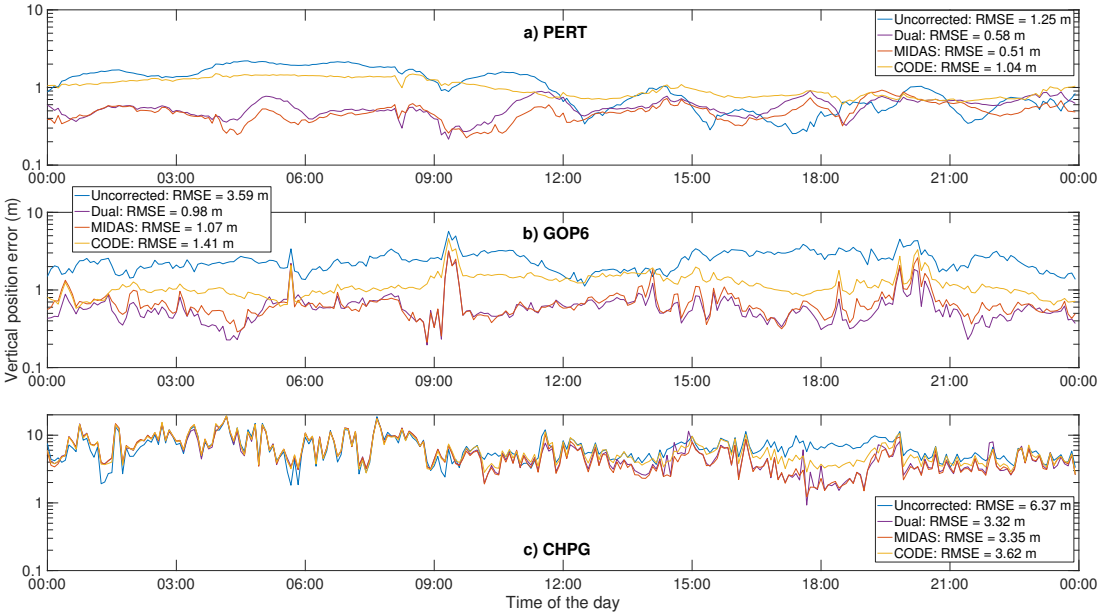


Figure 7.5: Diurnal variation of absolute vertical errors in the positioning estimation of a) PERT, b) GOP6 and c) CHPG with ionospheric delay uncorrected (blue), estimated from MIDAS (red), from CODE (yellow) and position estimated from dual-frequency observations (purple).

effect of scintillation in the ionosphere is strongest (Spogli et al., 2013). The diurnal variation of the ionospheric electron density is negligible in the horizontal errors given in Figure 7.4, which is in contrast to the vertical errors in Figure 7.5, where this variability is clearly visible. Larger differences between CODE and MIDAS/Dual are also observed during local day-time in the vertical component — 0-9 h UTC in PERT, 9-18 h UTC in GOP6 and 15-21 h UTC in CHPG. Corrections from MIDAS and Dual improve the results from CODE in ∼0.5 metres. It is worth noticing that the performance of dual-frequency positioning does not always improve MIDAS positioning results. This is likely because the combination of signals from two frequencies increases the noise level of the pseudorange, and the estimated position can therefore be less precise.

Figures 7.4 and 7.5 showed that the ionospheric delay corrections impact mostly the vertical component of the estimated position. Therefore, Figure 7.6 presents the variation of the vertical component of the estimated position errors throughout the year 2019. The figure shows the daily mean errors calculated from the results from each ionospheric correction method.

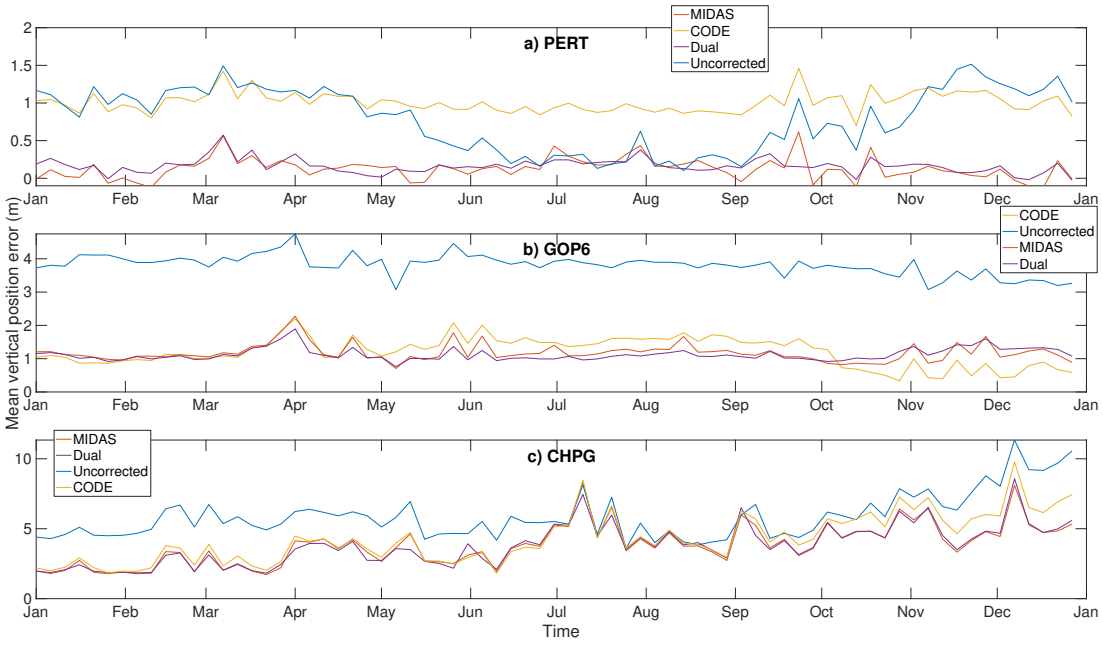


Figure 7.6: Vertical errors in the positioning estimation of a) PERT, b) GOP6 and c) CHPG with ionospheric delay uncorrected (blue), estimated from MIDAS (red), from CODE (yellow) and position estimated from dual-frequency observations (purple) for the entire 2019.

For the PERT receiver, an increase in the vertical error is observed during the local summer (Dec-Apr) relative to the rest of the year, when no ionospheric corrections (Uncorrected) are used in the position solution. This is likely related to the increase in solar radiation over the summer, when longer daylight periods are generally experienced. A similar increase is also observed in CHPG with the uncorrected position estimation over local Spring (Oct-Dec), which may also be related to the longer daylight hours. No noteworthy variations are observed in 2019 at GOP6. Table 7.1 summarises the horizontal and vertical components of the position errors for all validation receivers.

Table 7.1: Summary of position estimation results in metres. The percentage improvement for each ionospheric correction method compared to Uncorrected is given in brackets.

| **Receiver** | **Vertical position RMSE** | | | | **Horizontal position RMSE** | | | |
|---|---|---|---|---|---|---|---|---|
| | Uncor. | MIDAS | CODE | Dual | Uncor. | MIDAS | CODE | Dual |
| PERT | 1.25 | 0.51 (60%) | 1.04 (17%) | 0.58 (54%) | 1.61 | 1.59 (2%) | 1.65 | 1.79 |
| GOP6 | 3.59 | 1.07 (70%) | 1.41 (61%) | 0.98 (73%) | 2.41 | 1.39 (43%) | 1.24 (49%)) | 1.28 (47%) |
| TLSE | 3.08 | 1.19 (62%) | 1.07 (66%) | 1.23 (61%) | 2.41 | 1.36 (44%) | 1.16 (52%) | 1.47 (40%) |
| USN8 | 3.67 | 2.26 (39%) | 2.14 (42%) | 2.29 (38%) | 2.31 | 2.13 (8%) | 2.04 (12%) | 2.19 (6%) |
| JFNG | 4.11 | 2.20 (47%) | 2.40 (42%) | 2.45 (41%) | 1.58 | 1.18 (26%) | 1.08 (32%) | 1.21 (24%) |
| CHPG | 6.37 | 3.35 (48%) | 3.62 (44%) | 3.32 (48%) | 3.70 | 3.27 (12%) | 3.14 (16%) | 3.27 (12%) |

From Table 7.1, ionospheric corrections from all of the methods are observed to improve the accuracy of the vertical component of the estimated position in comparison to the uncorrected. MIDAS shows the best performance of the three ionospheric correction methods and is also comparable to dual frequency position estimations. Considering the dual-frequency approach, the effect of the increase in the noise level in the position estimation is visible in the table. For horizontal errors, ionospheric corrections from MIDAS and CODE provide larger position estimation correction percentages for all receivers than Dual.

## 7.3 Conclusions

This chapter showed the accuracy of the ionospheric four-dimensional maps and satellite DCBs estimated from MIDAS-Multi. In addition, the potential use of MIDAS-Multi for providing ionospheric corrections to support single-frequency positioning estimation was introduced. The chapter showed that ionospheric corrections from MIDAS can compensate for the ionospheric delay at an equivalent level to that provided by dual-frequency positioning, and can sometimes provide a better positioning estimation.

VTEC maps and satellite DCB estimations from MIDAS and CODE were compared in this chapter. Global electron density maps for the entire 2019 were created, and the RMS difference for each latitude-longitude voxel was calculated. Differences between MIDAS and CODE below 2 TECu (∼30 cm) at mid latitude and below 4 TECu (∼60 cm) at low latitude were obtained. The differences in DCB estimation were larger, with errors larger than 3 TECu for ∼30% of the satellites. These results suggest that the differences between MIDAS and CODE in satellite DCB estimation can have a larger

influence in position estimation than the influence of the differences in ionospheric delay estimation.

The positions estimated with corrections from MIDAS and Dual were in very close agreement, with a maximum difference in RMSE of 0.25 metres in the vertical component of the position (JFNG receiver). Dual frequency positioning requires the combination of observation from two frequencies, which increases the noise of the measurements and hampers the receiver position estimation. This was reflected in the performance of Dual for several validation receivers, as the estimated position was sometimes worse than the position estimated with single-frequency observations corrected with either MIDAS or CODE.

The ionospheric corrections from CODE were especially efficient in reducing the horizontal error in the position estimation, with improvements in RMSE between $4-8\%$ compared to MIDAS and between $4-12\%$ compared to Dual. This was likely due to a higher accuracy in satellite DCB estimation by CODE. Further research is however required to confirm this hypothesis. The vertical error is improved in 2 receivers by 0.12 m in RMSE compared to the errors obtained using corrections from MIDAS. MIDAS, on the other hand, improves the vertical accuracy of the estimated position in 4 receivers by $5-32\%$ compared to corrections from CODE. These differences were within the range of $2-4\%$ TECu differences observed in the vTEC comparisons.

These results provide a benchmark under quiet geomagnetic conditions and during solar minimum. As the errors using corrections from MIDAS are in the same range as the errors from dual-frequency positioning, the majority of the ionospheric delay is assumed to be corrected with MIDAS. This therefore applies to solar maximum, where the majority of ionospheric delay errors would also be corrected and similar positioning results would be obtained.

## 7.4 Summary

Single-frequency positioning for six globally distributed receivers for the entire year of 2019 was performed in this chapter. Four ionospheric delay and satellite DCB correction methods — Uncorrected, MIDAS, CODE and Dual — were applied, and the accuracy in the receiver position estimation was compared. Actual data from globally distributed 290 multi-GNSS receivers were used in MIDAS to create four-dimensional electron density images of the ionosphere. Slant TEC values for each of the validation receivers (not

assimilated to get the solution) were then integrated though these maps. In addition, satellite DCBs were calculated from combined (satellite + receiver) DCBs. GIMs from CODE were also used as an ionospheric correction source. These files provide daily satellite DCBs and two-dimensional ionospheric maps, which are used to calculate the sTEC for each receiver. Finally, dual-frequency positioning was performed.

The positioning estimations from three ionospheric correction methods (plus dual-frequency positioning) were compared. The ionospheric delay affects mostly the vertical component of the position estimation. Ionospheric corrections from MIDAS can improve the vertical accuracy of the position estimation between $8 - 63\%$ in RMSE compared to the uncorrected solutions.

This chapter has therefore demonstrated the accuracy of the ionospheric electron density maps calculated with MIDAS-Multi and their potential use as a source of ionospheric correction for globally distributed GNSS-receiver positioning. The computational effort of such technique is however larger, and its use is therefore subject to the application.

# 8 Conclusions

The study, implementation and validation of a multi-constellation ionospheric tomography method has been explored in this thesis. The use of the GPS constellation to image the ionospheric electron density has already been well studied and documented. Extending this technique to multiple constellations, however, has not yet been addressed, as satellites from different constellations were not available until recently. This thesis therefore explores the potential use of observations from GLONASS and Galileo constellations in addition to GPS in an ionospheric tomography algorithm called MIDAS. The work carried out and the collected results are summarised in this chapter. Further work to improve the multi-constellation tomography imaging technique is also discussed.

MIDAS is an ionospheric tomography algorithm. The techniques involves the use of sTEC line-integral measurements (see Chapter 3) from satellites orbiting the Earth to receivers on the ground, where these observations are inverted to retrieve three-dimensional electron density reconstructions. MIDAS and ionospheric tomography are described in Chapter 4. The first objective of this thesis was to validate an assess the current capabilities and limitations of MIDAS. A simulation framework was developed and the vertical and horizontal accuracy of MIDAS was assessed over different locations with differing ground receiver networks. This analysis is documented in Chapter 5. The results show the potential of MIDAS when sufficient observations are gathered, with errors below 0.2 TECu in regions with a high density of ground receivers. Over regions with sparse receiver coverage, however, the errors can increase up to 5 TECu and higher. These results demonstrate that coverage and geometry of observations are the main limiting factors for accurate imaging of the ionospheric electron density with MIDAS.

To address this issue, a multi-constellation (GPS-GLONASS-Galileo) version of MIDAS (MIDAS-Multi) was developed. The addition of extra satellites increases the density of sTEC observations and improves their geometry, without increasing the number of ground receivers. In addition to the electron density images, MIDAS-Multi is now also capable of calculating satellite DCBs independently for every constellation, an addition introduced in this thesis. The new version of MIDAS was tested and validated against MIDAS with observations from GPS only, both in a simulated scenario and with experimental data. Europe (mid-latitude) and Brazil (low-latitude) were selected to validate the methods, as both regions have good multi-constellation receiver networks.

The method and the collected results are discussed in Chapter 6. In addition to vTEC, satellite and receiver DCBs were independently estimated for the first time using MIDAS. The IRI-2016 model was used as a-priori known ionosphere in the simulated scenario. Ionospheric products from MGEX (satellite DCBs) and MIT (GIMs) were used as external validation sources when using actual observations to image the ionospheric electron density. VTEC results from the simulated scenario show that MIDAS-Multi has better accuracy relative to MIDAS-GPS imaging, especially at resolutions $> 0.5$ degree-step in latitude/longitude. MIDAS-Multi reduced errors in vTEC and in satellite DCB estimation by $10 - 25\%$ and $1 - 7\%$, respectively. The vTEC results from actual data confirmed the simulation results, where MIDAS-Multi improved between $1 - 12\%$ and $1 - 24\%$ the vTEC results from MIDAS-GPS during geomagnetically quiet and disturbed periods, respectively. The accuracy of satellite DCBs estimated with MIDAS improved by $5 - 10\%$ relative to MIDAS-GPS when using MIDAS-Multi.

Although an improvement with MIDAS-Multi relative to MIDAS-GPS has been demonstrated in simulated and experimental scenarios, none of the validation methods in Chapter 6 provide an actual ground-truth validation because the true electron density distribution within the ionosphere is unknown. The position of the receiver, however, is known at the cm-level, and the navigation accuracy can therefore be used as ground-truth for validation. This approach was used to additionally validate MIDAS-Multi for the positioning domain in this thesis (Chapter 7). Single-frequency pseudorange positioning was performed with three types of ionospheric corrections: Uncorrected, corrections from MIDAS and corrections from GIMs (from CODE). In addition, dual-frequency positioning was used as a benchmark, which removes the error introduced by the ionospheric electron density; although it has the negative effect of increasing the noise of the measurements that can hamper the receiver position estimation. The method to calculate the receiver position and the results obtained are discussed in Chapter 7, where the errors in the position estimation from the four ionospheric correction methods (Uncorrected, MIDAS, GIM and dual-frequency) are compared. Ionospheric corrections from MIDAS was found to improve the vertical accuracy of the position estimation between $8 - 63\%$ in RMSE compared to the uncorrected solutions. When comparing the positioning performance between using corrections from MIDAS and dual-frequency positioning, the estimated positions are in very close agreement, with a maximum difference in RMSE of 0.25 metres in the vertical component of the position. These results demonstrate the practical application of MIDAS as an ionospheric correction source for single-frequency positioning.

In summary, the key results of the research are:

- The accuracy and capabilities of MIDAS have been demonstrated through a simulation framework. The geometry limitation, due to poor data coverage, was investigated and quantified.
- MIDAS was extended to include multiple GNSS constellations, thus creating the MIDAS-Multi version. This version addresses the geometry limitation by adding extra satellites rather than investing in large ground-receiver networks. In addition, a method to estimate satellite DCBs independently from satellite/receiver combined DCBs was developed for MIDAS.
- The potential use of MIDAS to aid GNSS positioning methods (in particular, in single precise positioning) was demonstrated, achieving accuracies comparable to dual-frequency positioning.

In terms of future experiments, the work of this thesis can be potentially extended with further studies:

The addition of BeiDou GNSS constellation is one factor that can further improve the performance of MIDAS-Multi. This will help increase the available data for each MIDAS image, thereby reducing the geometry limitation of the method. Another important study would be analysing the large GLONASS DCB differences observed in Chapter 6. In addition, the potential use of MIDAS-Multi for precise positioning applications has to be further investigated. The positioning method used as validation in this thesis was able to achieve sub-meter accuracies. Precise positioning methods, however, are capable of achieving sub-centimetre level accuracies. The use of ionospheric corrections from MIDAS in such applications therefore needs to be further investigated. Finally, the growing global availability and the low cost of smart devices makes them an ideal tool for ionospheric tomography. The potential of smartphones for sensing the ionospheric electron density has already been validated in Bruno et al. (2020), indicating that ionospheric tomography based on smart devices may be achieved in the near future.

The research carried out in this thesis has demonstrated the potential use of MIDAS for estimating either global or regional three-dimensional ionospheric electron density distributions. The addition of multiple constellations into the software has increased the accuracy and resolution capabilities of MIDAS. By solving satellite DCBs independently, the ability of MIDAS to provide ionospheric corrections to support GNSS positioning methods has been demonstrated.

# References


Allain, D. J. and C. N. Mitchell (2009). "Ionospheric delay corrections for single-frequency GPS receivers over Europe using tomographic mapping". In: *GPS Solutions* 13.2, pp. 141–151. DOI: 10.1007/s10291-008-0107-y.

— (2010). "Comparison of 4D tomographic mapping versus thin-shell approximation for ionospheric delay corrections for single-frequency GPS receivers over North America". In: *GPS Solutions* 14.3, pp. 279–291. DOI: 10.1007/s10291-009-0153-0.

Andreeva, E. S., V. E. Kunitsyn, and E. D. Tereshchenko (1992). "Phase Difference Radio Tomography of the Ionosphere". In: *Geomagnetism and Aeronomy/Geomagnetizm i Aeronomiia* 32, pp. 104–110.

Appleton, E. V. (1924). "Geophysical influences on the transmission of wireless waves". In: *Proceedings of the Physical Society of London* 37.1, pp. 16D–22D. DOI: 10.1088/1478-7814/37/1/312.

Appleton, E. V. and M. A. F. Barnett (1925). "On Some Direct Evidence for Downward Atmospheric Reflection of Electric Rays". In: *Proceedings of the Royal Society A: Mathematical, Physical and Engineering Sciences* 109.752, pp. 621–641. DOI: 10.1098/rspa.1925.0149.

Ashby, N. (1995). "Relativistic effects in the global positioning system". In: *Journal of systems engineering and electronics* 6.4, pp. 199–237.

Austen, J. R., S. J. Franke, and C. H. Liu (1988). "Ionospheric imaging using computerized tomography". In: *Radio Science* 23.3, pp. 299–307. DOI: 10.1029/RS023i003p00299.

Austen, J. R., S. J. Franke, C. H. Liu, and K. C. Yeh (1986). "Application of computerized tomography tecniques to ionospheric research". In: *International Beacon Satellite Symposium on Radio Beacon Contribution to the Study of Ionization and Dynamics of the Ionosphere and to Corrections to Geodesy and Technical Workshop*. Ed. by A. Tauriainen, pp. 25–35.

Banville, S., P. Collins, W. Zhang, and R. B. Langley (2014). "Global and regional ionospheric corrections for faster PPP convergence". In: *Navigation, Journal of the Institute of Navigation* 61.2, pp. 115–124. DOI: 10.1002/navi.57.

Barclay, L. W. (2003). *Propagation of radiowaves*. Electromagnetic Waves. Institution of Electrical Engineers.

Benedicto, J., S. Dinwiddy, G. Gatti, R. Lucas, and M. Lugert (2000). "GALILEO: Satellite system design". In: *European Space Agency*. Citeseer.

Bernhardt, P. A., R. P. McCoy, K. F. Dymond, J. M. Picone, R. R. Meier, F. Kamalabadi, D. M. Cotton, S. Charkrabarti, T. A. Cook, J. S. Vickers, A. W. Stephan, L. Kersley, S. E. Pryse, I. K. Walker, C. N. Mitchell, P. R. Straus, H. Na, C. Biswas, G. S. Bust, G. R. Kronschnabl, and T. D. Raymund (1998). "Two-dimensional mapping of the plasma density in the upper atmosphere with computerized ionospheric tomography (CIT)". In: *Physics of Plasmas* 5.5, pp. 2010–2021. DOI: 10.1063/1.872872.

Beynon, W. J. G. and P. J. S. Williams (1978). "Incoherent scatter of radio waves from the ionosphere". In: *Reports on Progress in Physics* 41.6, pp. 909–955. DOI: 10.1088/0034-4885/41/6/003.

Bilitza, D., D. Altadill, V. Truhlik, V. Shubin, I. Galkin, B. Reinisch, and X. Huang (2017). "International Reference Ionosphere 2016: From ionospheric climate to real-time weather predictions". In: *Space Weather* 15.2, pp. 418–429. DOI: 10.1002/2016SW001593.

Breit, G. and M. A. Tuve (1925). "A radio method of estimating the height of the conducting layer". In: *Nature* 116.2914, pp. 357–357.

Bruno, J., F. Darugna, K. H. A. Bolmgren, J. Wübbena, C. N. Mitchell, and M. Schmitz (2020). "Quality analysis of dual-frequency smartphone-based ionospheric TEC measurements: what can be achieved?" In: *Annals of Geophysics* 63.0, p. 07. DOI: 10.4401/ag-8517.

Bruno, J., C. N. Mitchell, K. H. A. Bolmgren, and B. A. Witvliet (2019). "A realistic simulation framework to evaluate ionospheric tomography". In: *Advances in Space Research*. DOI: 10.1016/j.asr.2019.11.015.

Bust, G. S., G. Crowley, T. W. Garner, T. L. Gaussiran, R. W. Meggs, C. N. Mitchell, P. S. J. Spencer, P. Yin, and B. Zapfe (2007). "Four-dimensional GPS imaging of space weather storms". In: *Space Weather* 5.2. DOI: 10.1029/2006SW000237.

Bust, G. S., T. W. Garner, and T. L. Gaussiran (2004). "Ionospheric Data Assimilation Three-Dimensional (IDA3D): A global, multisensor, electron density specification algorithm". In: *Journal of Geophysical Research: Space Physics* 109.A11. DOI: 10.1029/2003JA010234.

Bust, G. S. and C. N. Mitchell (2008). *History, current state, and future directions of ionospheric imaging*. DOI: 10.1029/2006RG000212.

Cai, C., Y. Gao, L. Pan, and . Zhu J (2015). "Precise point positioning with quad-constellations: GPS, BeiDou, GLONASS and Galileo". In: *Advances in Space Research* 56.1, pp. 133–143. DOI: 10.1016/j.asr.2015.04.001.

Chapman, S. (1931). "The absorption and dissociative or ionizing effect of monochromatic radiation in an atmosphere on a rotating earth". In: *Proceedings of the Physical Society* 43.1, pp. 26–45. DOI: 10.1088/0959-5309/43/1/305.

Chartier, A. T., N. D. Smith, C. N. Mitchell, D. R. Jackson, and P. J. C. Patilongo (2012). "The use of ionosondes in GPS ionospheric tomography at low latitudes". In: *Journal of Geophysical Research: Space Physics* 117.10. DOI: 10.1029/2012JA018054.

Chengqi, R. (2012). "Development of the BeiDou navigation satellite system". In: *Global navigation satellite systems. Report of the Joint Workshop of the National Academy of Engineering and the Chinese Academy of Engineering. Washington, DC.*

Ciraolo, L., F. Azpilicueta, C. Brunini, A. Meza, and S. M. Radicella (2007). "Calibration errors on experimental slant total electron content (TEC) determined with GPS". In: *Journal of Geodesy* 81.2, pp. 111–120. DOI: 10.1007/s00190-006-0093-1.

Coco, D. S., C. Coker, S. R. Dahlke, and J. R. Clynch (1991). "Variability of GPS satellite differential group delay biases". In: *IEEE Transactions on Aerospace and Electronic Systems* 27.6, pp. 931–938. DOI: 10.1109/7.104264.

Colombo, O. L., M. Hernandez-Pajares, J. M. Juan, and J. Sanz (2000). "Ionospheric tomography helps resolve GPS ambiguities on the fly at distances of hundreds of kilometers during increased geomagnetic activity". In: *Record - IEEE PLANS, Position Location and Navigation Symposium*, pp. 15–21.

Da Dalt, F., C. J. Benton, T. Panicciari, N. D. Smith, and C. N. Mitchell (2014). "Implementation of a new ionospheric model (ANIMo) into a three-dimensional variational analysis (3D-Var) for imaging and forecasting purposes". In: *2014 31th URSI General Assembly and Scientific Symposium, URSI GASS 2014*. Institute of Electrical and Electronics Engineers Inc. DOI: 10.1109/URSIGASS.2014.6929836.

Daley, R. (1991). *Atmospheric Data Analysis*. Vol. 2. Cambridge University Press.

Davies, K. (1990). *Ionospheric Radio*. Vol. 36. Peregrinus, p. 312. DOI: 10.1049/ir:19900133.

Davies, K. and G. K. Hartmann (1997). "Studying the ionosphere with the global positioning system". In: *Radio Science* 32.4, pp. 1695–1703. DOI: 10.1029/97RS00451.

De Jonge, P. J. (1998). "A processing strategy for the application of the GPS in networks". PhD thesis.

Dear, R. M. and C. N. Mitchell (2006). "GPS interfrequency biases and total electron content errors in ionospheric imaging over Europe". In: *Radio Science* 41.6. DOI: 10.1029/2005RS003269.

Dvorkin, V. V., Y. I. Nosenko, Y. M. Urlichich, and A.M. Finkel'shtein (2009). "The Russian global navigation satellite program". In: *Herald of the Russian Academy of Sciences* 79.1, pp. 7–13.

European Commission (2016). "Ionospheric Correction Algorithm for Galileo Single Frequency Users". In: *Ionospheric Correction Algorithm for Galileo Single Frequency Users* 1.1.2, p. 96. DOI: 10.2873/723786.

Evans, J. V. (1965). "Ionospheric Backscatter Observations at Millstone Hill". In: *Planetary and Space Science* 13.11, pp. 1031–1074.

Feltens, J., M. Angling, N. Jackson-Booth, N. Jakowski, M. Hoque, M. Hernandez-Pajares, A. Aragon-Angel, R. Orus, and R. Zandbergen (2011). "Comparative testing of four ionospheric models driven with GPS measurements". In: *Radio Science* 46.4, pp. 1–11. DOI: 10.1029/2010RS004584.

Fremouw, E. J., J. A. Secan, and B. M. Howe (1992). "Application of stochastic inverse theory to ionospheric tomography". In: *Radio Science* 27.5, pp. 721–732. DOI: 10.1029/92RS00515.

Ganeshan, A. S., R. Shuntikatte, R. Gupta, and A. K. Jain (2005). "Indian regional navigation satellite system (IRNSS) concept". In: *Journal of Spacecraft Technology* 15, pp. 19–23.

Garriott, O. K. and H. Rishbeth (1969). *Introduction to Ionospheric Physics*. IEEE Transactions on Image Processing, pp. 1–331. DOI: 10.1016/0021-9169(71)90209-1.

Gordon, W. E. (1958). "Incoherent Scattering of Radio Waves by Free Electrons with Applications to Space Exploration by Radar". In: *Proceedings of the IRE*. DOI: 10.1109/JRPROC.1958.286852.

Håkansson, M., A. B.O. Jensen, M. Horemuz, and G. Hedling (2017). *Review of code and phase biases in multi-GNSS positioning*. DOI: 10.1007/s10291-016-0572-7.

Hargreaves, J. K. (1979). *The Upper Atmosphere and Solar Terrestrial Relations: An Introduction to the Aerospace Environment*. Van Nostrand Reinhold.

Hatch, R. (1983). "The synergism of GPS code and carrier measurements". In: *International Geodetic Symposium on Satellite Doppler Positioning*, pp. 1213–1231.

Hernández-Pajares, M., J. M. Juan, and J. Sanz (1999). "New approaches in global ionospheric determination using ground GPS data". In: *Journal of Atmospheric and Solar-Terrestrial Physics* 61.16, pp. 1237–1247. DOI: 10.1016/S1364-6826(99)00054-1.

Hernandez-Pajares, M., J. M. Juan, J. Sanz, and O. L. Colombo (2000). "Application of ionospheric tomography to real-time GPS carrier-phase ambiguities resolution, at scales of 400-1000 km and with high geomagnetic activity". In: *Geophysical Research Letters* 27.13, pp. 2009–2012. DOI: 10.1029/1999GL011239.

Hernández-Pajares, M., J. M. Juan, J. Sanz, and O. L. Colombo (2003). *Feasibility of wide-area subdecimeter navigation with GALILEO and modernized GPS*. DOI: 10.1109/TGRS.2003.817209.

Hernández-Pajares, M., J. M. Juan, J. Sanz, and J.G. Solé (1998). "Global observation of the ionospheric electronic response to solar events using ground and LEO GPS

data". In: *Journal of Geophysical Research: Space Physics* 103.A9, pp. 20789–20796. DOI: 10.1029/98ja01272.

Hounsfield, G. N. (1980). "Computed medical imaging". In: *Science* 210.4465, pp. 22–28.

Huang, X. and B. W. Reinisch (2001). "Vertical electron content from ionograms in real time". In: *Radio Science*. Vol. 36. 2, pp. 335–342. DOI: 10.1029/1999RS002409.

Hunsucker, R. D. and J. K. Hargreaves (2003). *The High-Latitude Ionosphere and its Effects on Radio Propagation*. Cambridge Atmospheric and Space Science Series. Cambridge University Press.

Ifadis, I. (1986). "The atmospheric delay of radio waves: modelling the elevation dependence on a global scale". In: *Licentiate Thesis, Technical Report* 38.

Ivanov, N. and V. Salischev (1992). "The GLONASS System–An Overview". In: *The Journal of Navigation* 45.2, pp. 175–182.

Jakowski, N., S. Heise, A. Wehrenpfennig, and S. Schlüter (2001). "TEC monitoring by GPS - A possible contribution to space weather monitoring". In: *Physics and Chemistry of the Earth, Part C: Solar, Terrestrial and Planetary Science* 26.8, pp. 609–613. DOI: 10.1016/S1464-1917(01)00056-3.

Juan, J. M., A. Rius, M. Hernández-Pajares, and J. Sanz (1997). "A two-layer model of the ionosphere using global positioning system data". In: *Geophysical Research Letters* 24.4, pp. 393–396. DOI: 10.1029/97GL00092.

Klobuchar, J. A. (1987). "Ionospheric Time-Delay Algorithm for Single-Frequency GPS Users". In: *IEEE Transactions on Aerospace and Electronic Systems* AES-23.3, pp. 325–331. DOI: 10.1109/TAES.1987.310829.

Kunitsyn, V. E., I. A. Nesterov, A. M. Padokhin, and Y. S. Tumanova (2011). "Ionospheric radio tomography based on the GPS/GLONASS navigation systems". In: *Journal of Communications Technology and Electronics* 56.11, pp. 1269–1281. DOI: 10.1134/S1064226911100147.

Lanyi, G. E. and T. Roth (1988). "A comparison of mapped and measured total ionospheric electron content using global positioning system and beacon satellite observations". In: *Radio Science*. DOI: 10.1029/RS023i004p00483.

Lee, J. K., F. Kamalabadi, and J. J. Makela (2008). "Three-dimensional tomography of ionospheric variability using a dense GPS receiver array". In: *Radio Science* 43.3. DOI: 10.1029/2007RS003716.

Leitinger, R., H. P. Ladreiter, and G. Kirchengast (1997). "Ionosphere tomography with data from satellite reception of global navigation satellite system signals and ground reception of navy navigation satellite system signals". In: *Radio Science* 32.4, pp. 1657–1669. DOI: 10.1029/97RS01027.

Li, X., M. Ge, X. Dai, X. Ren, M. Fritsche, J. Wickert, and H. Schuh (2015). "Accuracy and reliability of multi-GNSS real-time precise positioning: GPS, GLONASS, BeiDou, and Galileo". In: *Journal of Geodesy* 89.6, pp. 607–635. DOI: 10.1007/s00190-015-0802-8.

Li, X., M. Ge, H. Zhang, and J. Wickert (2013). "A method for improving uncalibrated phase delay estimation and ambiguity-fixing in real-time precise point positioning". In: *Journal of Geodesy* 87.5, pp. 405–416. DOI: 10.1007/s00190-013-0611-x.

Li, Z., N. Wang, L. Wang, A. Liu, H. Yuan, and K. Zhang (2019). "Regional ionospheric TEC modeling based on a two-layer spherical harmonic approximation for real-time single-frequency PPP". In: *Journal of Geodesy*. DOI: 10.1007/s00190-019-01275-5.

Ma, G., W. Gao, J. Li, Y. Chen, and H. Shen (2014). "Estimation of GPS instrumental biases from small scale network". In: *Advances in Space Research* 54.5, pp. 871–882. DOI: 10.1016/j.asr.2013.01.008.

Mannucci, A. J., B. D. Wilson, D. N. Yuan, C. H. Ho, U. J. Lindqwister, and T. F. Runge (1998). "A global mapping technique for GPS-derived ionospheric total electron content measurements". In: *Radio Science* 33.3, pp. 565–582. DOI: 10.1029/97RS02707.

Materassi, M. and C. N. Mitchell (2005). "Imaging of the equatorial ionosphere". In: *Annals of Geophysics* 48.3, pp. 477–482.

Maunder, E. W. (1904). "Note on the distribution of sun-spots in heliographic latitude, 1874-1902". In: *Monthly Notices of the Royal Astronomical Society* 64, pp. 747–761.

McNamara, L. F. (1991). *The Ionosphere: Communications, Surveillance, and Direction Finding*. Orbit, a foundation series. Krieger Publishing Company.

Meggs, R. W., C. N. Mitchell, and V. S. C. Howells (2005). "Simultaneous observations of the main trough using GPS imaging and the EISCAT radar". In: *Annales Geophysicae* 23.3, pp. 753–757. DOI: 10.5194/angeo-23-753-2005.

Mitchell, C. N., D. G. Jones, L. Kersley, S. E. Pryse, and I. K. Walker (1995). "Imaging of field-aligned structures in the auroral ionosphere". In: *Annales geophysicae* 13, pp. 1311–1319.

Mitchell, C. N. and P. S. J. Spencer (2003). "A three-dimensional time-dependent algorithm for ionospheric imaging using GPS". In: *Annals of Geophysics* 46.4, pp. 687–696.

Mitchell, C. N., P. Yin, P. S. J. Spencer, and D. Pokhotelov (2013). "Ionization Dynamics During Storms of the Recent Solar Maximum". In: *Midlatitude Ionospheric Dynamics and Disturbances*. American Geophysical Union (AGU), pp. 83–90. DOI: 10.1029/181GM09.

Montenbruck, O., A. Hauschild, and P. Steigenberger (2014). "Differential Code Bias Estimation using Multi-GNSS Observations and Global Ionosphere Maps". In: *Navigation, Journal of the Institute of Navigation* 61.3, pp. 191–201. DOI: 10.1002/navi.64.

Montenbruck, O., P. Steigenberger, L. Prange, Z. Deng, Q. Zhao, F. Perosanz, I. Romero, C. Noll, A. Stürze, G. Weber, R. Schmid, K. MacLeod, and S. Schaer (2017). *The Multi-GNSS Experiment (MGEX) of the International GNSS Service (IGS) â Achievements, prospects and challenges*. DOI: 10.1016/j.asr.2017.01.011.

Murai, Y. (2014). "Project Overview Quasi-Zenith Satellite System". In: *Proceedings of the ION GNSS+*, pp. 8–12.

Panicciari, T., N. D. Smith, C. N. Mitchell, F. Da Dalt, and P. S. J. Spencer (2015). "Using sparse regularization for multi-resolution tomography of the ionosphere". In: *Nonlinear Processes in Geophysics* 22.5, pp. 613–624. DOI: 10.5194/npg-22-613-2015.

Parkinson, B. W., P. Enge, P. Axelrad, and J. J. Spilker Jr (1996). *Global positioning system: Theory and applications, Volume II*. American Institute of Aeronautics and Astronautics.

Parkinson, B. W. and S. W. Gilbert (1983). "NAVSTAR: Global positioning system—Ten years later". In: *Proceedings of the IEEE* 71.10, pp. 1177–1186.

Pryse, S. E. and L. Kersley (1992). "A preliminary experimental test of ionospheric tomography". In: *Journal of Atmospheric and Terrestrial Physics* 54.7-8, pp. 1007–1012. DOI: 10.1016/0021-9169(92)90067-U.

Psychas, D., S. Verhagen, X. Liu, Y. Memarzadeh, and H. Visser (2019). "Assessment of ionospheric corrections for PPP-RTK using regional ionosphere modelling". In: *Measurement Science and Technology* 30.1, 014001 (17pp). DOI: 10.1088/1361-6501/aaefe5.

Radon, J. (1917). "Über die Bestimmung von Funktionen durch ihre Integralwerte längs gewisser Mannigfaltigkeiten". In: *Berichte Saechsische Akademie der Wissenschaften*, pp. 262–277. DOI: 10.1090/psapm/027/692055.

Rideout, W. and A. Coster (2006). "Automated GPS processing for global total electron content data". In: *GPS Solutions* 10.3, pp. 219–228. DOI: 10.1007/s10291-006-0029-5.

Rishbeth, H. and O. K. Garriott (1969). *Introduction to ionospheric physics*. Vol. 14. Academic Press New York.

Rishbeth, H. and P. Williams (1985). "The EISCAT ionospheric radar: the system and its early results". In: *Quarterly Journal of the Royal Astronomical Society* 26.4, pp. 478–512.

Rose, J. A. R., J. R. Tong, D. J. Allain, and C. N. Mitchell (2011). "The use of ionospheric tomography and elevation masks to reduce the overall error in single-frequency GPS timing applications". In: *Advances in Space Research* 47.2, pp. 276–288. DOI: 10.1016/j.asr.2010.05.030.

Rovira-Garcia, A., D. Ibáñez-Segura, R. Orús-Perez, J. M. Juan, J. Sanz, and G. González-Casado (2020). "Assessing the quality of ionospheric models through GNSS positioning error: methodology and results". In: *GPS Solutions* 24.1, pp. 1–12. DOI: 10.1007/s10291-019-0918-z.

Rovira-Garcia, A., J. M. Juan, J. Sanz, and G. Gonzalez-Casado (2015). "A worldwide ionospheric model for fast precise point positioning". In: *IEEE Transactions on Geoscience and Remote Sensing* 53.8, pp. 4596–4604. DOI: 10.1109/TGRS.2015.2402598.

Rovira-Garcia, A., J. M. Juan, J. Sanz, G. González-Casado, and E. Bertran (2016). "Fast Precise Point Positioning: A System to Provide Corrections for Single and Multi-frequency Navigation". In: *Navigation, Journal of the Institute of Navigation* 63.3, pp. 231–247. DOI: 10.1002/navi.148.

Saastamoinen, J. (1972). "Atmospheric correction for the troposphere and stratosphere in radio ranging satellites". In: *The Use of Artificial Satellites for Geodesy* 15, pp. 247–251.

Saito, S., S. Suzuki, M. Yamamoto, A. Saito, and C.H. Chen (2017). "Real-Time Ionosphere Monitoring by Three-Dimensional Tomography over Japan". In: *Navigation, Journal of the Institute of Navigation* 64.4, pp. 495–504. DOI: 10.1002/navi.213.

Sardón, E., A. Rius, and N. Zarraoa (1994). "Estimation of the transmitter and receiver differential biases and the ionospheric total electron content from Global Positioning System observations". In: *Radio Science* 29.3, pp. 577–586. DOI: 10.1029/94RS00449.

Schaer, S., W. Gurtner, and J. Feltens (1998). "IONEX: The ionosphere map exchange format version 1". In: *Proceedings of the IGS AC Workshop*.

Schwabe, H. (1843). "Solar observations during 1843". In: *Astronomische Nachrichten* 20.495, pp. 234–235.

Spencer, P. S. J. and C. N. Mitchell (2007). "Imaging of fast moving electron-density structures in the polar cap". In: *Annals of Geophysics* 50.3, pp. 427–434.

Spogli, L., L. Alfonsi, V. Romano, G. De Franceschi, J. F. Galera Monico, M. Hirokazu Shimabukuro, B. Bougard, and M. Aquino (2013). "Assessing the GNSS scintillation climate over Brazil under increasing solar activity". In: *Journal of Atmospheric and Solar-Terrestrial Physics* 105-106, pp. 199–206. DOI: 10.1016/j.jastp.2013.10.003.

Su, K., S. Jin, and M. M. Hoque (2019). "Evaluation of ionospheric delay effects on multi-GNSS positioning performance". In: *Remote Sensing* 11.2, pp. 1–19. DOI: 10.3390/rs11020171.

Takahashi, H. (2004). "Japanese Regional Navigation Satellite System "The JRANS Concept"". In: *Journal of Global Positioning Systems* 3.1-2, pp. 259–264.

Tegedor, J., O. Øvstedal, and E. Vigen (2014). "Precise orbit determination and point positioning using GPS, Glonass, Galileo and BeiDou". In: *Journal of Geodetic Science* 4.1. DOI: 10.2478/jogs-2014-0008.

Teunissen, P. J. G. (1991). "The GPS phase-adjusted pseudorange". In: *Proceedings of the 2nd international workshop on high precision navigation Stuttgart/Freudenstadt*, pp. 115–125.

— (2000). *Adjustment Theory, an Introduction*. Delft University Press.

Teunissen, P. J. G. and O. Montenbruck (2017). *Springer Handbook of Global Navigation Satellite Systems*. Springer International Publishing. DOI: 10.1007/978-3-319-42928-1.

Tikhonov, A. and V Arsenin (1977). *Solutions of ill-posed problems*. Winston.

Van De Kamp, M. M. J. L. (2013). "Medium-scale 4-D ionospheric tomography using a dense GPS network". In: *Annales Geophysicae*. DOI: 10.5194/angeo-31-75-2013.

Vierinen, J., A. J. Coster, W. C. Rideout, P. J. Erickson, and J. Norberg (2016). "Statistical framework for estimating GNSS bias". In: *Atmospheric Measurement Techniques* 9.3, pp. 1303–1312. DOI: 10.5194/amt-9-1303-2016.

Walker, I. K., J. A. T. Heaton, L. Kersley, C. N. Mitchell, S. E. Pryse, and M. J. Williams (1996). "EISCAT verification in the development of ionospheric tomography". In: *Annales Geophysicae* 14.12, pp. 1413–1421. DOI: 10.1007/s00585-996-1413-8.

Wang, C., G. Hajj, X. Pi, I. G. Rosen, and B. Wilson (2004). "Development of the Global Assimilative Ionospheric Model". In: *Radio Science* 39.1. DOI: 10.1029/2002rs002854.

Wang, N., Z. Li, B. Duan, U. Hugentobler, and L. Wang (2020). "GPS and GLONASS observable-specific code bias estimation: comparison of solutions from the IGS and MGEX networks". In: *Journal of Geodesy* 94.8, pp. 1–15. DOI: 10.1007/s00190-020-01404-5.

Wang, N., Z. Li, M. Li, Y. Yuan, and X. Huo (2018). "GPS, BDS and Galileo ionospheric correction models: An evaluation in range delay and position domain". In: *Journal of Atmospheric and Solar-Terrestrial Physics* 170, pp. 83–91. DOI: 10.1016/j.jastp.2018.02.014.

Wang, N., Y. Yuan, Z. Li, O. Montenbruck, and B. Tan (2016). "Determination of differential code biases with multi-GNSS observations". In: *Journal of Geodesy* 90.3, pp. 209–228. DOI: 10.1007/s00190-015-0867-4.

Wanninger, L. (2012). "Carrier-phase inter-frequency biases of GLONASS receivers". In: *Journal of Geodesy* 86.2, pp. 139–148. DOI: 10.1007/s00190-011-0502-y.

Wen, D., Y. Yuan, J. Ou, K. Zhang, and K. Liu (2008). "A Hybrid Reconstruction Algorithm for Ionospheric Tomography". In: *October* 46.6, pp. 1733–1739.

Wilson, B. D. and A. J. Mannucci (1993). "Instrumental Biases in Ionospheric Measurements Derived from GPS Data". In: *Proceedings of the 6th International Technical Meeting of the Satellite Division of The Institute of Navigation (ION GPS 1993)*, pp. 1343–1351.

Wilson, B. D., A. J. Mannucci, and C. D. Edwards (1995). "Subdaily northern hemisphere ionospheric maps using an extensive network of GPS receivers". In: *Radio Science* 30.3, pp. 639–648. DOI: 10.1029/94RS03186.

Yin, P., C. N. Mitchell, and J. Kinrade (2011). "The use of GLONASS data in ionospheric imaging over the Antarctic". In: *2011 30th URSI General Assembly and Scientific Symposium, URSIGASS 2011*. DOI: 10.1109/URSIGASS.2011.6050960.

Zha, J., B. Zhang, Y. Yuan, X. Zhang, and M. Li (2019). "Use of modified carrier-to-code leveling to analyze temperature dependence of multi-GNSS receiver DCB and to retrieve ionospheric TEC". In: *GPS Solutions* 23.4. DOI: 10.1007/s10291-019-0895-2.

Zhang, L., T. Yao, W. Peng, L. Shan, Y. He, and J. Kong (2019). "Real-time global ionospheric map and its application in single-frequency positioning". In: *Sensors (Switzerland)* 19.5, pp. 1–17. DOI: 10.3390/s19051138.